Montanuniversität Leoben

Investigation of fundamental deformation parameters on TiAlN films of different chemical composition and crystallographic structure using high-temperature nanoindentation

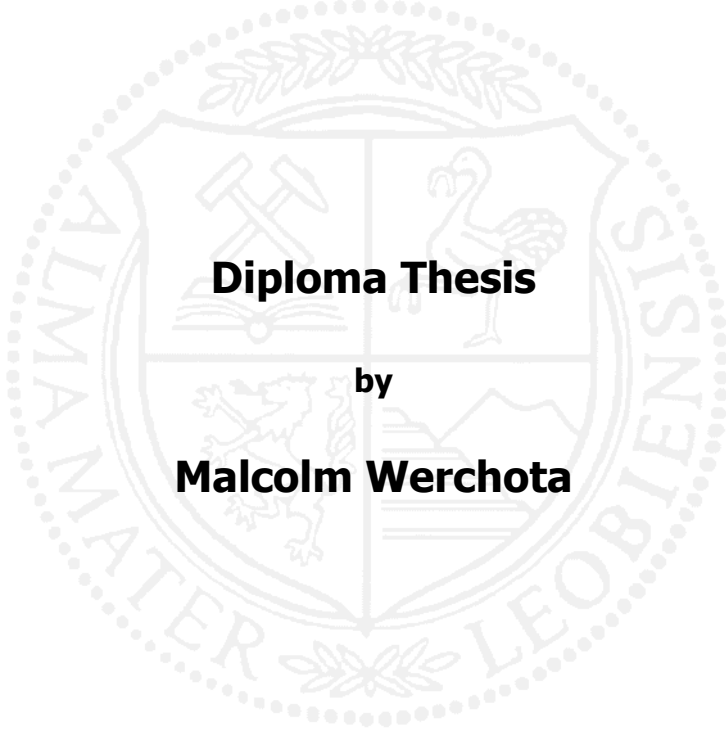

Diploma Thesis

by

Malcolm Werchota

The following thesis was carried out at the Department of Physical Metallurgy and Materials Testing at the Montanuniversität in Leoben, Austria, in cooperation with the UK Center of Structural Ceramics based at the Imperial College in London, UK.

Leoben, October 2010

Affidavit

I hereby declare in lieu of oath, that I have myself composed this diploma thesis and that the work contained therein is my own, except where stated.

Leoben, October 2010

Acknowledgements

My gratitude is in no manner aligned to the acknowledgement "listing" below, but since there is no other way to "list", I express a very special and humble "thank you" to ALL who have been instrumental in helping me along the entire way.

I would like to thank Dr. Paul Mayrhofer for firstly giving me the possibility of writing a diploma thesis with his group at the Department of Physical Metallurgy and Materials Testing in Leoben. Secondly I am thankful for the confidence he has placed in me during all stages of this thesis.

I would further like to thank Dr. Finn Giuliani of the Structural Ceramic Centre at the Imperial College in London, for allowing me to perform all the necessary experiments under his supervision. I am grateful for the planning of my exchange stay and his patience during completion of this thesis.

Dr. Vineet Bhakhri: If I had to thank him for everything he has helped me with, a few additional acknowledgement pages would be the result! All the knowledge I posses about nanoindentation, activation volumes and energies is due to you! Thank you for your help, your never-ending patience in answering my questions and continuously guiding me through the achievement of this work. Thank you!

I also would like to express my gratitude to Constantin Ciurea for very valuable discussions. Thank you for always questioning my motives, experiments and ideas.

I also appreciate the help of Richard Chate for 3D optical measurements, Gerhard Hawranek for EDX measurements, Johannes Pölzl for assistance and support during deposition.

Finally I am indebted to my girlfriend Iris Niesenbacher, my best friend Marianne Mataln and most importantly my FAMILY, which I love very dearly.

Knowing is not enough, we must apply. Willing is not enough, we must do.

Johann Wolfgang von Goethe

Table of Contents

1 Abstract

Metal nitrides, such as TiAlN films are one of the most common hard ceramic coatings in use today. These are primarily used as wear-resistant coatings for cutting tools, to improve among others, resistance to wear, oxidation and corrosion properties. Investigation at high temperatures, where dislocation activity is more significant, is therefore sensible. Using high temperature nanoindentation the typical hardness (H) and Young's modulus (E) measurements were extended to calculate and extract the fundamental deformation parameters, such as activation volumes (V^*) and activation energies (ΔG_{tot}).

For this investigation near-to epitaxial TiAlN films were grown on MgO single crystals (100) using a reactive magnetron sputtering system. After a multitude of pre-deposition runs, single-phased films with the following chemical compositions were achieved and analyzed: cubic-$Ti_{0.44}Al_{0.56}N$, cubic-$Ti_{0.68}Al_{0.32}N$ and wurtzite-$Ti_{0.36}Al_{0.64}N$. Additionally cubic-$Ti_{0.44}Al_{0.56}N$ was annealed at 600°C for 24 hours. HT-nanoindentation experiments were carried out in a temperature range from 25 - 350°C at 3 different loading rates of 0.5, 1 and 10 mN/s using a Berkovich indenter.

Hardness values of the all cubic samples were stable (~22-23 GPa for cubic $Ti_{0.68}Al_{0.32}N$ and $Ti_{0.44}Al_{0.56}N$, and ~28 GPa for the annealed cubic $Ti_{0.44}Al_{0.56}N$) in the measured temperature range, with a slight decrease at 350°C. XRD analyses on powder samples of cubic-$Ti_{0.44}Al_{0.56}N$ before and after annealing at 600°C for 24 hours indicate an increase of the integral width from 0.55 to 0.59 suggesting ongoing spinodal decomposition to form Ti- and Al-rich cubic domains, resulting in a small age-hardening behavior. The H values of the wurtzite sample on the other hand decreased continuously from 19.8 ± 0.9 GPa at 25°C to 16.9 ± 1.4 GPa at 350°C. Young's modulus values for all samples remained constant throughout the temperature range: 344 ± 34 GPa for c-$Ti_{0.68}Al_{0.32}N$, 336 ± 23 GPa for c-$Ti_{0.44}Al_{0.56}N$-as-deposited, 356 ± 21 GPa for c-$Ti_{0.44}Al_{0.56}N$-annealed and 219 ± 11 GPa for the

wurtzite-$Ti_{0.36}Al_{0.64}N$. H values of the films were found to be loading rate sensitive at all temperatures, leading to an increase of up to 20% for the cubic films, when tested with 10 mN/s.

Dislocation activation volume values, V^*, for the cubic sample were in the range of 0.18 to 0.79 b^3. V* values for the wurtzite sample were larger, ranging from 0.24 to 1.22 b^3. The activation volume of the annealed sample only rose slightly compared to other samples. Ab-initio calculations using the VASP package showed that 1.63% rise of V^* in the tested temperature range is due to thermal expansion. For further comparison purposes, V^* values were determined for bulk-aluminum at room temperature using a population density function (PDF). V^* values ranged between 0-4 b^3 for the cubic films and 0-25 b^3 for bulk-aluminum, which is a clear indication for a different deformation mechanism than present in ceramic films. Similarly to the V^* values, ΔG_{tot} for the cubic and wurtzite samples were very close and ranged between 0.19 and 0.86 eV. ΔG_{tot} values rose linearly with the temperature, whereby both the thermal and the mechanical work equally influenced the calculated values.

Summing up for the tested temperature range, the crystallographic structure of TiAlN films had the largest influence on all measured parameters. Calculation of the activation energies show that the obstacles encountered by moving dislocations are of weak nature and that lattice-resistance can be determined as rate-controlling deformation mechanism, due to the stiff nature of hard ceramic films, as V^* values were smaller than the volume of one dislocation, E values were constant and ΔG_{tot} of very low order. Comparative studies for soft bulk-aluminum exhibit a dislocation-dislocation interaction. This investigation proved that high temperature nanoindentation can be used to successfully extract fundamental deformation parameters in hard ceramic-like coatings and to conclude, which rate-controlling deformation mechanism is active.

2 Theory

2.1 Introduction

Out of absence of adequate apparatus or out of convenience, the mechanical properties of hard ceramic coatings are determined from room temperature tests or after annealing. As TiAlN coatings are used primarily for high temperature applications, it is more sensible to determine the mechanical characteristics at the actual high temperatures.

High temperature nanoindentation provides the possibility of testing the coatings at elevated temperatures. Hardness and elastic modulus measurements of TiAlN films have already previously been carried out at elevated temperatures but without the consideration of important influences, such as the substrate influence [1]. This master thesis aims at extending the typical hardness and elastic modulus measurements to calculate and extract the fundamental deformation parameters, such as activation volumes and activation energies. Extracting the fundamental deformation parameters can give an insight into the rate-controlling mechanism taking place in the given temperature range.

This investigation is motivated by the desire to understand the kinetics of deformation and its correlation with temperature, chemical composition and crystallographic structure of reactive magnetron sputtered TiAlN films.

The first chapter will introduce the hereby investigated TiAlN films, the deposition process and a short theoretical introduction about the nanoindentation testing method. The second chapter will report on the experimental procedure used for deposition of the films. The determined hardness, Young's moduli, activation volume and activation energy results and the ensuing discussions will be presented in the chapter 4. Finally an outlook for future considerations and experiments will be given in the last chapter.

2.2 Historical overview

Why were metals not commonly used in utensils, machines and tools before the early 18th century? Why were early machines, such as, the Spinning Mule, early bridges and even early washing machines made out of wood?

There are most definitely many aspects that have to be looked at, in order to answer these questions. Yet undoubtedly, one of the most important aspects responsible for the lack of usage of metals before the industrial revolution, was the difficulty relating to their precise manipulation and machining. Figure 2-1 depicts the *"machining turner"*, which is viewable at the Science Museum in London, is an example of an early lathe, which acted as a catapult in the precise and stabile manufacturing of metal tools and machines.

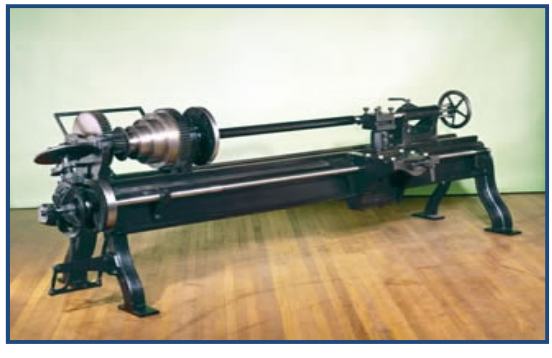

Figure 2-1: Early lathe: "the machining turner"; 1816.

Research in machining, has come a very long way since the 18th century, yet nowadays we are still faced with similar challenges than those encountered by our ancestors: growing elevated temperatures, higher impact forces and increasing wear. Because of both, high speed and pressure while machining, cutting tools heat up to temperatures which can be higher than their melting points. These cutting tools would literally melt away, if they were not protected or shielded by coatings.
Different types of coatings have been developed, to protect the base materials. The ongoing development, upgrade and improvement of coatings for cutting tools have been fueling research. In this diploma thesis, we will investigate one of the presently widely used hard ceramic coatings: **titanium aluminum nitride (TiAlN)**.

2.3 Thin ceramic coatings: TiAlN

Metal nitrides such as TiAlN coatings are one of the most common hard ceramic coatings in use today. These have only been developed as recently as the 1980's and are industrially used because of the exceptional properties they offer [2]. TiAlN coatings are primarily used as wear-resistant coatings for cutting tools, to improve among others, resistance to oxidation, erosion and corrosion, thereby enabling faster machining speeds, allowing a longer lifetime and thus finally improving overall productivity. The usage of TiAlN coatings is in no way only restricted to cutting tools. Their applications range from diffusion-barriers on integrated circuits, functional coatings for satellites and even protective coatings for the IPod [3],[4].

Advantages: TiAlN films present the following superior advantages [5], [6], [7]:

High temperature oxidation resistance: TiAlN possesses excellent oxidation resistance properties due to the formation of a protective dense Al_2O_3 and TiO_2 layer. The layer acts as a diffusional barrier preventing oxidation [3], [7], [8].

Machining properties: During high speed machining, cutting tools are faced with very tedious conditions: High stresses of up to ~700 MPa, temperatures of over 1000°C, repeated impact and chemical interaction. Tool life can be extended when coated with TiAlN for machining of various materials, such as steel, cast iron and even aluminium alloys [9].

Age hardening capabilities: When used at high temperatures TiAlN films not only maintain their high wear resistance up to 1000°C but are even known to increase their hardness. This happens through the process of spinodal decomposition, where the cubic-TiAlN phase decomposes into two coherent cubic nanometer-size domains: aluminum nitride (AlN) and titanium nitride (TiN). A deeper look into this phenomenon will be taken in the next chapter 2.4 [10].

Corrosion resistance: The corrosion rate of steels, amongst others, can be diminished substantially by three orders of magnitude when substrates are coated with TiAlN [3].

Crystallographic structure: TiAlN films have a metastable face centered cubic (fcc)-NaCl crystallographic structure, where the aluminum atoms substitute titanium in the cubic-NaCl TiN structure for $Ti_{1-x}Al_{-x}N$ compositions of $0<x<0.66$. The cubic structure remains stable until approximately $0.65<x<0.75$ [10]. Ab-initio and experimental studies have shown that the NaCl structure then switches to a hexagonal-wurtzite structure for $x>0.65$ [3], which is illustrated in Fig. 2-2:

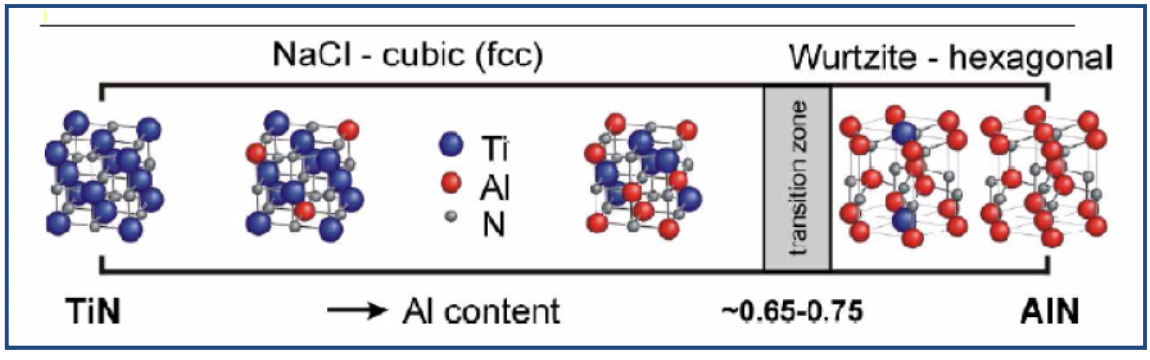

Figure 2-2: Cubic and wurtzite structure of TiAlN over aluminum content [11].

Plastic deformation takes place in ceramics by the motion of dislocations, such as in metals [12]. Furthermore, the lattice resistance is much higher in ceramics compared to metals due to the nature of the bondings. The bond structure in transition metal nitrites consists of a mixture of ionic and covalent components [2]. The covalent component of the bonding is strong and directional making dislocation movement very difficult. The ionic component, on the other hand, increases the Peierls stress for dislocation glide, which is the determining factor for the slip system. The charge neutrality imposes that, dislocations only move on crystallographic planes and directions which prevent the proximity of a like charge [13].

The hardness of TiAlN, which is nothing else as the resistance to dislocation motion is majorly influenced by the addition of Al. With increasing Al content, the hardness is known to increase [3]. In a range of 0.65-0.75 the cubic-NaCl structure becomes unstable and transforms into a wurtzite-ZnS $Ti_{1-x}Al_xN$ and cubic-NaCl $Ti_{1-x}Al_xN$ structure or for higher Al contents even to a single-phased wurtzite $Ti_{1-x}Al_xN$.

The hardness as well as further mechanical properties drop, when the fraction of cubic structure decreases at aluminium x-values higher than 0.65. Since aluminum atoms are smaller in atomic size than titanium atoms, the lattice parameter of cubic-TiAlN also decreases with increasing aluminum content (see Fig. 2-3).

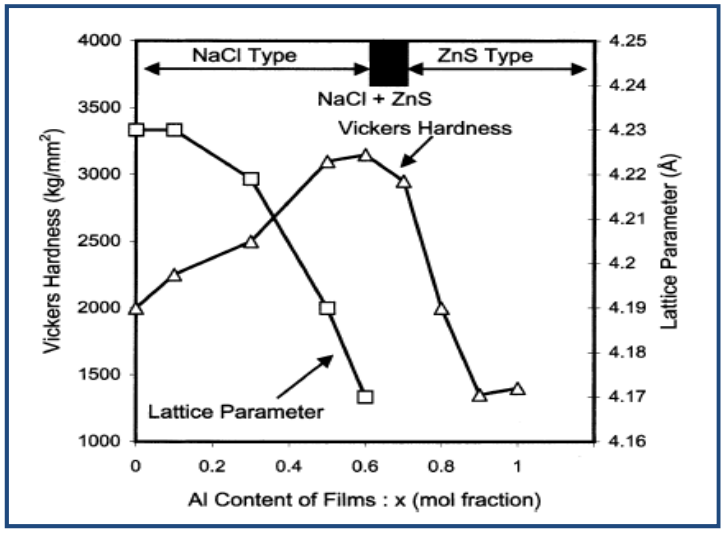

Figure 2-3: Change of hardness and lattice parameters in dependence of aluminium concentration in $Ti_{1-x}Al_xN$ films [3].

TiAlN films are usually deposited through a physical vapor deposition (PVD) process, which will be discussed in chapter 2.5.

2.4 Age hardening through spinodal decomposition

Spinodal decomposition, easier understood under the term „spontaneous phase separation", is a mechanism, in which a phase α transforms into two phases α' and α" of the same lattice. This reaction is solely governed by a diffusion reaction. Spinodal decomposition is very different to nucleation and precipitation, although both result in a phase separation.

Spinodal decomposition occurs spontaneously, when the second derivative of the Free Gibbs Energy G turns negative. The system is then considered to be unstable and tends to separation. The points where this occurs are referred to as "spinodal points". The dark grey region in Fig. 2-4 is called the spinodal region and this is where phase separation takes place by spinodal decomposition.

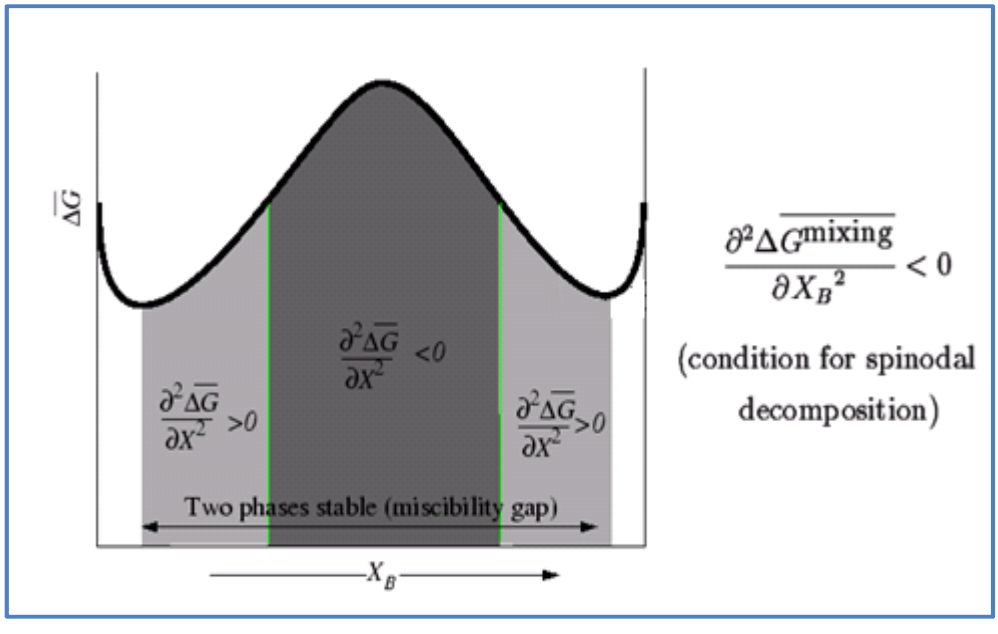

Figure 2-4: Molar free-energy change for the areas of spinodal decomposition [14].

TiAlN are metastable films and are known to decompose spinodally, resulting in the formation of two stable compounds: TiN and AlN. Adibi et al. had already reported in 1991, about surface-diffusion initiated spinodal decomposition for $Ti_{0.5}Al_{0.5}N$ [15]. Mayrhofer et al. have further determined that in a first step, c-TiAlN decomposes spinodally by forming coherent Ti- and Al-rich domains. In a second step, a following phase transformation takes place where these domains further stabilise into c-TiN

and w-AlN, this is schematically presented in Fig. 2-5. The change of c-AlN into w-AlN is accompanied by a decrease in hardness [10].

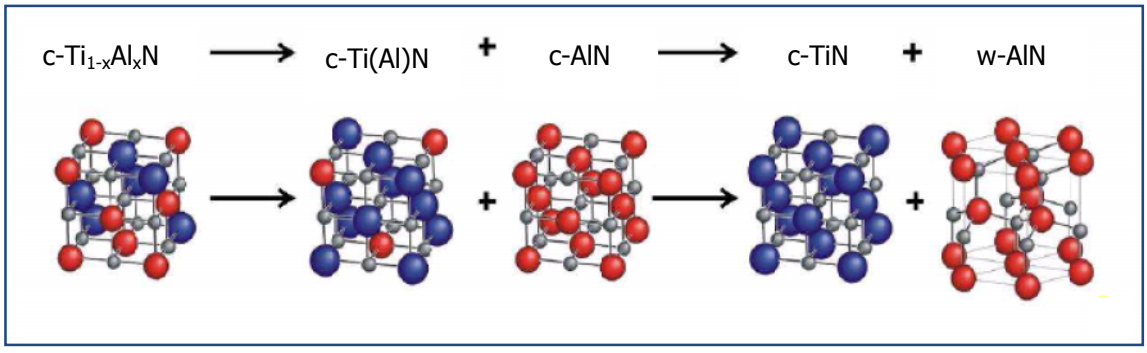

Figure 2-5: Structural changes due to spinodal decomposition of TiAlN [11].

Experimental observations as well as ab-initio calculations have shown that both the hexagonal-TiAlN and the cubic-TiAlN are metastable and prone to decomposition into c-TiN and w-AlN. Regardless of the Aluminium content, TiAlN will either decompose after heat treatment or when given enough time.

We will not focus with too much detail on spinodal decomposition, as this phenomenon is not expected to take place in the testing temperature range used in this thesis.

The next chapter will focus on the very energetic process used to deposit these films: Magnetron sputtering.

2.5 Deposition process: Magnetron sputtering

The main goal of a coating technique is to deposit uniform films, with a good adherence for improving the properties of the substrate. TiAlN coatings are metastable coatings, which would not exist under equilibrium conditions. A very energetic process is required in order to deposit such films. The most common deposition process for TiAlN films is through physical vapour deposition (PVD).

PVD is a process based on the formation of vapour of the material to be deposited. The material to be deposited can either be evaporated or sputtered by ions. Sputtering, which is the process used by the deposition apparatus of this thesis, will be focused on [16].

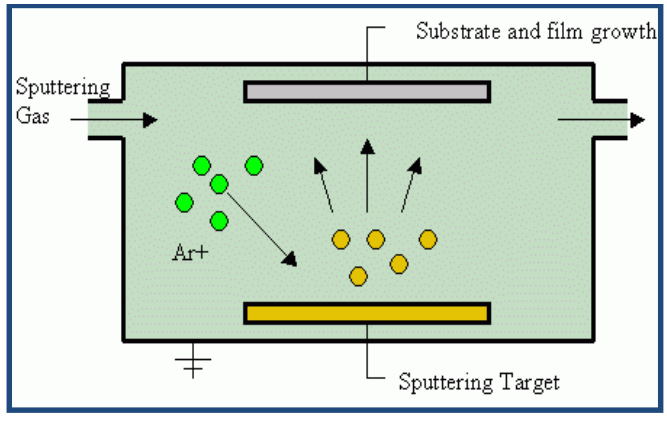

Figure 2-6: Schematic of a sputtering process [17].

As illustrated in Fig. 2-6, Sputtering is a process, by which argon ions ballistically eject species (mostly atoms) from a target (bottom yellow block), which in turn then fly and deposit onto a substrate (top grey block). Sputtering, in comparison to evaporation, necessitates the ignition of a plasma, also called glow discharge. The plasma has the role of generating the ions used to eject the target material. The ionised gas is often an inert gas, such as Argon, which bombards the target. Through sputtering, deposition of high melting metals is possible. Further on, the sputter deposited films show a similar composition as the target. PVD deposition takes place in a vacuum in order to largely remove residual gases. Thereby source material particles are less prone to collide with gas particles and a higher amount of particles reach the substrate. This results in smoother and more uniform films.

Several PVD techniques are available for the deposition of hard coatings. Magnetron sputtering will be focused on.

A magnetron consists of magnets of alternating polarity arranged behind the target. A negative voltage is supplied to the magnetron. The main objective of a magnetron is to trap electrons near the target surface. These electrons follow a helical path along the magnetic field lines, further ionising neutral argon gas atoms (Fig. 2-7). This in turn enables a denser plasma to be sustained at the target surface, which further increases the resulting sputter rate. The second advantage of a magnetron is that magnets enable a lower gas pressure to be used, thereby reducing collision possibilities. Finally the substrates to be deposited can be given a negative biased voltage, in order to attract the positively charged ions and thereby assisting film growth processes by kinetic-energy transfer. For further studies see [16].

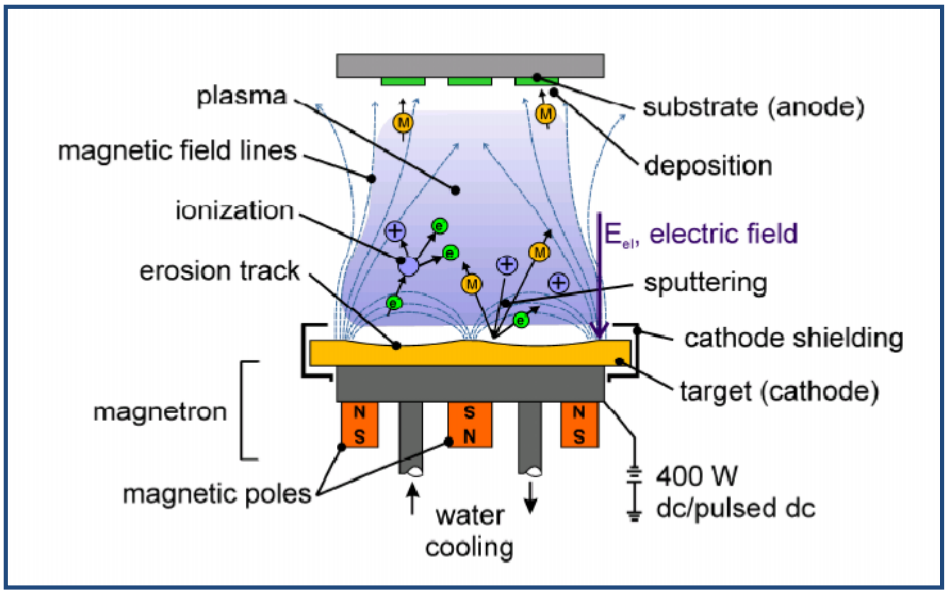

Figure 2-7: Schematic illustration of an unbalanced magnetron [11].

For reactive sputtering, the metal target is exposed to a discharge of a noble gas with some fraction of reactive gas. Titanium aluminium nitride films can be sputtered using a titanium-aluminium target and nitrogen reactive gas.

The deposited TiAlN films will be primarily analyzed using nanoindentation. The next chapter will focus on the theory behind this method.

2.6 Nanoindentation theory

Indentation, used for the determination of mechanical properties, is in no way a "new" method. Scientists, such as Mohr, have in early days understood that the contact between two materials can be used to measure mechanical properties. Indentation has really become popular with the introduction of simple tests, such as the Brinell indentation test, which was first presented by a Swedish mechanical engineer Johan August Brinell at the universal exposition in Paris in 1900 [18].

Indentation is a method by which a hard tip is pressed into a soft sample. Mechanical properties can be determined and analysed without having to optically image the indentation. The hardness of the sample can thereby be measured, which can in turn be correlated to various other mechanical properties. The most widely used method for characterisation is the determination of the properties using the load-displacement curve (Fig. 2-8). A tip is pressed into the sample with increasing load until a certain load P_{max} has been reached. Then the force is slowly decreased to zero. The penetration of the sample first leads to an elastic response and then to plastic deformation. After the sample is unloaded, only the plastic deformation remains. Figure 2-8 presents a typical illustration of a load displacement curve, whereby P_{max} is the maximum Load, h_{max} the maximum displacement, S the elastic unloading stiffness and h_f is the indenter displacement after unloading.

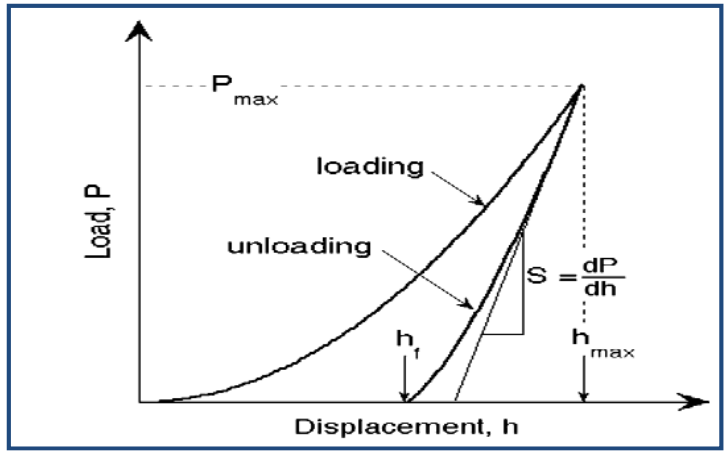

Figure 2-8: Schematic of a load-displacement curve from an indentation cycle [19].

Nanoindentation is a particularly attractive investigative technique as it presents the following 2 advantages:

Easy to use: As indentation is a simple technique, it is widely used for quality control in industrial manufacturing.
Sample size: Indentation can be performed on all samples irrespective of their size. Nanoindentation, which uses a tip as small as a few nanometers (nm), can even be used on samples, which would be too small to perform uniaxial tests on.

There are a multitude of indenter tips that can be used for indenting the sample.

The Vickers indenter is the most widely used indenter, especially for microindentation. It is a four-sided pyramid, with face angle of 68.0°, which can be seen in Fig. 2-9. A very popular indenter tip is the Berkovich indenter tip. The Berkovich indenter tip, seen in Fig. 2-10, is the most widely used tip for nanoindentation. It is a three-sided pyramid, which can easily be manufactured, as the sides always meet at a single point. This is a main advantage of a Berkovich tip compared to a Vickers tip, where it is more difficult to manufacture a four-sided pyramid. The Berkovich tip has a lower face angle of 65.03°, which reduces the influence of friction.

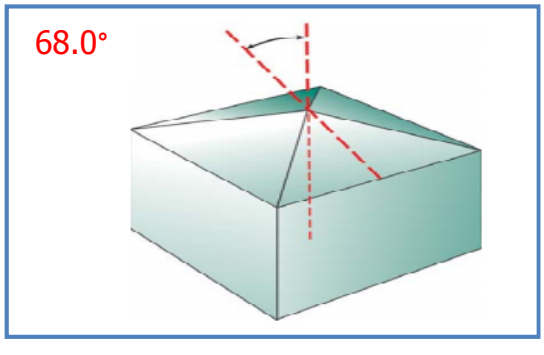

Figure 2-9: Vickers indenter tip [20].

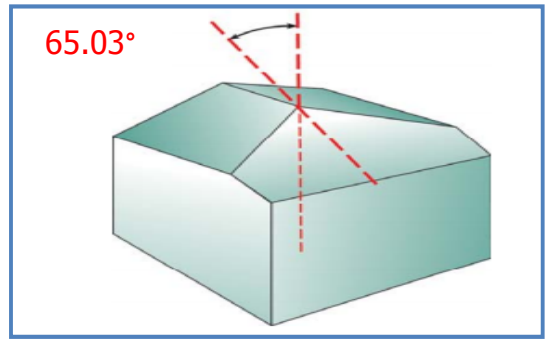

Figure 2-10: Berkovich indenter [20].

Further on, pyramidal indenters are geometrically self-similar, meaning that the ratio of depth to height is independent of the depth (h) and constant. The projected area of contact A of both the Vickers and Berkovich indenter is $24.5.h^2$ [19].

In theory, the projected area of the indenter tip increases with the indentation depth. Yet this is only valid for an ideal shape of an indenter tip. In reality, the indented tip wears out with time, thus changing its shape. Therefore the shape has to be determined regularly using fused silica.

There are numerous ways to analyse the load-displacement curves. The most widely used method, developed in 1992 by Oliver and Pharr will be used here [19]. The hardness, which is nothing else as the resistance to plastic deformation, can be defined as the instantaneous load divided by the instantaneous projected area [19]:

$$H = \frac{P_{max}}{A} \tag{2-1}$$

whereby H is the hardness in [Pa], P_{max} is the maximum Load in [N] and A is the contact area between the tip and the sample [m^2].

The correct measurement of the following three quantities is important:
P_{max}, h_{max} the maximum displacement in [m] and S the elastic unloading stiffness S=dP/dh [N/m], which is the slope of the upper portion of the unloading curve, see Fig. 2-8.

The elastic modulus can be then calculated using the following formula [19]:

$$S = \frac{2}{\sqrt{\pi}} \beta \, E_{eff} \sqrt{A} \tag{2-2}$$

$$\frac{1}{E_{eff}} = \frac{1-\nu^2}{E} + \frac{1-{\nu_i}^2}{E_i} \tag{2-3}$$

whereby β accounts for the deviation in stiffness, E_{eff} is the effective elastic modulus [GPa], E_i and ν_i are the Young's modulus and Poisson ratio of the indenter.

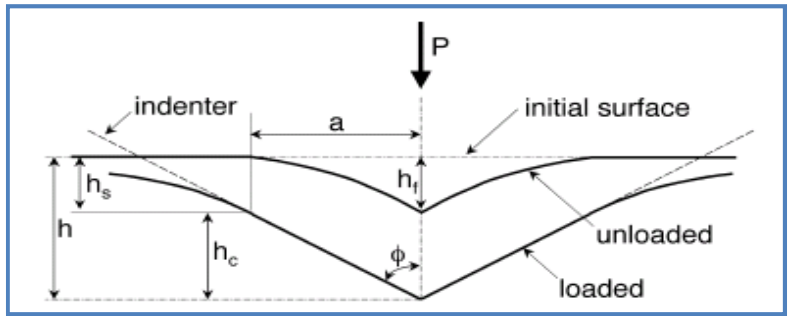

Figure 2-11: Schematic representation of a section through an indentation showing various quantities used in the analysis [19].

The schematic representation in Fig. 2-11 shows that the plastic depth h_c is equal to the total depth h_t [nm] minus the elastic component h_s [nm]. The plastic component can be therefore be calculated by subtracting the elastic compliance from the elastic contribution [19]:

$$h_c = h_t - \varepsilon . \frac{P_{max}}{S} \tag{2-4}$$

whereby ε a constant is, that depends on the geometry.

In the last decade, due to advances in electronics and sensors, very precise indentation, such as, nanoindentation became possible, with force measured in the millinewton range and displacement measured in the nanometer range. Indentation on the submicron scale enables the possibility to outreach the measurement of common hardness and elastic modulus. The focus of the next chapter will be the theory behind the calculations of kinetics of deformation using nanoindentation data.

2.7 Kinetics of deformation

During nanoindentation, the Berkovich tip creates a high local stress state, which can be represented by the average indentation stress σ_{ind} [MPa] [21]:

$$\sigma_{ind} = \frac{P}{A(h)} \tag{2-5}$$

where P is the instantaneous Force and A(h) is the instantaneous area function of the indenter tip.

The material deformation rate under the indenter can be expressed by the indentation strain rate $\dot{\varepsilon}$ [s^{-1}] [22]:

$$\dot{\varepsilon} = \frac{\dot{h}}{h} \tag{2-6}$$

where $\dot{h}$ is the indentation velocity and h the indentation depth.

The average indentation shear τ_{ind} stress [MPa], which is athermal and responsible for dislocation movement, can be calculated using the von-Mises yield criteria. It is related to the indentation stress as follows [22]:

$$\tau_{ind} = \frac{\sigma_{ind}}{3\sqrt{3}} \tag{2-7}$$

The average indentation shear strain rate $\dot{\gamma}_{ind}$ [s^{-1}] is a function, which is dependent on the average effective shear stress τ_{ind} [22]:

$$\dot{\gamma}_{ind} = \sqrt{3}\,\dot{\varepsilon} \tag{2-8}$$

If a dislocation glide mechanism takes place under the indent, due to the large stress around the indentation, the following constitutive relationship between strain rate, stress and temperature can be used [22]:

$$\dot{\gamma}_{ind} = \dot{\gamma}_0 e^{-\frac{\Delta G(\tau)}{kT}} \tag{2-9}$$

where $\Delta G(\tau)$ [J] is the thermal activation energy, $\dot{\gamma}_0$ = 1.10^8 [s^{-1}] is a pre-exponential constant when the deformation mechanism is dislocation-dislocation interaction [23], k is $1.38.10^{-23}$ [$\frac{J}{K}$] the Boltzmann constant and T the temperature [K]. This pre-exponential constant $\dot{\gamma}_0$ has a value of 1.10^{11} [s^{-1}] if the mechanism in place is lattice-resistance.

2.7.1 Activation energy

Fig. 2-12 depicts a dislocation trying to overcome an obstacle, e.g. a potential barrier ΔG_{tot}:

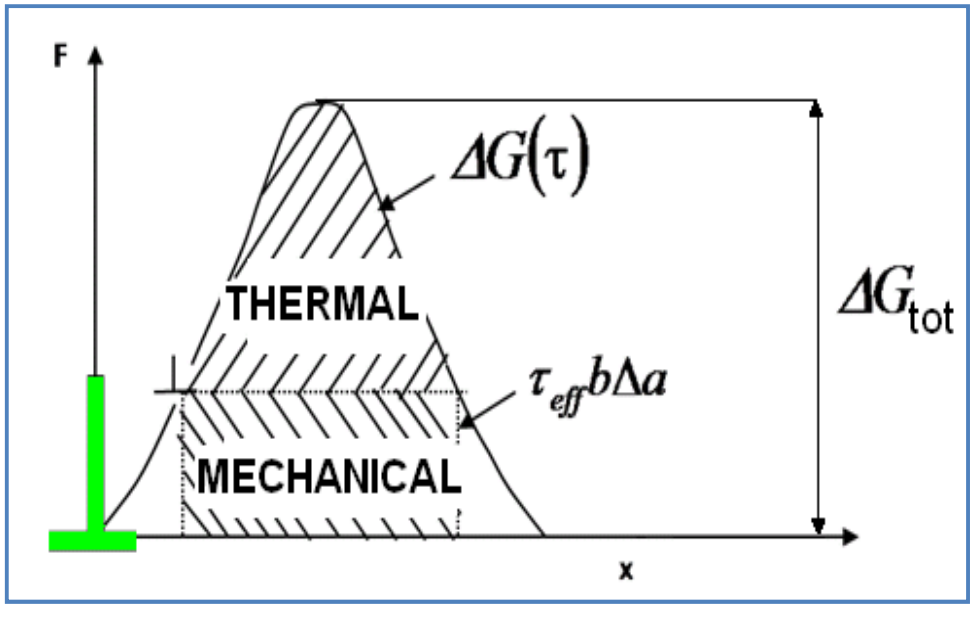

Figure 2-12: Dislocation having to overcome an idealised obstacle ΔG_{tot} [21].

If a shear stress is applied to a dislocation, there would be two components that would play a role in overcoming the obstacle. The first component is a thermal component, which is responsible for the vibration of atoms: $\Delta G(\tau)$. The second component is a mechanical component, which is the mechanical energy that is supplied externally to the dislocation by the shear stress τ. The addition of the thermal agitation and the mechanical part is equal to the total activation energy ΔG_{tot} required by a dislocation for overcoming the rate-controlling obstacles [21]:

$$\Delta G_{tot} = \Delta G(\tau) + \Delta W = \Delta G(\tau) + \tau.(b.\Delta a) \qquad (2\text{-}10)$$

whereby b is the burgers vector [m] of the dislocation and Δa [m^2] is the area swept through by the dislocation as seen in Fig. 2-13. Here d(l) is the distance between two obstacles and x is the distance travelled by the dislocation:

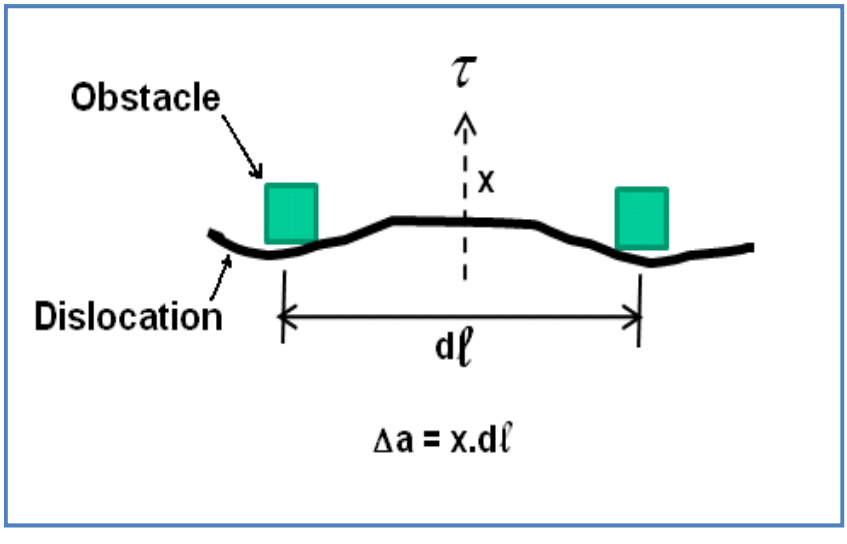

Figure 2-13: Dislocation overcoming obstacles and sweeping an area Δa [21].

2.7.2 Activation Volume

An activation volume V* is the volume over which the thermal energy is to concentrate in order to achieve the activation of a dislocation over an obstacle [21, 24]. As seen in Fig. 2-13, the activation volume V* is the length of the burgers vector times the area swept through, whereby V* is in [m^3]:

$$V^* = x.dl.b = \Delta a.b \tag{2-11}$$

The activation volume is therefore effectively indicating the size of the segment of the dislocation line, which jumps in the rate determining step. Thus the determination of activation volumes is a further indication for the size of the obstacle that has to be overcome during dislocation movement [24].

The activation volume can be calculated by using the derivative of $\Delta G(\tau)$ with respect to τ [21]:

$$V^* = \frac{d\Delta G(\tau)}{d\tau} \tag{2-12}$$

The next chapter will deal with the experimental procedure used to deposit the TiAlN films.

3 Experimental procedure for deposition of the films

3.1 Substrates used for deposition: Magnesium oxide (100)

To investigate TiAlN coatings a wide range of substrates have been used including industrial cermented carbides, cermets and high speed steels, which are in practice actually coated with TiAlN [7]. However for this scientific research topic, a single crystal was chosen as substrate, in order to rule out certain effects caused by substrate effects.

Magnesium oxide (MgO) substrates were chosen for deposition of TiAlN films. MgO was primarily chosen as it is considered to be a hard ceramic substrate. This will facilitate the interpretation of nanoindentation results. Further on epitaxial TiAlN films have already been successfully grown on MgO [25]. To limit substrate effect, the intention was to grow epitaxial films. Even though MgO is harder than most common available materials, it is softer compared to TiAlN. The hardness values of MgO (100) lay at around 12 GPa and also decreases with indentation depth [25].

Single-crystal MgO (100) samples (CrysTec) were used for all coatings. The substrates were sized 10x10x1 mm^3 and polished on both sides. All substrates were first ultrasonically cleaned for 10 minutes in acetone, then with ethanol to remove any acetone residues.

3.2 Sample holder

To enable a simultaneous uniform deposition of multiple films, a sample holder was fabricated out of non-magnetic steel, as visible in Fig. 3-1:

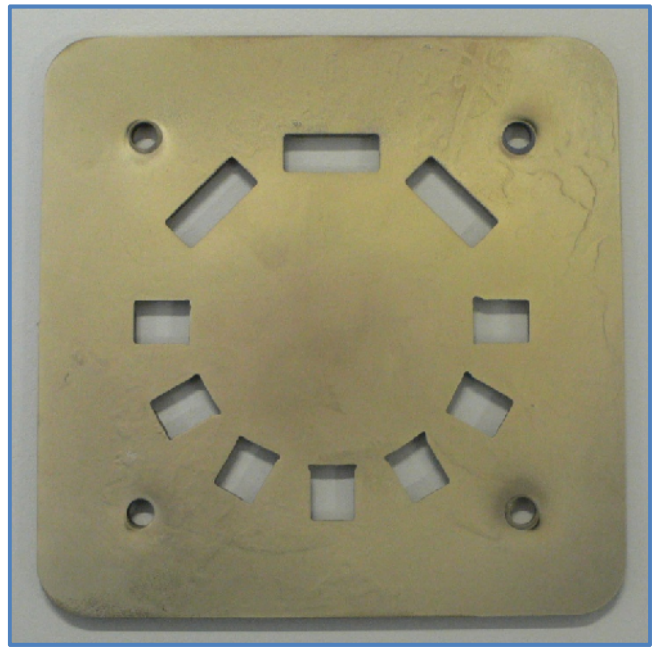

Figure 3-1: Picture of the fabricated sample holder used for deposition of all films.

The samples were placed in a circular order to enable equidistance from the target. The substrates-to-target distance was 10 cm. A constant substrate to target distance guarantees the exposure of the substrate to constant scattering losses. A constant angular distribution of the sputter flux is also guaranteed by a circular configuration of the substrate holder.

It was ascertained that the sample position on the holder had no influence on the attained microstructure on the coating, meaning that the plasma was uniform within the chamber. This was evident from the XRD analysis of each and every of the 150 samples deposited during 40 deposition runs, which included the pre-deposition runs described in chapter 3.4.

3.3 Target composition: $Ti_{0.5}Al_{0.5}$

For all deposited coatings, a powder metallurgical prepared target with a 50-50 titanium-aluminium chemical composition was used. The target, with a diameter of 152.4 mm, had a purity of 99.9% was supplied by PLANSEE. The target was cleaned by pre-sputtering against a shutter every single time before starting the deposition.

3.4 Deposition system: Reactive magnetron sputtering system

3.4.1 Deposition system

The main objective was to deposit films of very good quality. Therefore a reactive unbalanced DC magnetron system was used. This deposition system, which can be seen in Fig. 3-2, is described elsewhere in detail [26].

Figure 3-2: Picture of the reactive magnetron sputtering system used in this thesis.

Permanent circular magnets are located behind the target. An external pair of Helmholtz coils was used to create a uniform magnetic field B_{ex}. The films were sputtered in an argon and nitrogen glow discharge. Before deposition the substrates were not etched, in order to prevent amorphization of the orientated single crystal surface.

3.4.2 Deposition conditions

Deposition temperature: The crystalline quality of as-deposited layers is typically increased by raising the film growth temperature. Therefore the highest possible deposition temperature of the system was chosen to achieve epitaxial growth of the coatings: 500°C. Hultman et al. have successfully deposited epitaxial TiAlN films on MgO at similar temperatures (500 – 850°C) [27].

Bias voltage: The same bias voltage of minus 50V was applied for all deposition runs in order to ease comparison of samples.

Pressures: The base pressure before deposition was in the range of 5.10^{-6} mbar. The working gas pressure was $0.4.10^{-2}$ mbar (0.4Pa). Pressure after deposition was in the range of $\sim 2.10^{-6}$ mbar.

3.4.3 Deposition procedure

Heating cycles: To ensure a "high quality" deposition (high vacuum), the deposition chamber was heated up to 500°C and then cooled down to room temperature three times in a row to achieve base pressures of less than 9×10^{-6} mbar.

Target pre-cleaning: When the vacuum pressure stabilised, the target was pre-sputtered to ensure a clean deposition.

Deposition time: The deposition time varied between 3 to 4.5 hours.

Gases: Pure Argon (99.99%) and Nitrogen (99.99%) gases were used as sputtering and reactive gas, respectively.

3.4.4 Pre-deposition studies

More than 150 MgO samples were pre-deposited in more than 40 deposition runs. The high number of deposition runs include the pre-deposition studies, which were necessary for obtaining near-epitaxial films with the desired chemical composition of ~$Ti_{0.75}Al_{0.25}N$, ~$Ti_{0.5}Al_{0.5}N$ and ~$Ti_{0.25}Al_{0.75}N$. Another important factor for the high number of pre-deposition studies was the growth in single-phase cubic structure for the Ti-rich films and single-phase wurtzite structure for the Al-rich films. The latter was difficult to achieve, therefore the N_2-partial pressure had to be increased to drastically influence the growth-kinetics. The pre-deposition studies are not presented in this thesis, as only the three main coatings of different chemical composition and different crystallographic structure will be focused on.

The brief summary of the deposition conditions such as bias voltage, nitrogen and argon flow, etc., for the investigated films, is presented in appendix 1.

4 Results

The results are structured as follows: First, the visual appearance, chemical composition, crystallographic structure and film thickness will be investigated. Then a detailed analysis of the measured hardness and Young's moduli values will be presented. A rate controlling mechanism will be defined following activation volume and activation energy calculations. Finally plastic index calculations will help determine, which applications these coatings are best suited for.

4.1 Characterization of films

Coatings were characterised with respect to visual appearance, chemical composition, crystallographic structure and film thickness.

4.1.1 Variation of the chemical composition of deposited films

Using a 50-50 Al:Ti target ratio films of the following chemical composition were obtained: $Ti_{0.33}Al_{0.66}N$. The deviation of the target ratio results from the fact that Al and Ti have not only different sputtering conditions, but also different angular and scattering losses [28]. To deposit films with a higher Ti-Al ratio, Ti-pieces of a purity of 99.99% had to be physically added onto the target. By adding 48 pieces in a row, as in Fig. 4-1, a chemical composition of $Ti_{0.5}Al_{0.5}N$ was expected to be achieved, with 48 pieces evenly distributed as in Fig. 4-2, a composition of $Ti_{0.75}Al_{0.25}N$.

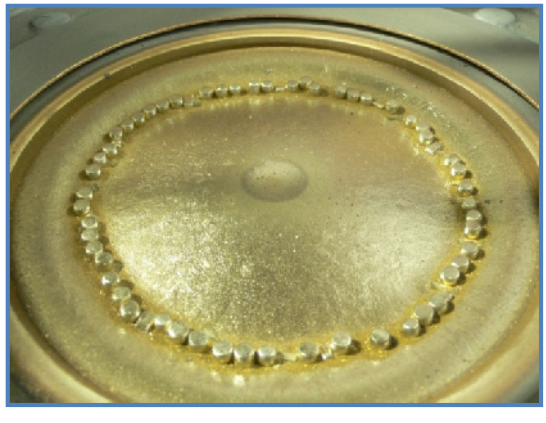

Figure 4-1: Addition of 48 Ti pieces, in a row, in order to achieve a $Ti_{0.5}Al_{0.5}N$ films.

Figure 4-2: Addition of 48 Ti pieces, evenly distributed, in order to achieve a $Ti_{0.75}Al_{0.25}N$ films.

Three samples were deposited to achieve an investigation over a wide area of chemical composition, with a first sample being a Ti-rich sample, another with a 50-50 Ti-Al ratio and a last being Al-rich. Furthermore, an investigation of the behaviour of different crystallographic structures was undertaken as the Ti-rich and 50-50 Ti-Al samples should have a single-phased cubic structure, and the Al-rich a single-phased wurtzite structure. To achieve the intended single-phase cubic structure and single-phase wurtzite structure, the deposition parameters as described in [28] were used.

Coatings with a high aluminium percentage are dark in colour, whereas high titanium percentage samples present the golden colour, which is characteristic for TiN.

4.1.2 Chemical composition analysis using EDX

The chemical composition of the deposited films was determined using energy dispersive X-ray analysis (EDX). The Oxford Instruments INCA EDX unit, which was attached to a scanning electron microscope (SEM) was used in Leoben. Table 4-1 presents the determined chemical compositions of the samples.

Added Ti-Pieces to Ti0.5Al0.5 target	Film chemical composition (in atom. %)			N_2		Ar		**Achieved chemical composition**
	Al [%]	Ti [%]	N [%]	sccm	$P(N_2)$ [Pa]	sccm	P(Ar) [Pa]	
0	30.3	16.9	52.8	10	0.258	7	0.176	$\mathbf{Ti_{0.36}Al_{0.64}N}$
48 (row)	27.4	21.7	50.9	1.6	0.063	13	0.346	$\mathbf{Ti_{0.44}Al_{0.56}N}$
48 (distr.)	15.4	33.4	51.2	1.6	0.063	13	0.346	$\mathbf{Ti_{0.68}Al_{0.32}N}$

Table 4-1: Achieved chemical composition of the deposited films.

4.1.3 Visual characterization and roughness measurements

Roughness measurements were undertaken using a 3D-optical microscope: Vertical Scanning White Light Interferometry (VS-WLI, ZYGO NewView 200). The roughness (Ra-value) was found to be 0.073 µm for c-$Ti_{0.68}Al_{0.32}N$, 0.023 µm for c-$Ti_{0.44}Al_{0.56}N$ and 0.011 µm for w-$Ti_{0.36}Al_{0.64}N$. Therefore the Ti-rich films were not as smooth as the other 2 films, which is supported by the surface and intensity map in Fig. 4-3, where more craters and surface irregularities can be seen.

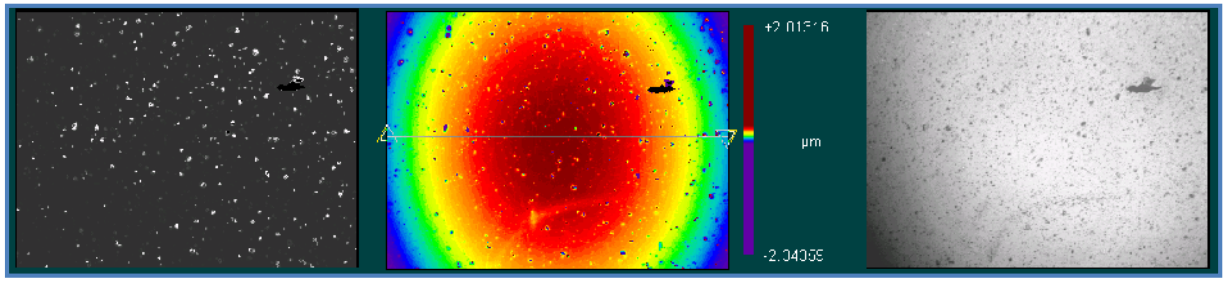

Figure 4-3: Surface map, intensity map and roughness profile of c-$Ti_{0.68}Al_{0.32}N$.

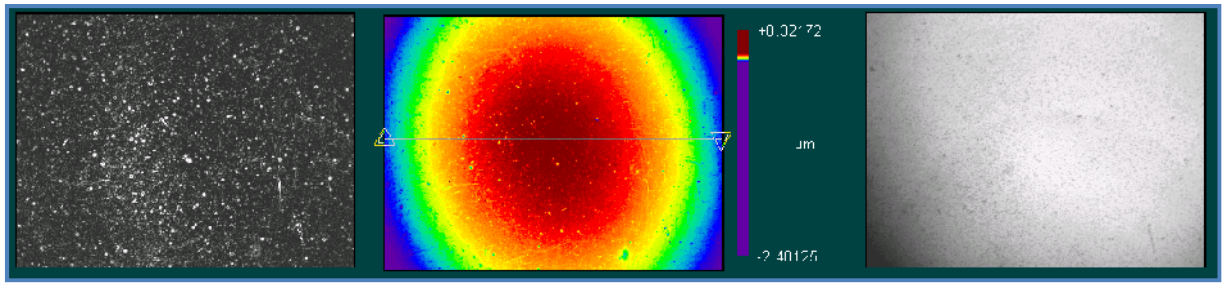

Figure 4-4: Surface map, intensity map and roughness profile of c-$Ti_{0.44}Al_{0.56}N$.

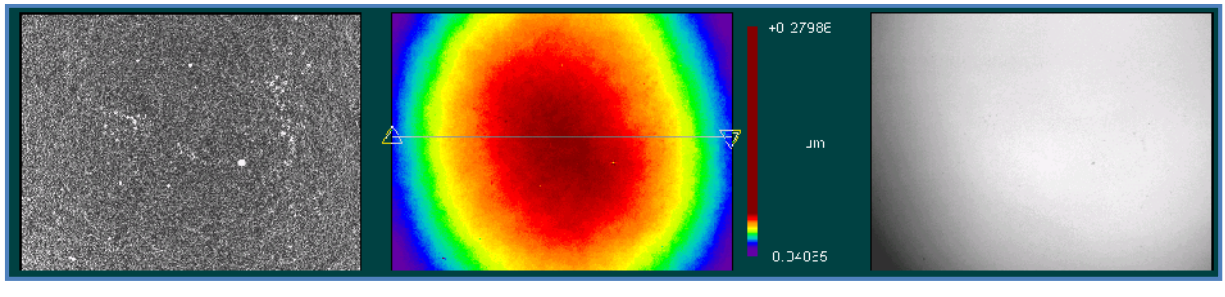

Figure 4-5: Surface map, intensity map and roughness profile of w-$Ti_{0.36}Al_{0.64}N$.

4.1.4 Crystallographic analysis with XRD

X-Ray diffraction (XRD) was used to characterise the crystallographic structure of the deposited films. XRD patterns of the TiAlN films were measured in both Leoben and London using a diffractometer in the Bragg-Brentano configuration with a Cu Kα radiation. As the X-rays have a large penetration depth, the XRD pattern also provides information about the underlying MgO substrate. The single crystal MgO yet only provides one single peak, facilitating the identification of the TiAlN peaks. Figure 4-6 presents the measured XRD pattern for the substrate, highlighting the MgO peaks.

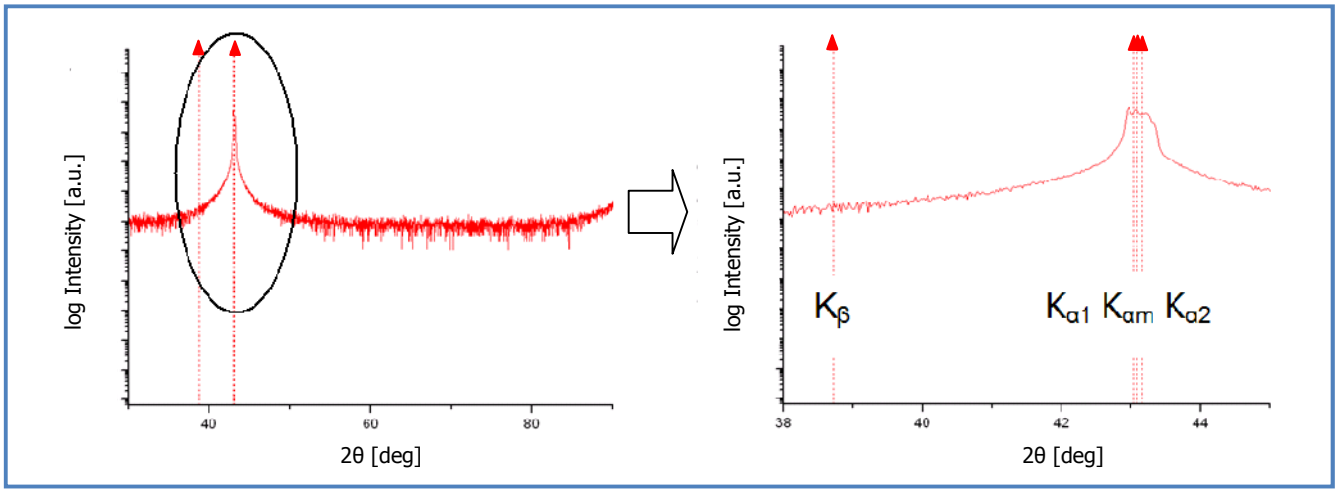

Figure 4-6: XRD pattern of single-crystal MgO with $K_{\alpha 1}$, $K_{\alpha m}$, $K_{\alpha 2}$ and K_{β} peaks.

The next figure, Fig. 4-7, presents the comparison of measured XRD patterns for the investigated films. The red vertical lines from triangles represent the characteristic peak position for the single phased-wurtzite structure of TiAlN, while the black vertical lines from squares represent the characteristic peak positions for a cubic $Ti_{0.5}Al_{0.5}N$ film.

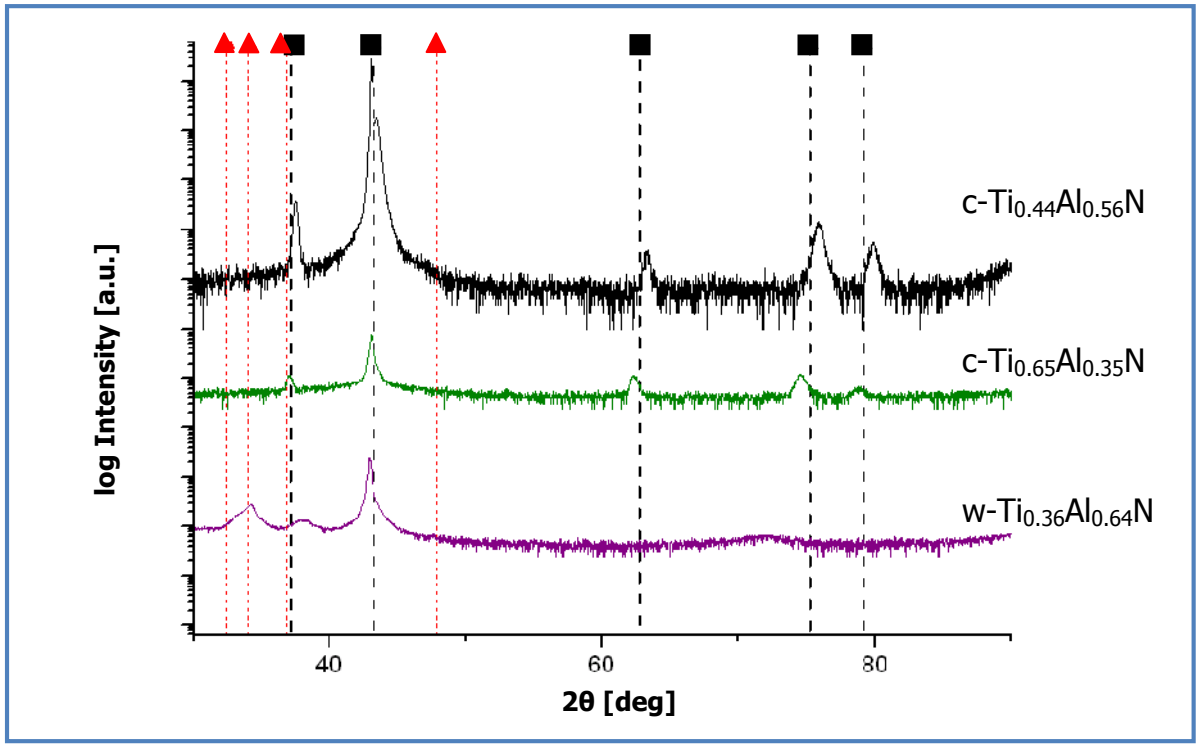

Figure 4-7: XRD patterns of deposited c-$Ti_{0.44}Al_{0.56}N$ (black), c-$Ti_{0.65}Al_{0.35}N$ (green) and w-$Ti_{0.36}Al_{0.64}N$ (violet) films.

Looking at the cubic peaks, a shift to the right was observed for sample $Ti_{0.44}Al_{0.56}N$ (black line), proving a high aluminum content. For the titanium rich sample (green line), $Ti_{0.68}Al_{0.32}N$, a shift to the left of the cubic peaks is observed, proving a higher titanium content of the films.

$Ti_{0.44}Al_{0.56}N$ and $Ti_{0.68}Al_{0.32}N$ have a single-phased cubic structure, whereas $Ti_{0.36}Al_{0.64}N$ exhibits a single-phased wurtzite structure. The deposited coatings can be considered to be near-epitaxial as the main coating reflex is at the position of MgO.

4.1.5 Heat treatment at 600°C

In order to investigate the effect of annealing on the mechanical properties, the c-$Ti_{0.44}Al_{0.56}N$ sample was chosen for heat treatment. The sample was heat treated in an argon atmosphere at 600°C for 24 hours in a furnace. An argon atmosphere was chosen in order to prevent oxidation.

To prove if a structural change had taken place upon annealing, further XRD scans were performed after the heat treatment. Fig. 4-8 presents XRD measurements performed before ($Ti_{0.44}Al_{0.56}N$-as-deposited) and after the heat treatment ($Ti_{0.44}Al_{0.56}N$-ann). No new peaks have developed, nor has there been a shift of existing peaks, therefore, the underlying structure as not been altered. This is in accordance with findings of Fox-Rabinovich et al., that showed that spinodal decomposition should not take place before ~700°C [29].

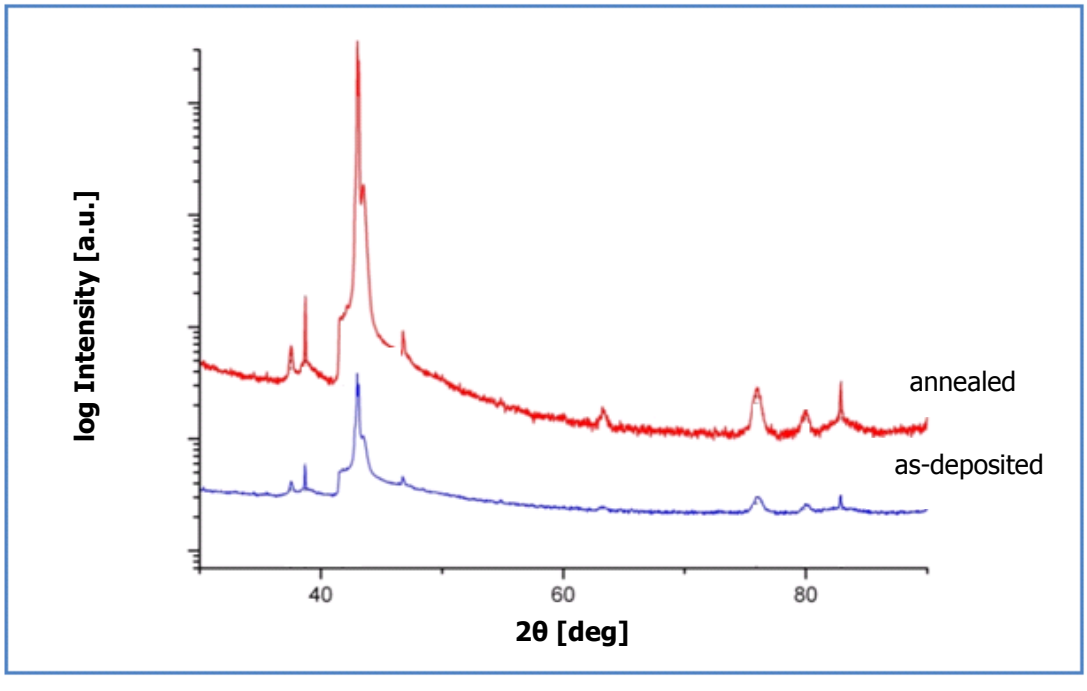

Figure 4-8: XRD patterns of the annealed (red curve) and as deposited (blue curve) $Ti_{0.44}Al_{0.56}N$ sample.

4.1.6 High temperature nanoindentation

The indentation instrument will be presented first. Then the procedure and finally the importance of the diamond area function of the tip will be discussed.

Instrumentation:

Since a high temperature nanoindentation system was not available at the Department of Physical Metallurgy and Materials Testing in Leoben, all experiments were carried out during a 4 months exchange program at the UK Structural Ceramic Centre based at the Imperial College in London. The nanoindentation system, which was used in this thesis, is the NanoTest platform from MicroMaterials Ltd and can be seen in Fig. 4-9.

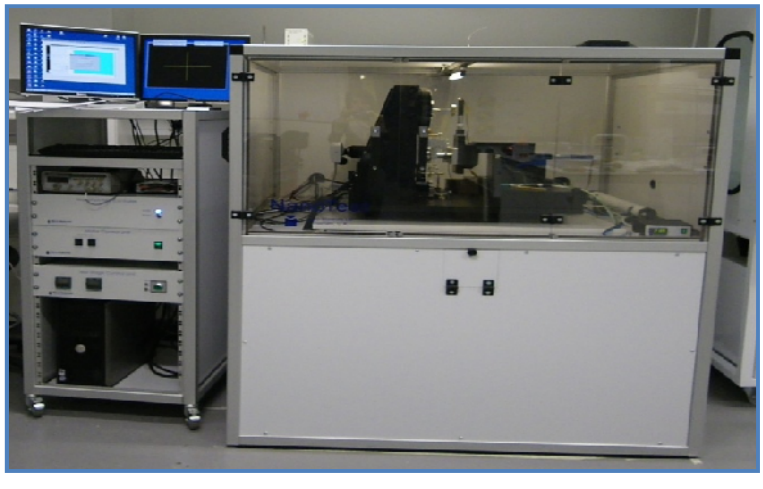

Figure 4-9: High temperature Nanoindentation system: NanoTest.

The indentation instrument consists of a vertically mounted pendulum, whereby the upper end is attached to a coil. When an electric current is supplied to the coil, the bottom of the pendulum, i.e., the Berkovich indenter moves towards the sample. The depth measurement is made by a plate capacitor which is located behind the pendulum. A schematic representation, as well as a picture can be seen in Fig. 4-10 and 4.11.

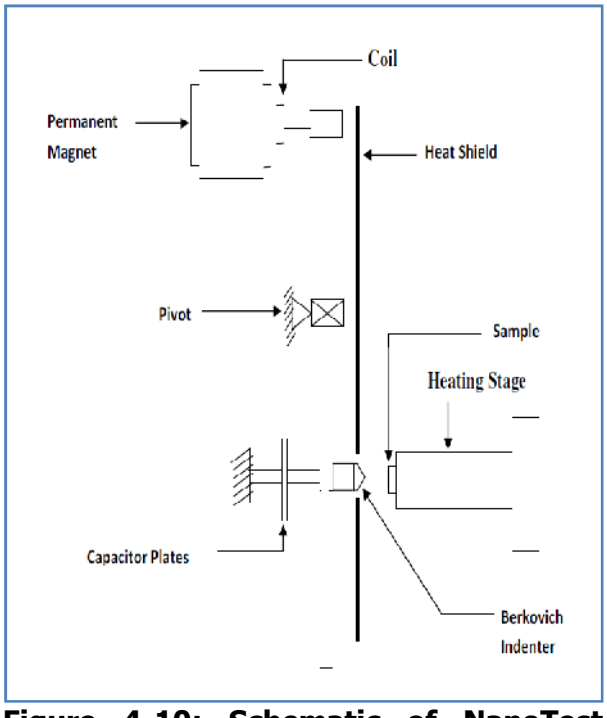

Figure 4-10: Schematic of NanoTest ceramic pendulum [21].

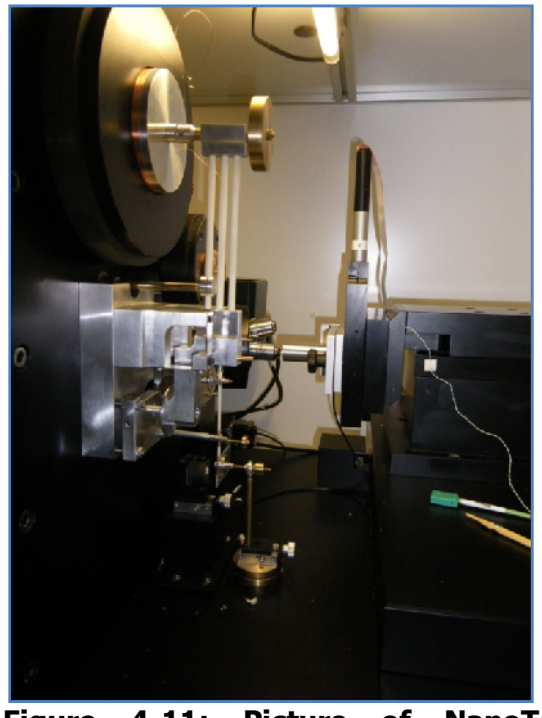

Figure 4-11: Picture of NanoTest ceramic pendulum.

Procedure:

Nanoindentation was performed between a temperature range of 25°C to 350°C. This temperature range was chosen for the following reasons:

- Diamond tips are known to readily oxidize over ~ 400°C [30].
- TiAlN is known not to oxidize in this temperature range [3].
- Age hardening effects, such as spinodal decomposition, should not take place in this temperature range [29].

A dual heater arrangement was used to minimise the effects of thermal drift. Two separate heaters were connected to the indenter and to the sample stage. The ramping up of the temperature took between 8 to 12 hours with an included holding and stabilizing time of 3 hours. Before indenting, an additional stabilisation time of 60 seconds was held at first contact, in order for thermal equilibrium between the tip and the sample to be reached.

Indenting:

The deposited samples had the following dimensions: 10 x 10 x 1 mm. The sample was cut into smaller pieces using an ISOMET-low speed saw. These were then glued onto a high temperature stage sample holder.

All samples were measured at 5 different temperatures: 25, 100, 200, 300 and 350 °C. Further on at every temperature, the samples were measured at 3 different loading rates: 0.1 ; 0.5 ; 1 ; 10 mN/s.

A series of 15 constant loading rate indents were made using a pyramidal high temperature diamond Berkovich tip. More than 1000 points were recorded per indent. Table 4-2 presents the forces, which were applied per loading rate.

Loading Rate [mN/s]	Min. Force [mN]	Max. Force [mN]	Increment [mN]
0.5	3	30	1.8
1	3	50	3.1
10	30	250	14.6

Table 4-2: Forces used for indentation at different loading rates.

A plot of a load-displacement curve from an indentation cycle is presented in Fig. 4.12.

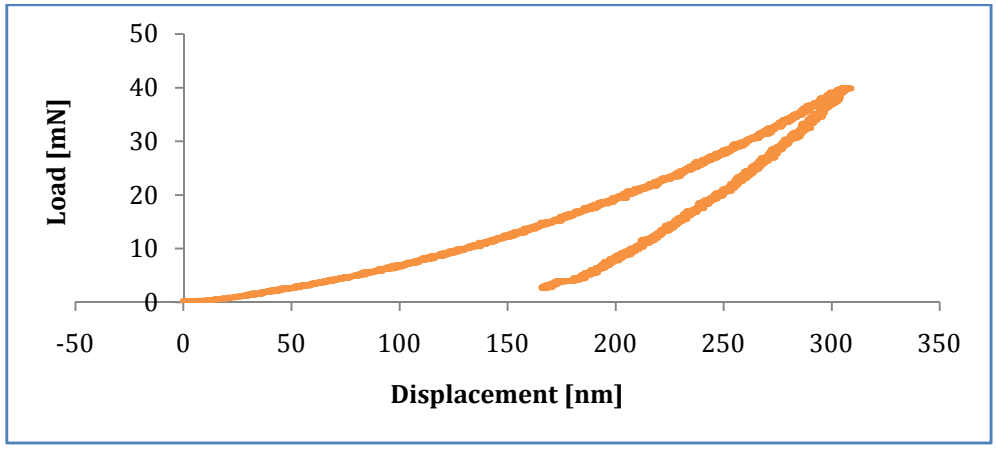

Figure 4-12: Measured load displacement curve for an indentation cycle of c-$Ti_{0.44}Al_{0.56}N$.

The following Fig. 4-13 presents the unloading and loading cycles for 15 consecutive indents:

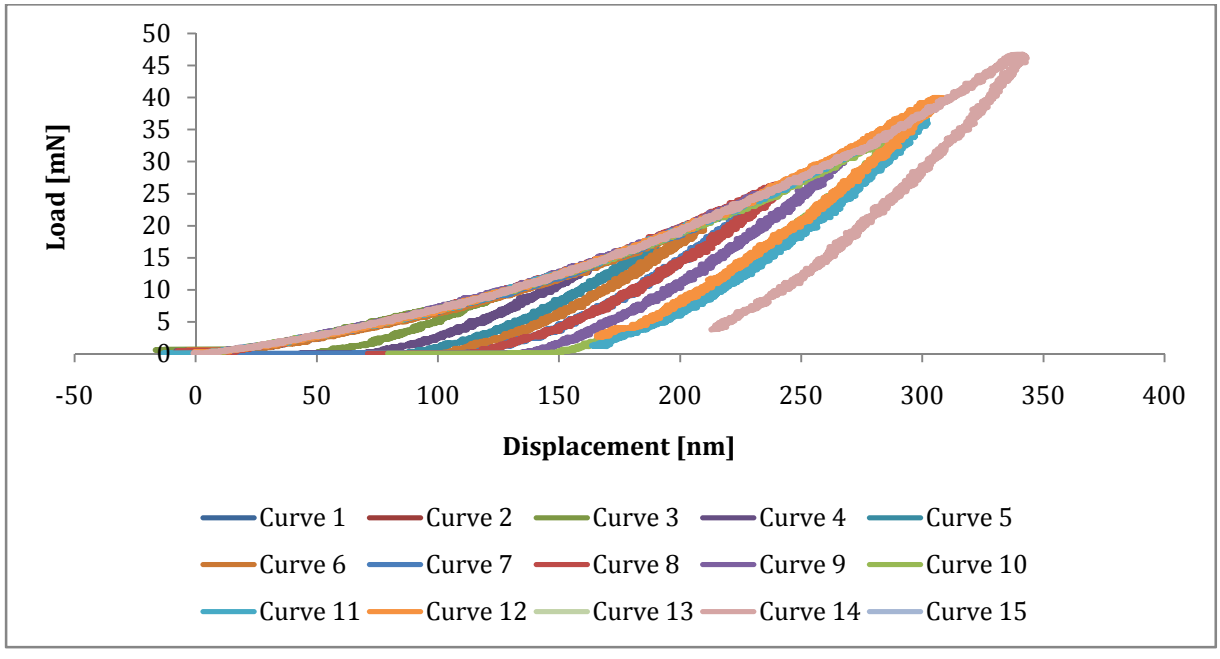

Figure 4-13: Load displacement curve for 15 consecutive indents on c-$Ti_{0.44}Al_{0.56}N$.

4.1.7 Calibration of the diamond area function

It is crucial to regularly measure the contact area of the diamond tip, also called the diamond area function. Due to friction, wear, high stresses and high temperatures, the tip wears out with time, thus changing its shape. It is therefore of utmost importance to measure the diamond area function as often as possible.

Fused silica was used to measure the diamond area function. Fused silica is used as it presents following advantages: a Young's modulus (E) of 72.67 ± 2.017 GPa and hardness (H) values of 7.75 ± 0.494 GPa, both of which do not change with depth. It has a small E/H value, which means it is quite soft and does not additionally wear out the tip. Finally it does not present pile up, which would lead to an underestimation of the area. [26]

The indentation data with a depth of less than 90 nm was disregarded, to prevent unreliable result. It was difficult to accurately determine the diamond area function under 90 nm. Choosing a minimum depth, also presents the further advantage of minimising the influence of surface roughness.

Compliance measurements of the hot temperature stage were further performed. For the high temperature sample stage, the compliance was found to be 0.72 nm/mN. This value was also used for the analysis of the hardness and Young's modulus data.

4.2 Characterization of mechanical properties using high temperature nanoindentation

The following results and discussions to these will be presented in this chapter: Hardness, Young's modulus, activation volumes and energies.

4.2.1 Hardness

Very few investigations have focused on the high temperature hardness of TiAlN films. Jindal et al. have found out that the hardness of TiAlN films decrease with increasing temperatures, however the following had not been taken into account: substrate effects [1]. Jindal et al. however investigated the films using microindents with an indentation load of 50 gF (500 mN). This is a very high load compared to the forces of 3-50 mN used at a loading rate of 0.5 mN/s in this thesis. The loads used by Jindal et al., are substrate influenced, as coatings were investigated, which are similar in thickness than the ones analysed in this thesis. Consequently the loads used by Jindal et al. are too high for proper hardness measurements.

4.2.1.1 Importance of the consideration of plastic depth:

Ceramic materials have high hardness to modulus (H/E*) values and are considered to be hard. Since the elastic component of the deformation is quite large it is crucial that it is taken into consideration. The elastic component is often neglected for low H/E* materials, such as metals [31]. Figure 4-14 and 4-15 shows the influence that taking the elastic component into account has on hardness and Young's modulus.

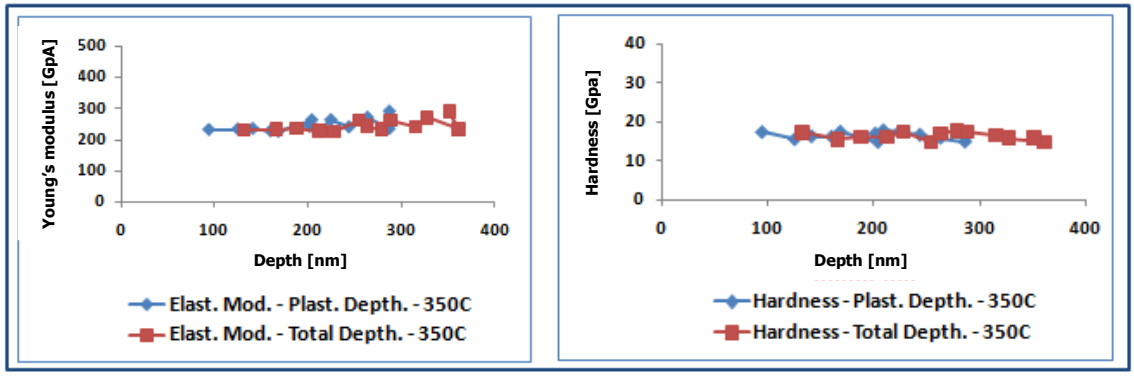

Figure 4-14: H and E values for w-$Ti_{0.36}Al_{0.64}N$ in dependence of total depth (red) and plastic depth (blue).

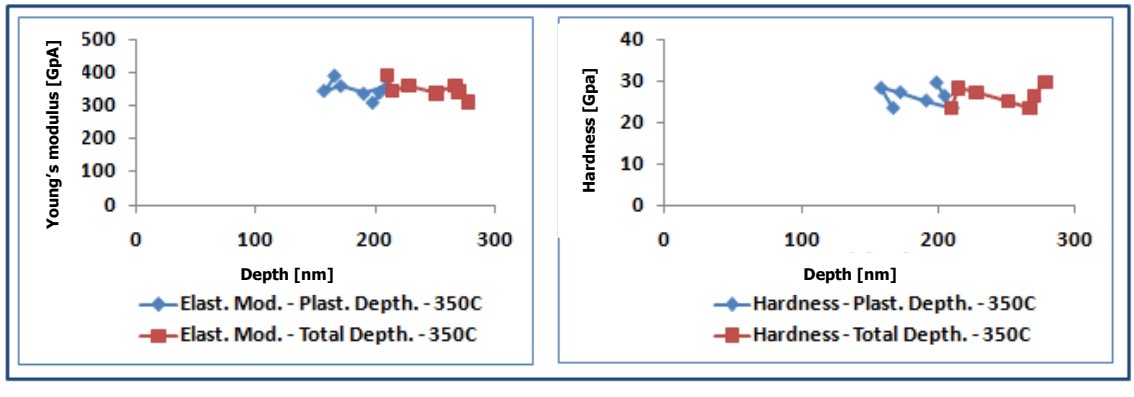

Figure 4-15: H and E values for c-$Ti_{0.44}Al_{0.56}N$-as-deposited in dependence of total depth (red) and plastic depth (blue).

As can be seen, the elastic component has an immense influence, resulting in a depth shift of up to 30% for the $Ti_{0.44}Al_{0.56}N$-as-deposited sample. Not taking the elastic component into consideration would lead to falsification of the ensuing calculations of the fundamental deformation parameters, with possible errors of one to two orders of magnitude.

4.2.1.2 Depth dependence of measured hardness values:

Figure 4-16 shows the influence of the hardness over the measured depth at 25°C for a low loading rate of 0.5 mN/s.

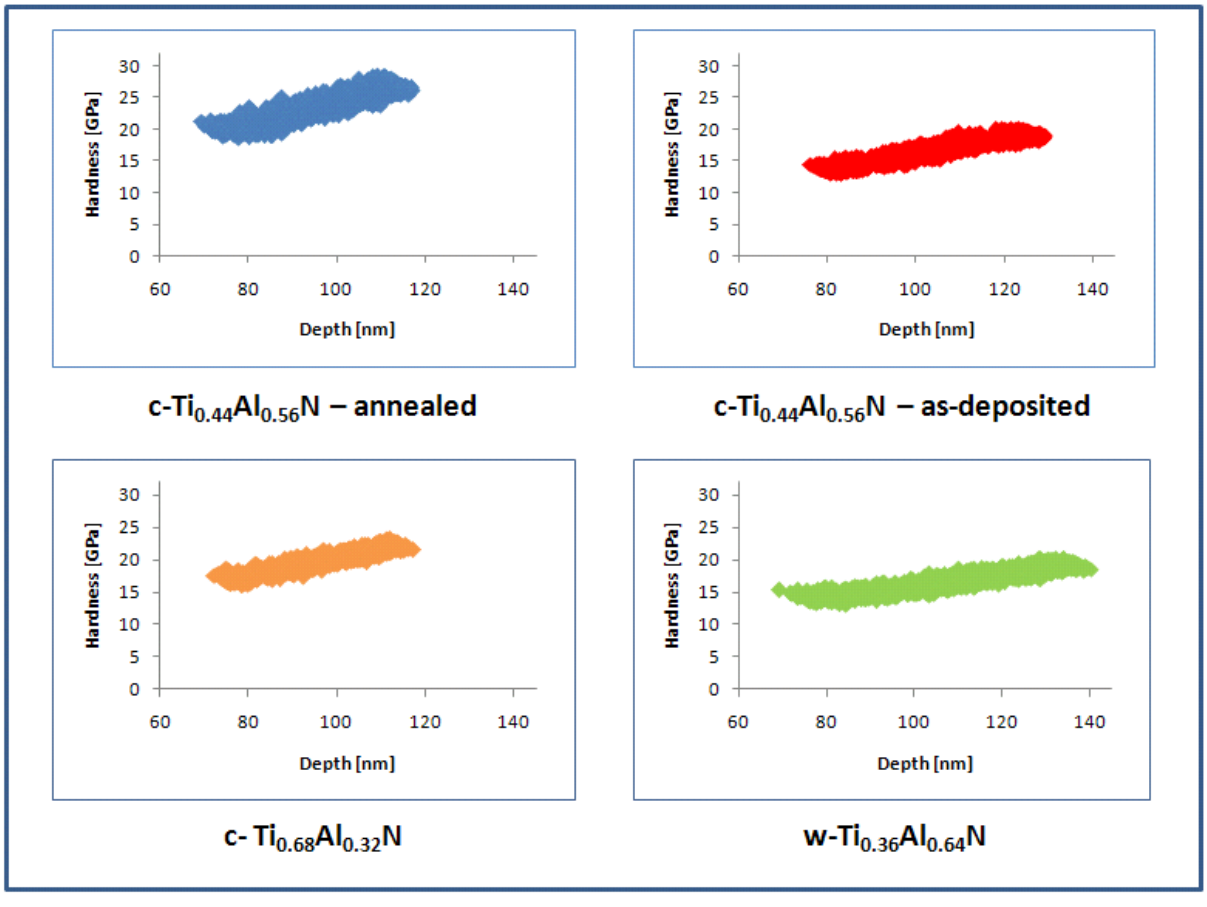

Figure 4-16: Hardness over depth for 25°C, at loading rate of 0.5 mN/s.

Figure 4-16 shows that the hardness increases with the indentation depth for all four samples (at room temperature, with a loading rate of 0.5 mN/s). This trend can be seen at all temperatures and all loading rates. This is not an artefact of the diamond area function as two different diamond area functions have been used to analyse the samples. Hultman et al. have grown TiAlN films epitaxially on MgO [27]. Films were observed, which were denser at the film-substrate interface and more porous at the top. Further on since MgO and TiAlN have different interatomic spacings, the films will be more strained at the interface. As the film grows thicker, the more relaxed and less strained it will be, thus resulting in a lower hardness at the top of the film.

Figure 4-17 shows the influence of the hardness over the measured depth at 350°C for a high loading rate of 10 mN/s.

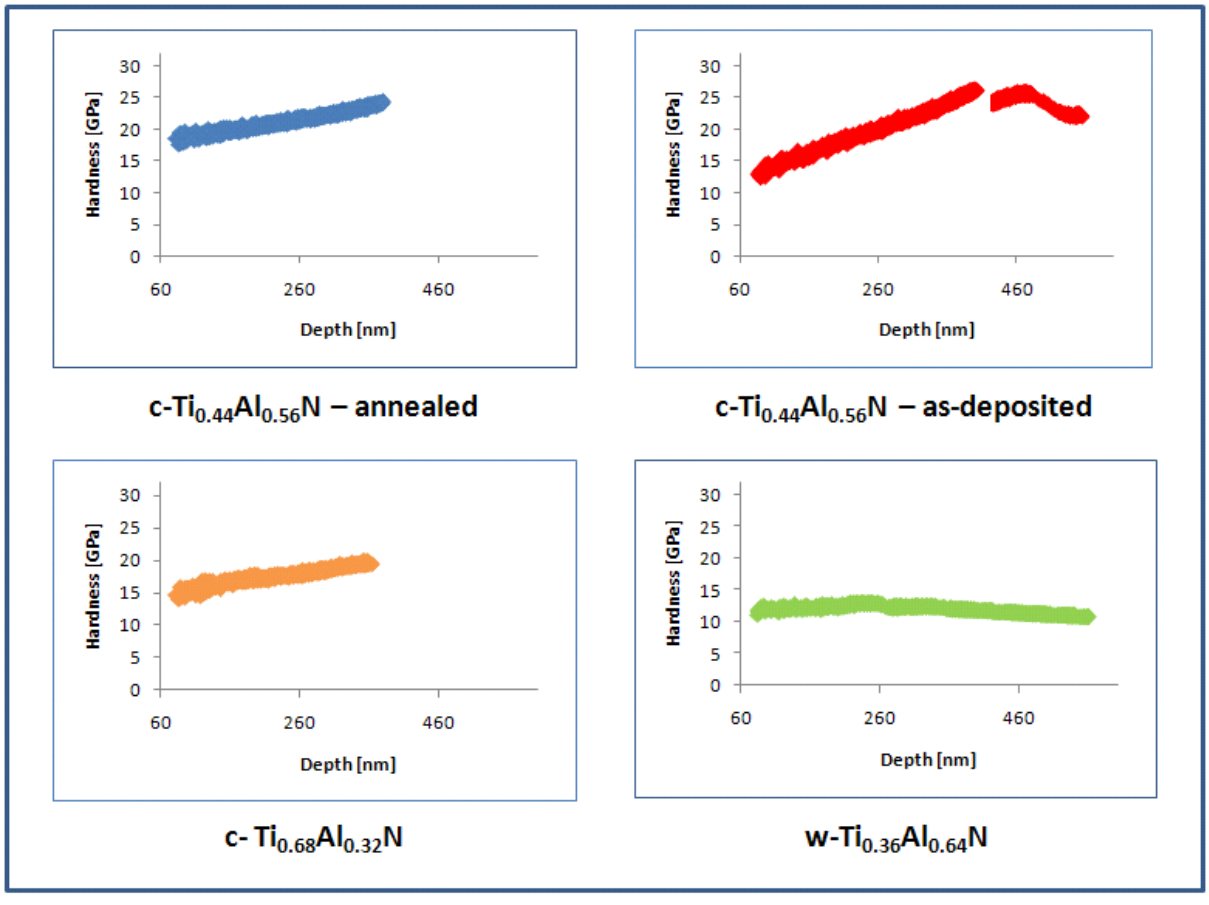

Figure 4-17: Hardness over depth for 350°C, at loading rate of 10 mN/s.

Figure 4-17 shows that for the wurtzite sample the hardness increases until around ~250 nm, after which it starts decreasing. 250 nm represents about 12% of the film thickness. After a depth of 12% of the film thickness, substrate effects from the softer MgO are noticeable and the hardness falls. The hardness does not fall for the c-$Ti_{0.68}Al_{0.32}N$ and c-$Ti_{0.44}Al_{0.56}N$ samples, as the maximum depth of 390 and 370 nm, respectively, is less than 10% of the film thickness in both cases.

The curve for the as-deposited c-$Ti_{0.44}Al_{0.56}N$ sample, presents an interesting phenomena, which appeared on all coatings predominantly at high temperatures and high loading. When testing with high loading rates of 10 mN/s, interruptions in the load-displacement curves appear. These jumps could have been caused by either crack formation or local delamination of the coating.

4.2.1.3 Temperature dependence of measured hardness values:

Hardness values for the four samples are plotted in Fig. 4-18 individually and in Fig. 4-19 together as a function of temperature.

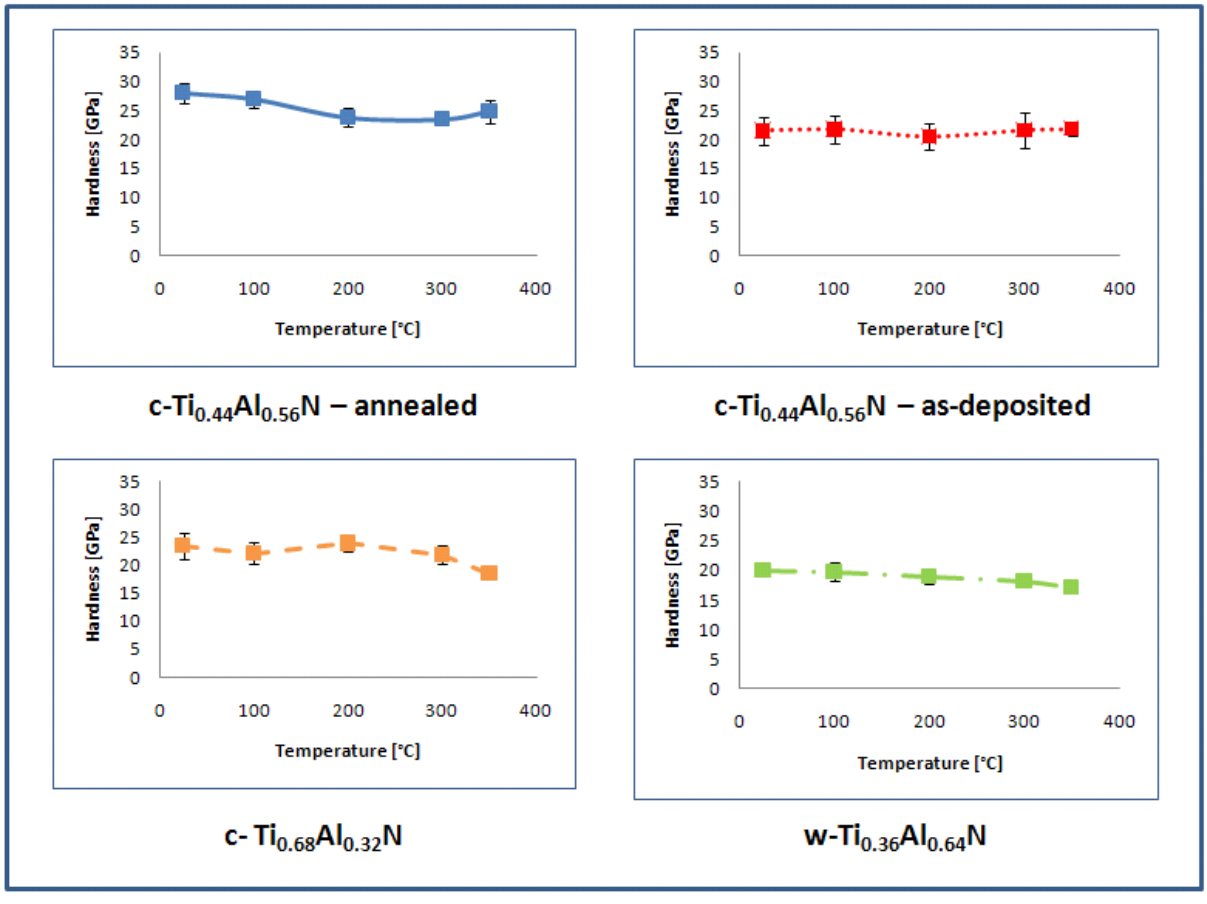

Figure 4-18: Hardness over temperature at loading rate of 1 mN/s.

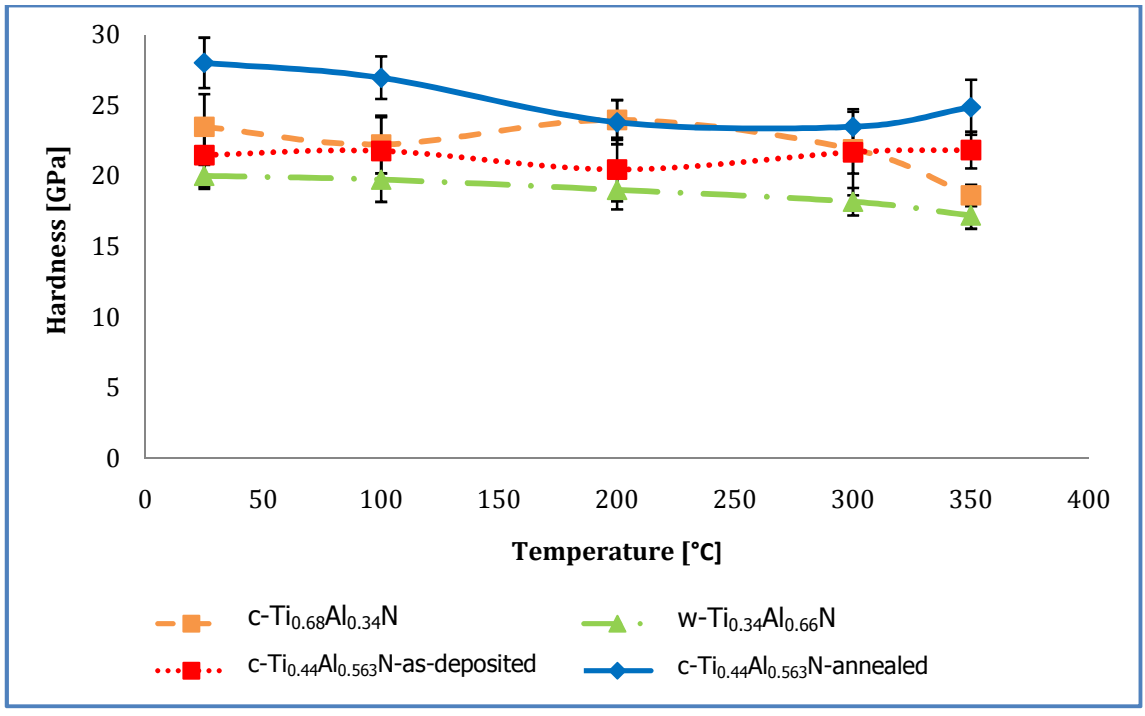

Figure 4-19: Comparison of hardness over temperature at loading rate of 1 mN/s.

The hardness of the wurtzite sample is lower than that of the cubic sample. This was expected and in accordance with previous findings [3]. The titanium rich c-$Ti_{0.68}Al_{0.32}N$ sample shows hardness values, which are slightly lower than the c-$Ti_{0.44}Al_{0.56}N$ samples. The hardness of the cubic samples is stable for the tested temperature range. However for higher temperatures, such as 300 and 350°C, the hardness decreases by 7% and 15%, respectively, compared to the room temperature hardness. For the wurtzite sample however, the hardness continuously decreases with the rising temperature. The hardness decrease is substantial, as only 85 % of the original room temperature hardness can be measured at 350C.

Interestingly enough the annealed c-$Ti_{0.44}Al_{0.56}N$ sample shows a higher hardness than the as-deposited $Ti_{0.44}Al_{0.56}N$ sample. To support the allegation that the annealed sample is harder than the as-deposited sample, the influence of the loading rate on both is plotted in Fig. 4-20.

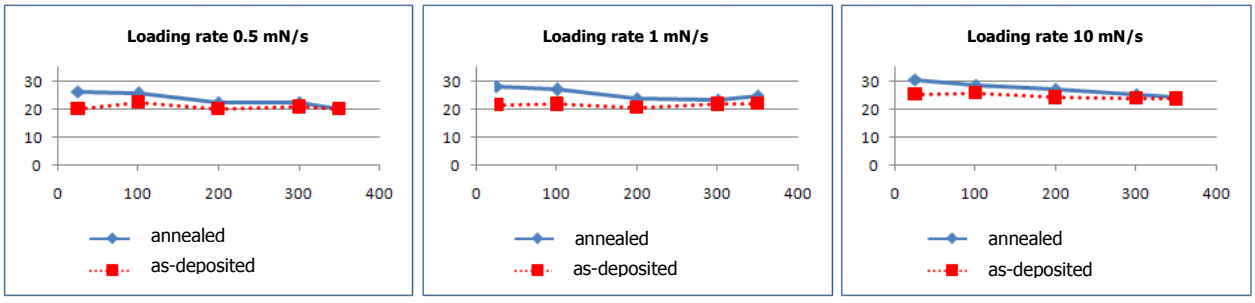

Figure 4-20: Comparison of the hardness of the as-deposited and annealed c-$Ti_{0.44}Al_{0.56}N$ sample at different loading rates.

Independently of the loading rate and the temperature, the annealed sample had higher H values than the as-deposited film. When annealing of a sample is performed, different mechanisms take place: reduction of compressive stresses caused by Frenkel pairs, annealing out of voids and vacancies (Schotky defects), rearrangement of vacancies, annihilation of opposite dislocations etc. [32]. These structural changes would lead to more relaxed structure and therefore a lower hardness should be measured.

The observation made in this investigation is exactly inverse. There are two possible reasons for this effect:

Influence of the diamond area function: The first possible influence is that of the diamond area function. The samples were nanoindented in the following order: as-deposited-c-$Ti_{0.44}Al_{0.56}N$, followed by c-$Ti_{0.68}Al_{0.32}N$ then finally annealed-c-$Ti_{0.44}Al_{0.56}N$. A diamond area function, which was determined after the third sample, was used to analyse all three coatings. During indentation at temperatures up to 350°C with high loading rates of 10 mN/s, the diamond tip undergoes severe strains and becomes substantially blunted. Meaning that the tip area of the samples, that were measured first, would be overestimated, as the tip was sharper at the beginning. This in consequence means, that the calculated hardness values of the first sample, the as-deposited-c-$Ti_{0.44}Al_{0.56}N$, should in fact be higher than those of the second c-$Ti_{0.68}Al_{0.32}N$ film.

Spinodal decomposition: The second possible influence could be because of spinodal decomposition. When annealing at high temperatures, TiAlN films decompose spinodally, resulting in a higher hardness as TiAlN decomposes into two coherent Ti-rich and Al-rich domains. The relatively low temperature at which the films were annealed, 600°C, is not known to show spinodal decomposition. Primary XRD analysis performed in chapter 4.1.4 did not reveal any changes in the crystallographic structure, which is possibly due to the fact, that the peaks, where structural changes take place are overshadowed by the substrate MgO peak. Therefore XRD analysis was performed anew on powder samples of cubic-$Ti_{0.44}Al_{0.56}N$, which were also annealed for 600°C for 24 hours under vacuum. The new XRD analysis on the powder samples can be seen in the following Figure 4-21 before and after annealing:

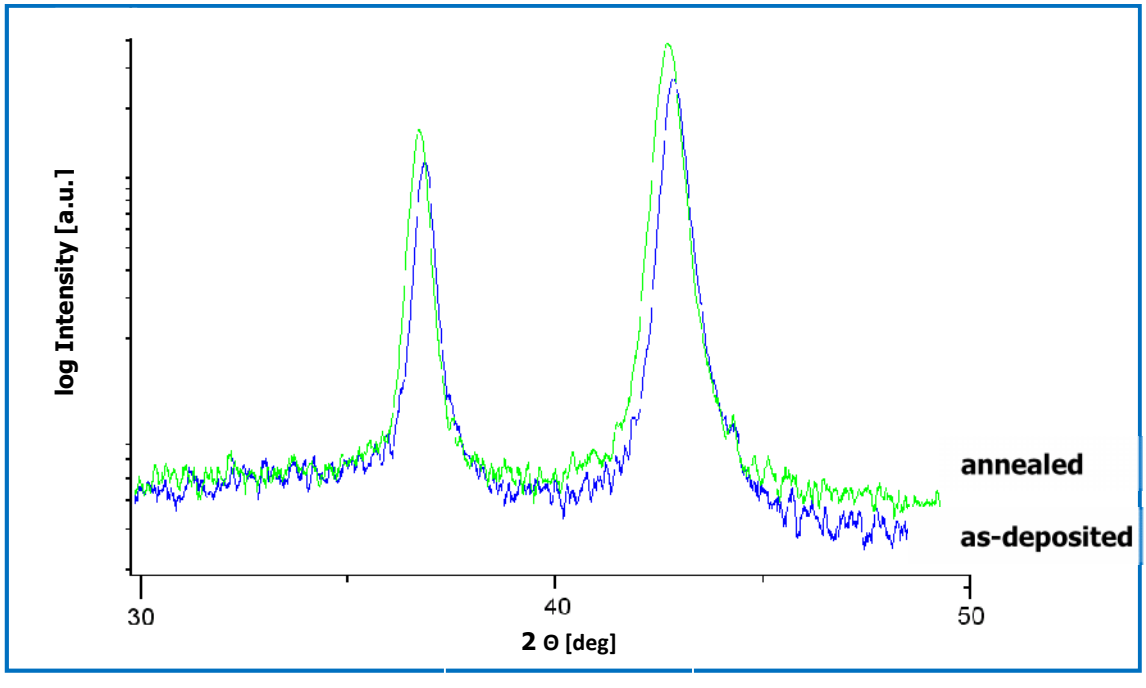

Figure 4-21: XRD analysis of powder- cubic-$Ti_{0.44}Al_{0.56}N$, annealed (green curve) and as-deposited (blue curve).

XRD analysis indicates an increase of the integral width from 0.55 to 0.59 suggesting ongoing spinodal decomposition to form Ti- and Al-rich cubic domains.

The next Figure 4-22 shows the effect of the aluminium concentration on hardness.

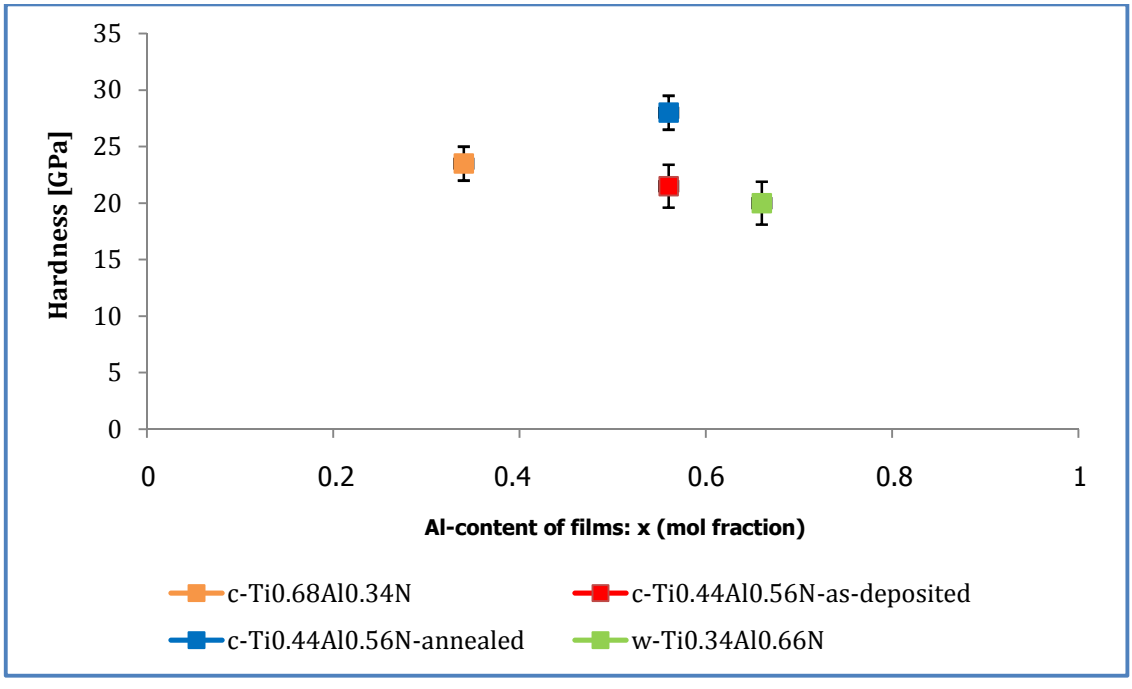

Figure 4-22: Hardness at 25°C in dependence of aluminium concentration in deposited $Ti_{1-x}Al_xN$ films.

The $Ti_{0.44}Al_{0.56}N$ samples having higher aluminium content are expected to have a higher hardness, as the smaller aluminium atom, which is substituted into the TiN, distorts the lattice. The distortion of the lattice results in a higher stressed state, whereby a higher measured hardness is the consequence. This is not the case in this investigation and cannot be observed for the following samples: c-$Ti_{0.68}Al_{0.32}N$ and c-$Ti_{0.44}Al_{0.56}N$. Once again, the influence of the blunting of the tip is used to explain the higher hardness values for the c-$Ti_{0.68}Al_{0.32}N$ sample. The annealed c-$Ti_{0.44}Al_{0.56}N$ sample is seen to have a higher hardness than the as-deposited state.

4.2.1.4 Loading rate dependence of measured hardness values:

Figure 4-23 presents the plot of the influence that the loading rate has on measured hardness values.

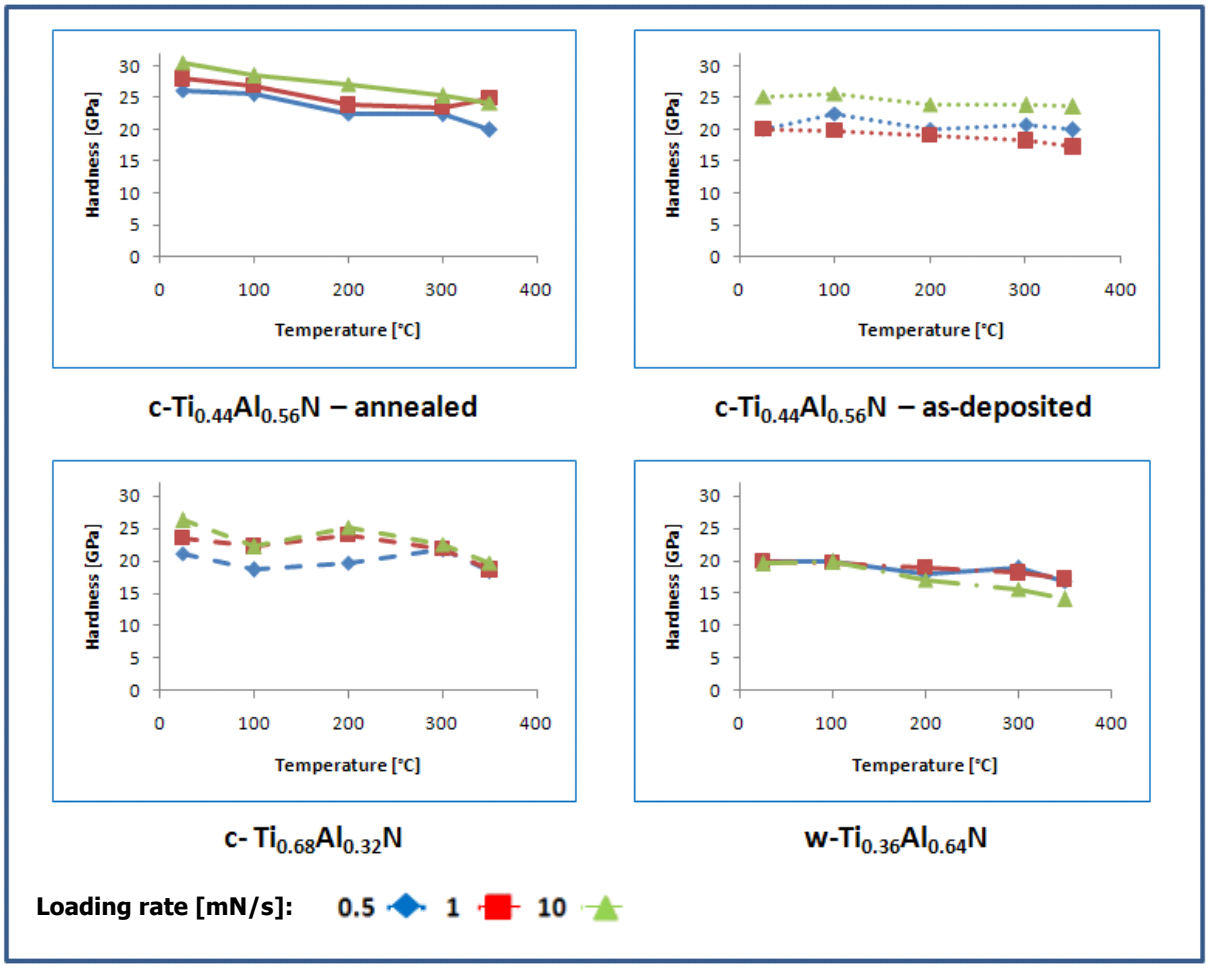

Figure 4-23: Hardness versus temperature at all 3 measured loading rates.

Let us consider two indents made at the same depth, but with a low and high loading rate. Through indentation, a plastic zone of a certain size is created. During nanoindentation with a low loading rate, the structure under the indent is given time to relax. With indentation at a high loading rate, the same amount of plastic deformation has to be created in much less time. There is less time for relaxation and a higher stressed state is created, i.e. higher hardness values are measured.

The fact that the higher the applied loading rate was, the higher the measured hardness values, holds true for all cubic samples. For the wurtzite sample, the

inverse phenomena can be observed. This can be explained with the influence of the substrate effect. The wurtzite sample is softer, as can be seen in the hardness measurements, than the cubic samples. When the same load is applied to both, the tip will travel deeper in the soft sample. The influence of the substrate effect will be even more pronounced, as the wurtzite sample is about 30% thinner than the cubic samples.

In the loading rate range of 0.5-10 mN/s all TiAlN films are rate sensitive. This is surprising as TiAlN films, which are hard ceramic coatings, are not expected to be loading rate sensitive.

In the loading rate range of 0.5 to 10 mN/s the hardness of all TiAlN films was found to be loading-rate sensitive. The hardness of c-$Ti_{0.44}Al_{0.56}N$-annealed increased by 17.2% from 26.1 to 30.6 GPa, $Ti_{0.44}Al_{0.56}N$-as-deposited increased by 24.8% from 20.1 to 25.1 GPa and $Ti_{0.68}Al_{0.32}N$ increased by 24.0% from 21.2 to 26.3 GPa. The loading-rate sensitivity of the wurtzite sample could not be measured because of the influence of substrate effects.

Furthermore, it is important to realise, that the hardness of the cubic TiAlN films already starts decreasing at a temperature of ~300°C. This is indeed relevant as these thin films are primarily used as protective coatings for high temperature applications.

4.2.2 Young's modulus

After hardness calculation, Young's modulus calculations were performed for the four samples and can be seen as single plots in Fig. 4-24 and to facilitate comparison in Fig. 4-25.

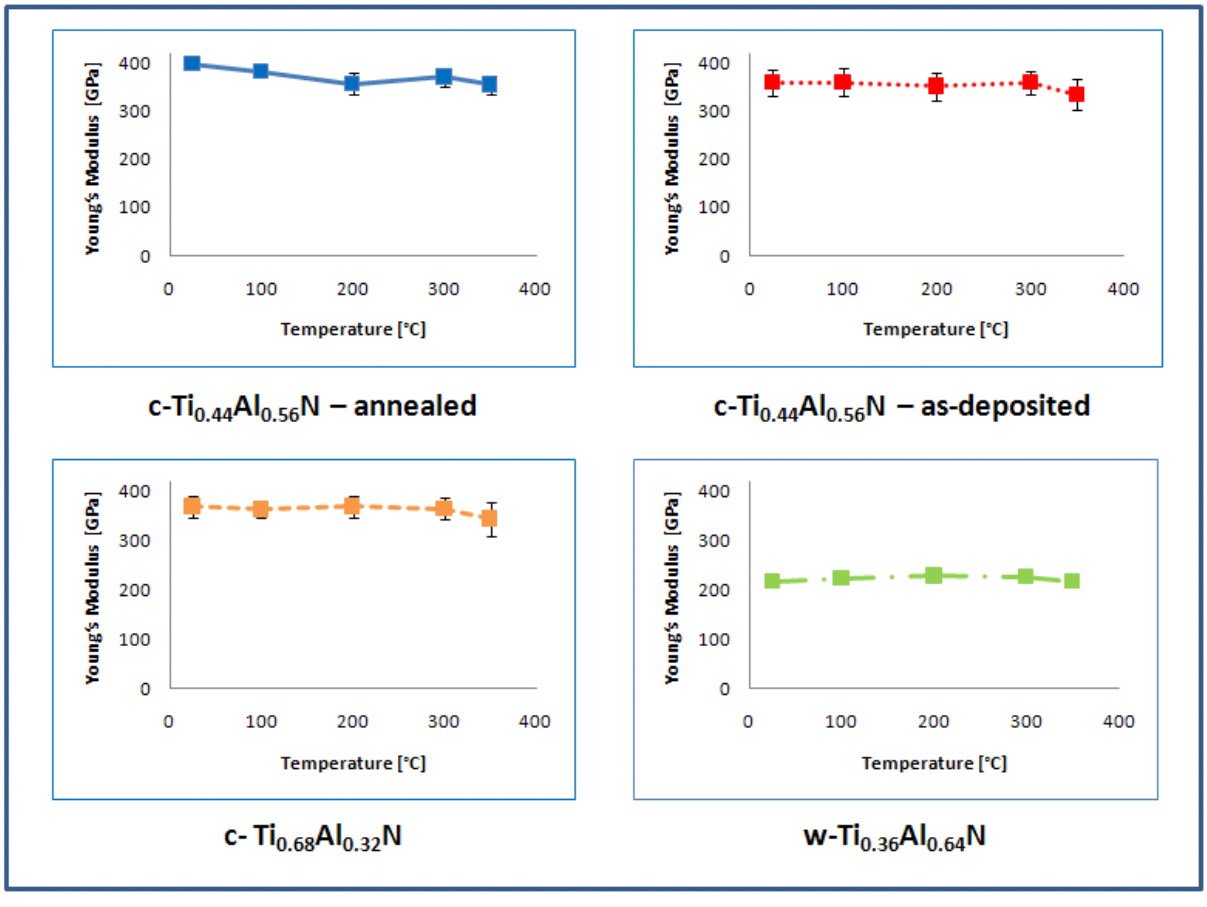

Figure 4-24: Temperature dependence of Young's moduli values of all samples for a loading rate of 1 mN/s.

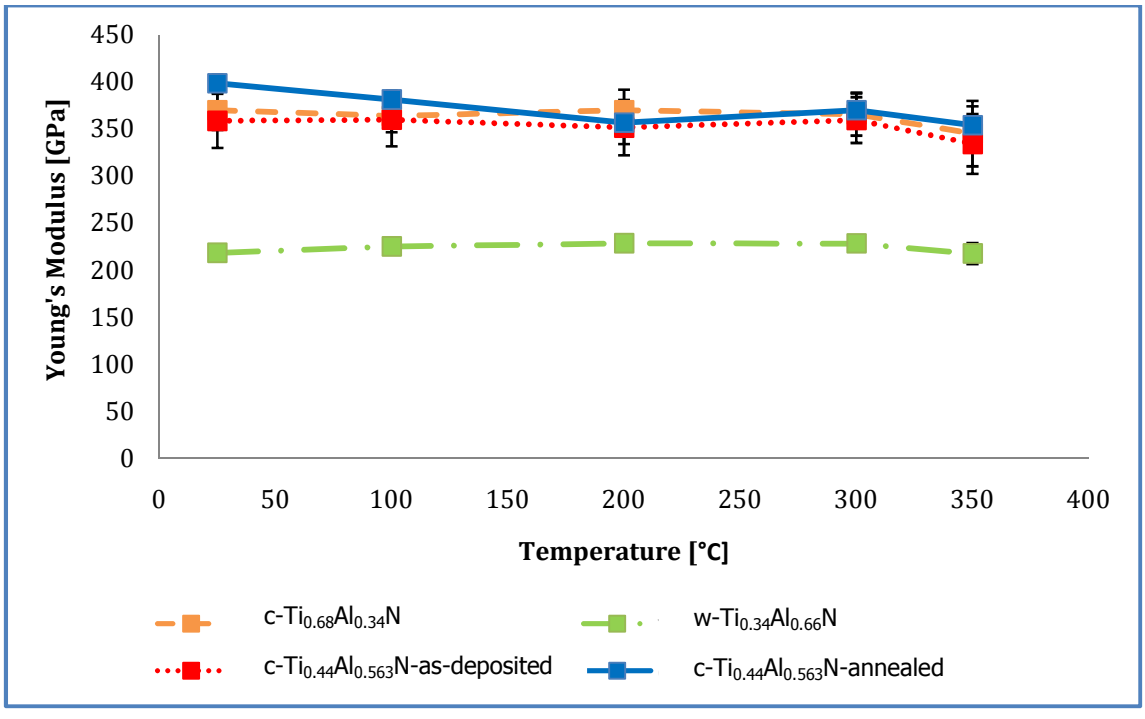

Figure 4-25: Comparison of measured Young's moduli values obtained from the 4 coatings at different temperatures for a loading rate of 0.5 mN/s.

TiAlN has a melting point of ~ 2950°C. The Young's modulus of materials is in general expected to be relatively insensitive to temperature until ~0.5 T_M [13].

The measured Young's moduli values for the cubic samples are 371 GPa for c-$Ti_{0.44}Al_{0.56}N$-ann., 352 GPa for c-$Ti_{0.44}Al_{0.56}N$-as-dep., 364 GPa for c-$Ti_{0.68}Al_{0.32}N$. The wurtzite sample has a much lower Young's modulus of 224 GPa.

Figure 4-25 graphically emphasises the fact that all cubic samples, have similar Young's moduli values, compared to the values for the wurtzite samples, which are much lower.

All samples present relatively constant Young's moduli values, which would be expected as the investigated temperature range of 25 - 350°C is much lower than ~0.5T_M.

4.2.3 Activation volume

The novelty of this thesis is the determination of the activation volumes of TiAlN films using nanoindentation, which has not been done previously. Yet the analysis and determination of activation volumes is not a new topic as such. Mulford et al. have already, calculated activation areas/volumes to determine dominant strengthening mechanisms in alloys [33].

After using numerous fitting functions with software packets, i.e., Matlab, it was observed that fitting the loading curve had drastic implications on the calculation of the activation volume; therefore, no fitting functions were used for any following calculations. For the extraction of activation volumes, the value at the beginning and the end of each curve was taken. All activation energies are further normalised to the volume of single dislocation by dividing it with b^3.

An activation volume is an indicator, for the size of the obstacle that has to be overcome by a dislocation.

- Is the activation volume smaller than one b^3, then the obstacles that would have to be overcome would be vacancies or point defects.
- Is the activation volume in the range of a few dislocations ($>b^3$), then multiple dislocations arrangements, such as forest dislocations, have to be overcome.
- Would the activation volume be in the range of multiple orders of dislocation volumes ($>10.b^3$), then this is a sign that larger structures, such as cell structures or grain boundaries, have to be overcome [21].

The elastic shear modulus μ is temperature dependant. All materials display a decreasing μ with increasing temperature. The following equation was used to calculate the values of μ at the indentation temperature [23].

$$\mu = \mu_o \left(1 + \frac{(T-300)}{T_M}\right) \frac{T_M}{\mu_o} \frac{d\mu}{dT} \quad (4\text{-}1)$$

Whereby:

μ = Elastic shear modulus at temperature T [GPa]

μ_o = Elastic shear modulus at 300 K [GPa]

T_M = Melting temperature [K]

$\frac{d\mu}{dT}$ = Temperature dependence of elastic shear modulus (which is -0.18 in case of TiC) [23].

The activation volume can be determined by using each and every single point of the load-displacement curve and then interpreted using a population-density-function. The activation volume can also be determined using the last point of the load-displacement curve. All the presented activation volumes were calculated using the last point. Chapter 4.2.3.1 will presents a calculation where all points of the curve are used for calculation.

4.2.3.1 Activation volume determination for loading rate 0.5 mN/s :

Figure 4-25 presents the measured activation volumes for all samples at a loading rate of 0.5 mN/s:

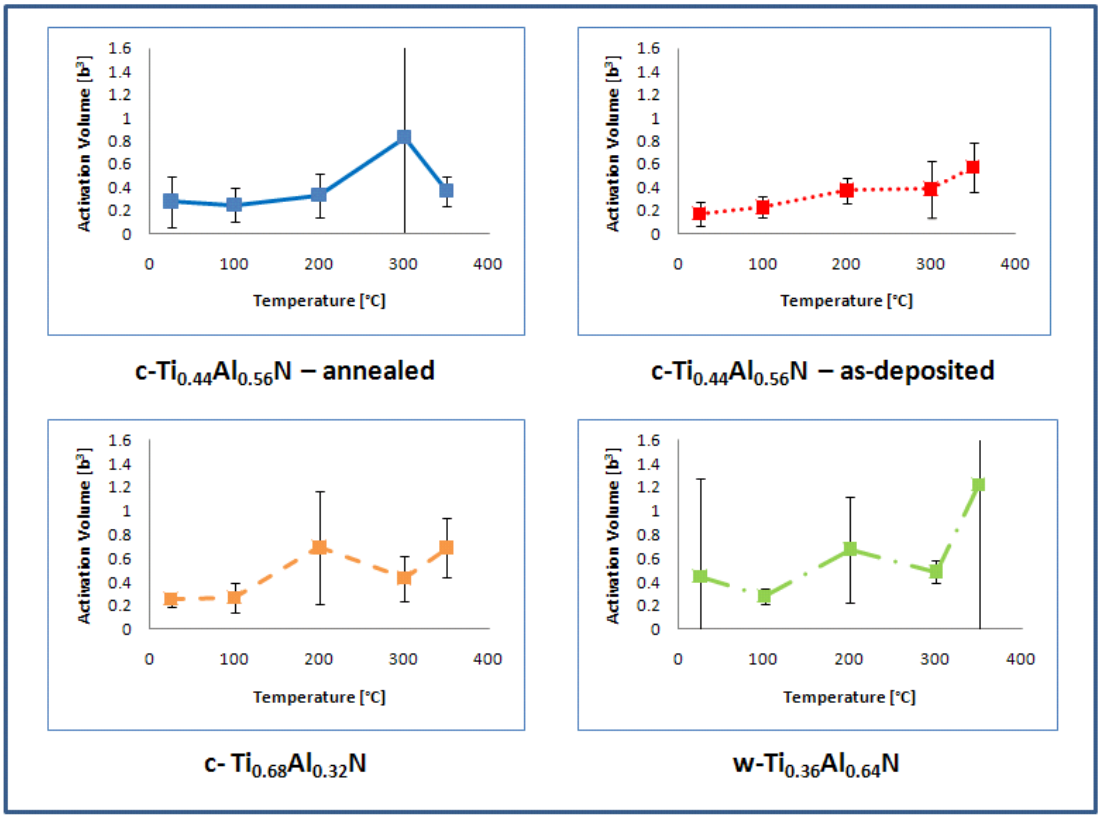

Figure 4-26: Activation volumes in dependence of the temperature for a loading rate of 0.5 mN/s.

The first observation that can be made is that most measured points present a high scatter of the values due to measuring fluctuations of mechanical or thermal nature. Preliminary indentation experiments were conducted at an even lower loading rate of 0.1 mN/s and presented an even higher scatter of the measured values. Therefore it can be concluded that future investigations should be conducted with loading rates higher than 0.5 mN/s, in order to exclude scatter.

The next Table 4-3 presents the activation volume values at room temperature and at 350°C, the percentage increase in the temperature range and the increase per Kelvin.

	Act.V. at 25°C [b^3]	Act.V. at 350°C [b^3]	% increase of V* in temperature-range	V*-increase per [K]
c-$Ti_{0.44}Al_{0.56}N$-annealed	0.27	0.37	34	2.86E-04
c-$Ti_{0.44}Al_{0.56}N$-as-deposited	0.17	0.58	236	1.17E-03
c-$Ti_{0.68}Al_{0.32}N$	0.25	0.69	171	1.26E-03
w-$Ti_{0.36}Al_{0.64}N$	0.45	1.22	175	2.20E-03

Table 4-3: Comparison of activation volumes of samples at 0.5 mN/s.

Figure 4-26 and Table 4-3 illustrate that the activation volumes rise with the temperature in the tested temperature range. Excluding the annealed sample, the activation volume values double over the temperature range. Further on, the values for the cubic samples lay lower than the wurtzite sample: around ~50% lower. The wurtzite sample presents the highest increase of V* per Kelvin, suggesting a higher dislocation activity than in other samples.

It can be further observed that the activation volumes for the annealed c-$Ti_{0.44}Al_{0.56}N$ sample are slightly higher (0.27) than the as-deposited state (0.37). On the other hand the V^* values rise less for the annealed sample c-$Ti_{0.44}Al_{0.56}N$ (34% of V*) compared to the as deposited c-$Ti_{0.44}Al_{0.56}N$ (236% of V*). The increment per degree is the lowest for c-$Ti_{0.44}Al_{0.56}N$-annealed, suggesting that dislocation activity is lower than in other samples. This would be supported by higher hardness values measured in the annealed sample in chapter 4.2.1.3. The higher the hardness of a sample, the higher the resistance to dislocation movement and therefore the lower the expected activation volume.

The following Figure 4-27, presents the four curves of Fig. 4-26 on one single chart to facilitate comparison:

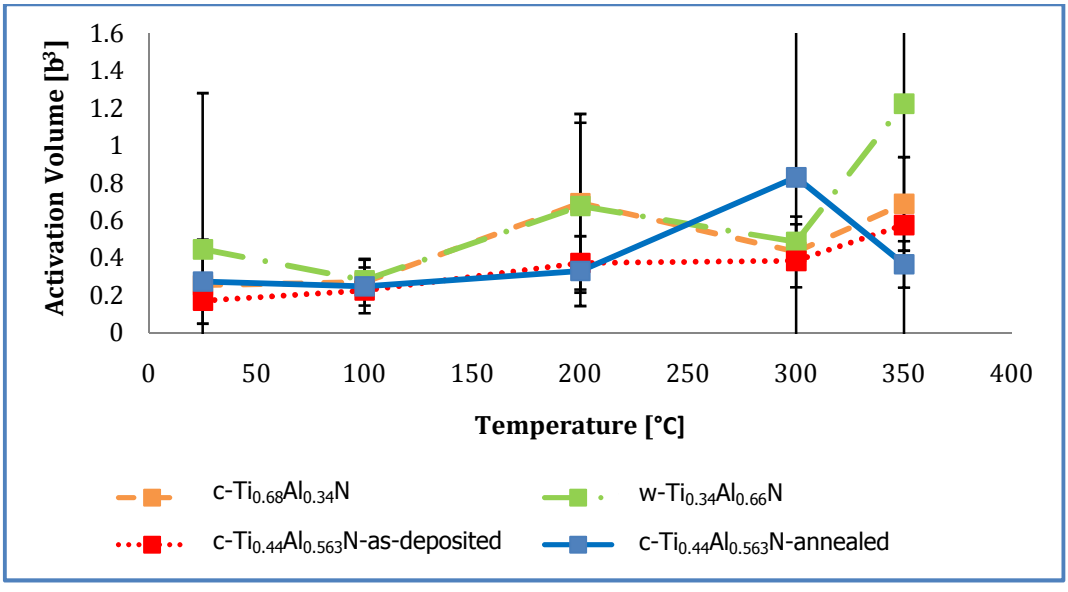

Figure 4-27: Comparison of the activation volumes in dependence of the temperature for a loading rate of 0.5 mN/s.

Figure 4-27 shows, similarly to the measured Young's modulus and hardness values, that all the cubic samples have very similar activation volume values.

Activation volume values for the cubic samples are in the range of 0.17 to 0.69 b^3. The activation volume values for the wurtzite sample ranged from 0.45 to 1.22 b^3. As discussed previously, an activation volume of less than 1 would suggest, that the dislocations are encountering obstacles, which are smaller than the volume of a dislocation, i.e. vacancies, point defects, etc. This seems to be the case at this low temperature range for the cubic samples. Yet on the other hand a shift of the obstacle-type encountered by the dislocations can be observed for the wurtzite sample. At low temperatures, the activation volumes lie under 1 b^3, yet as the temperature increases, the activation volume increases to values lying over the volume of a single dislocation. While moving dislocations were encountering obstacles smaller than a dislocation at room temperature, they are, at higher temperature, overcoming obstacles in the range of a dislocation.

4.2.3.2 Activation volume determination for loading rate 1 mN/s :

Figure 4-28 presents the measured activation volumes for all four samples, when a higher loading rate of 1 mN/s is used for indentation:

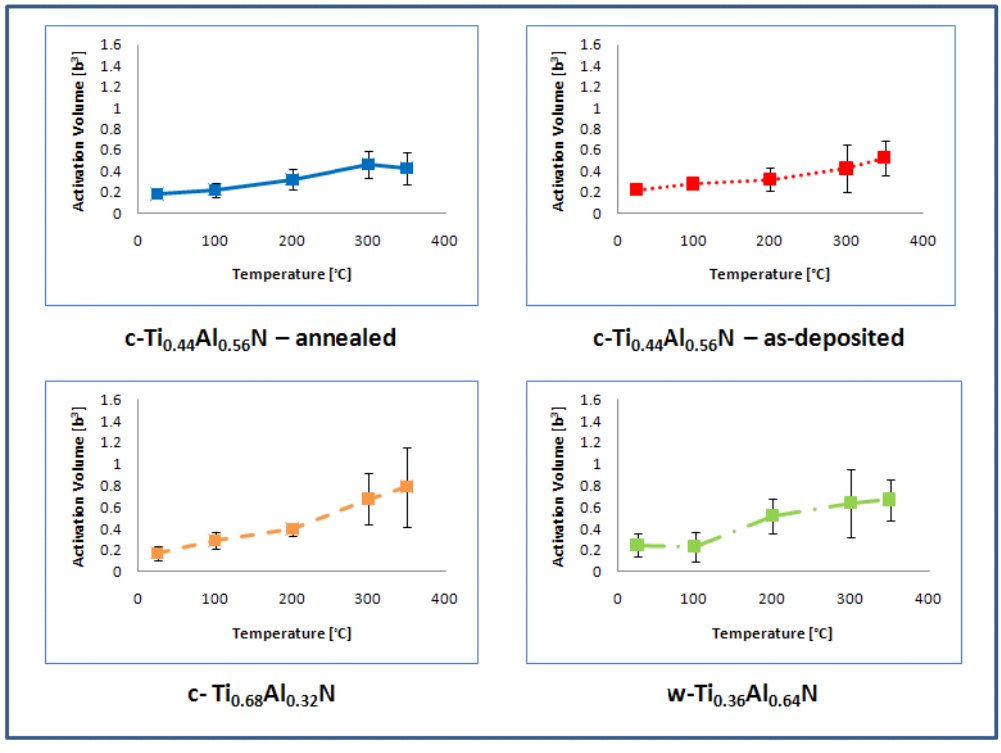

Figure 4-28: Comparison of the activation volumes in dependence of the temperature for a loading rate of 1 mN/s.

The following Figure 4-29, presents the combination of the four curves of Fig. 4-28 on one single chart to facilitate comparison:

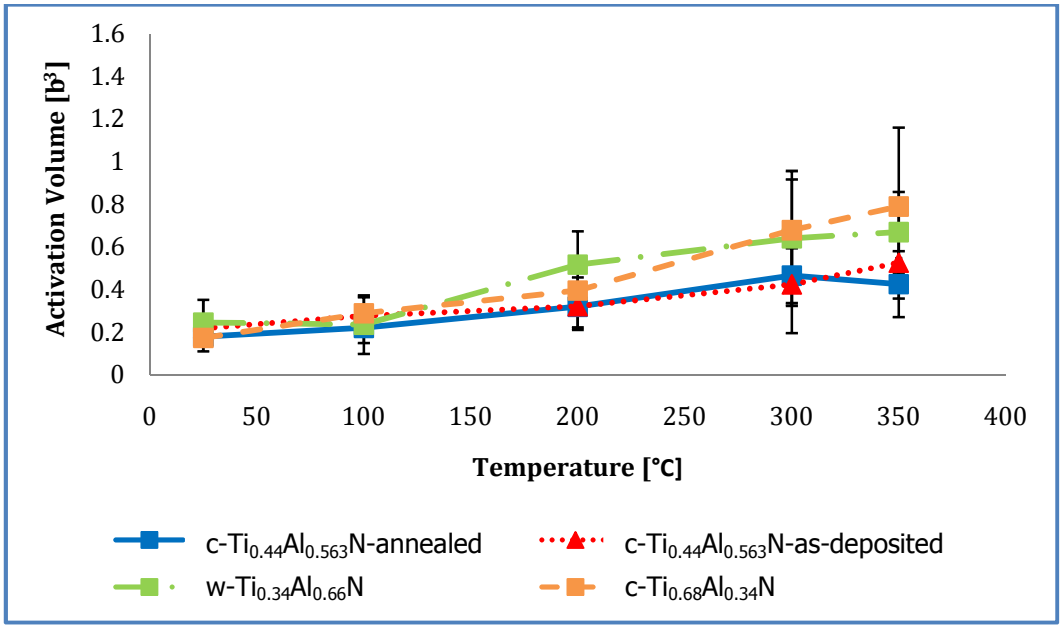

Figure 4-29: Comparison of the activation volumes in dependence of the temperature for a loading rate of 1 mN/s.

Figure 4-28 and 4-29 show that a similar trend can be observed for a higher loading rate of 1 mN/s. A positive finding is that the scatter has been reduced, when testing is performed at a higher loading rate.

The next Table 4-4 presents the activation volume values at room temperature and at 350°C, the percentage increase in the temperature range and the increase per Kelvin.

	Act.V. at 25°C [b^3]	Act.V. at 350°C [b^3]	% increase of V* in temperature-range	V*-increase per [K]
c-$Ti_{0.44}Al_{0.56}N$-annealed	0.18	0.43	138	7.14E-04
c-$Ti_{0.44}Al_{0.56}N$-as-deposited	0.22	0.53	142	8.86E-04
c-$Ti_{0.68}Al_{0.32}N$	0.17	0.79	356	1.77E-03
w-$Ti_{0.36}Al_{0.64}N$	0.24	0.67	173	1.23E-03

Table 4-4: Comparison of activation volumes of samples at 1 mN/s.

Similarly to the lower loading rate, the activation volume values for the cubic samples are in the range of 0.17 to 0.79 b^3. The activation volume values for the wurtzite sample were slightly lower ranging from 0.24 to 0.67 b^3. The error bars, for the wurtzite sample are higher than for the cubic sample.

For a loading rate of 1 mN/s, the increase per Kelvin is lower for the annealed c-$Ti_{0.44}Al_{0.56}N$ than for the as-deposited state and both are lower than the increase of the wurtzite sample are, compared in Table 4-4.

4.2.3.3 Activation volume determination for loading rate 10 mN/s :

Figure 4-30 presents the measured activation volume with a high loading rate of 10 mN/s:

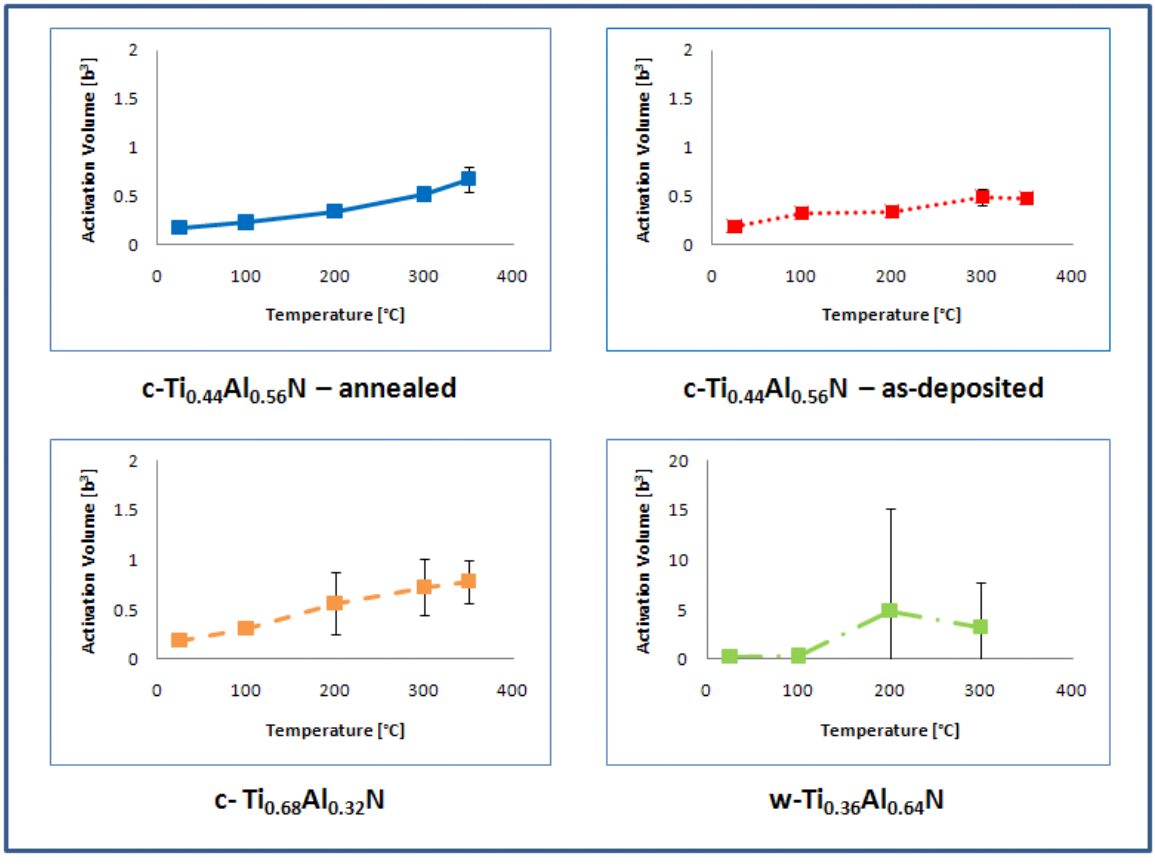

Figure 4-30: Comparison of the activation volumes in dependence of the temperature for a loading rate of 10 mN/s.

The following Figure 4-31, presents the combination of the four curves of Fig. 4-30 on one single chart to facilitate comparison:

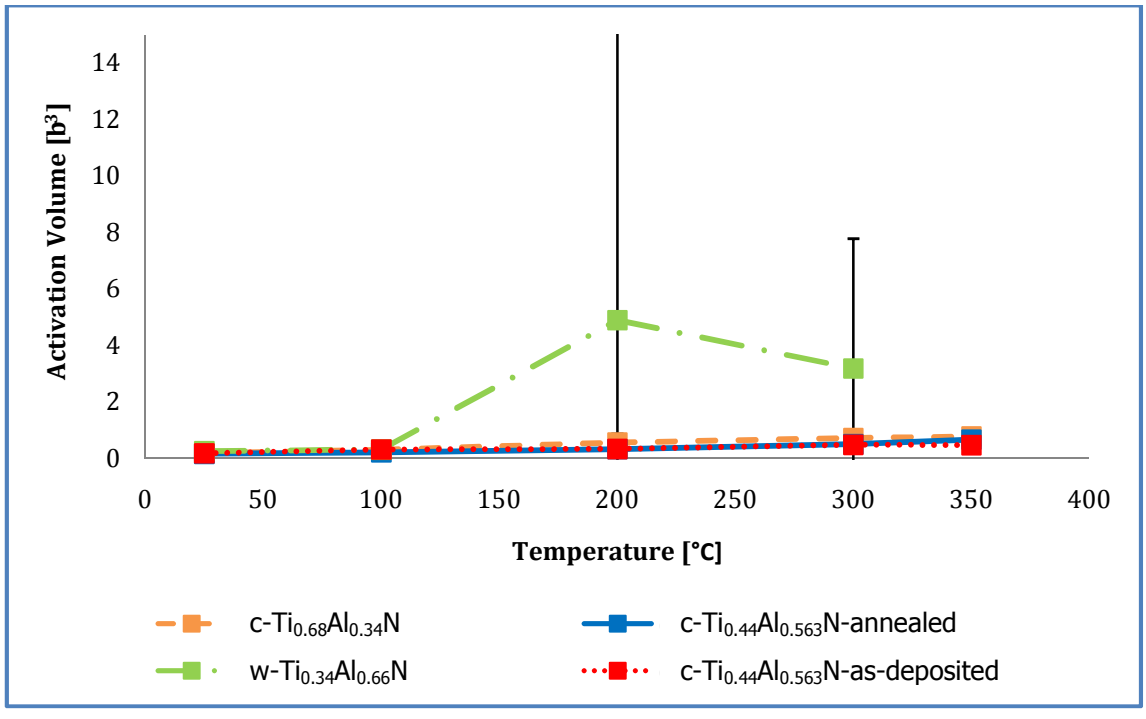

Figure 4-31: Comparison of the activation volumes in dependence of the temperature for a loading rate of 10 mN/s.

The activation volumes measured for the cubic samples are once again, very similar. The values found for the wurtzite sample lay at ~ 3.5 b^3. As the substrate effect is predominant for very high loading rates, as discussed in chapter 4.2.1.2, the activation volume rises as dislocation movement in the softer MgO substrate is also recorded. This is further illustrated in the next Table 4-5:

	Act.V. at 25°C [b^3]	Act.V. at 350°C [b^3]	% increase of V* in temperature-range	V*-increase per [°C]
c-$Ti_{0.44}Al_{0.56}N$-annealed	0.17	0.67	394	1.43E-03
c-$Ti_{0.44}Al_{0.56}N$-as-deposited	0.18	0.48	267	8.57E-04
c-$Ti_{0.68}Al_{0.32}N$	0.19	0.78	411	1.69E-03
w-$Ti_{0.36}Al_{0.64}N$	0.27	3.18	1178	8.31E-03

Table 4-5: Comparison of activation volumes of samples at 10 mN/s.

Table 4-5 shows that the percentage increase for a loading rate of 10 mN/s are much higher. Comparing the annealed sample at different loading rates, an increase of 34% at 0.5 mN/s, 138% at 1 mN/s and 267% at 10 mN/s, which is a clear indication of loading rate sensitivity, which is why the next sub-chapter will focus on this topic.

4.2.3.4 Loading rate dependence of activation volumes:

The loading rate sensitivity was investigated in depth on the c-$Ti_{0.68}Al_{0.32}N$ sample, as seen in Fig.4-32:

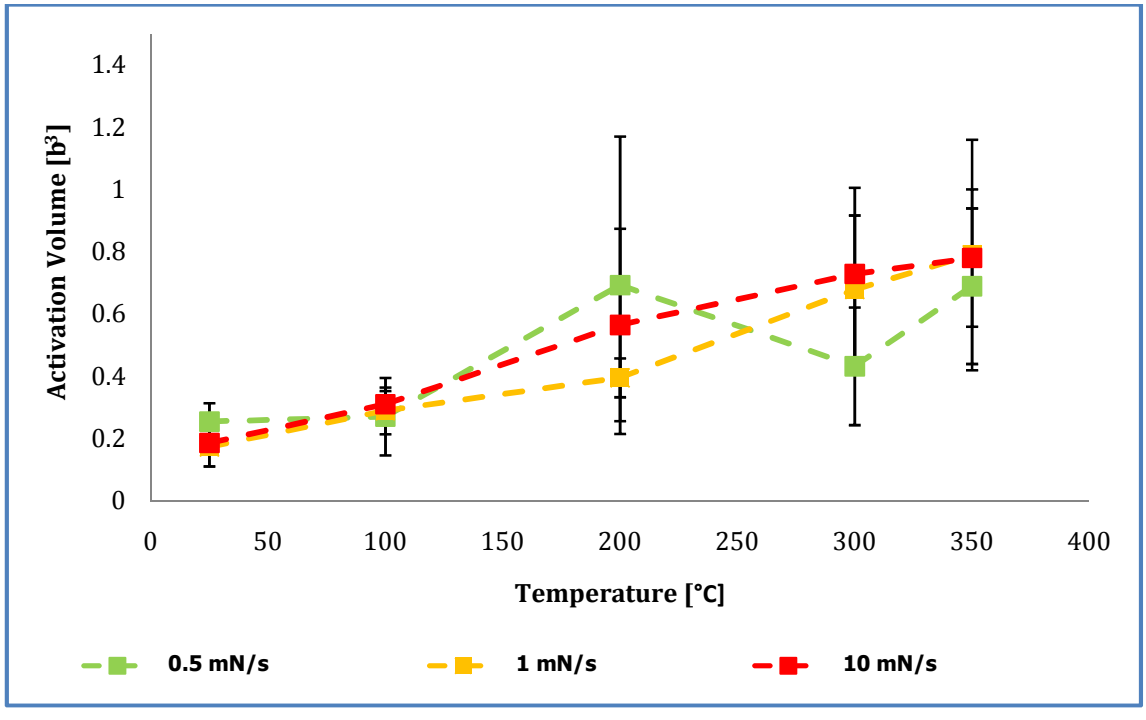

Figure 4-32: Loading rate sensitivity of measured activation volumes on the example of c-$Ti_{0.68}Al_{0.32}N$.

Similarly to the hardness, the activation volume values also show a loading rate sensitivity, lying slightly higher at higher loading rates. This would not mean, that the obstacles encountered by the dislocation change, but that there is a higher resistance to dislocation movement, due to the additional stress induced in the plastic zone at higher loading rates, as discussed in 4.2.1.

In Fig. 4-32, it can be seen that apart from 200°C, the trend can be seen, that the higher the loading rate, the higher the measured activation volume.

4.2.3.5 Activation volume of bulk aluminum as comparison:

To fully understand, activation volumes, when determined with nanoindentation, a comparative study was made, by indenting a metal. Soft metals, such as aluminium, are known to primarily deform by dislocation-dislocation interactions. The activation volume, would therefore expected to be larger than 1, as dislocation encounter single, but moreover, a multitude of dislocation, often in form of dislocation forest. This time an alternative population density function (PDF) method was used to evaluate the activation volumes. The PDF method not only uses the last point of the load-displacement curve to calculate activation volumes, but uses each and every one of the 1000+ measured points. Therefore, different activation volumes are measured. This can be explained by the fact, that during indentation, different mechanisms take place: movement of single point defects, single dislocations, kink and jog movement, etc. These measured activation volume values are then summed-up in a temperature range.

The following diagram in Fig. 4-33 presents the PDFs for the c-$Ti_{0.56}Al_{0.44}N$-as-deposited sample and the bulk aluminum:

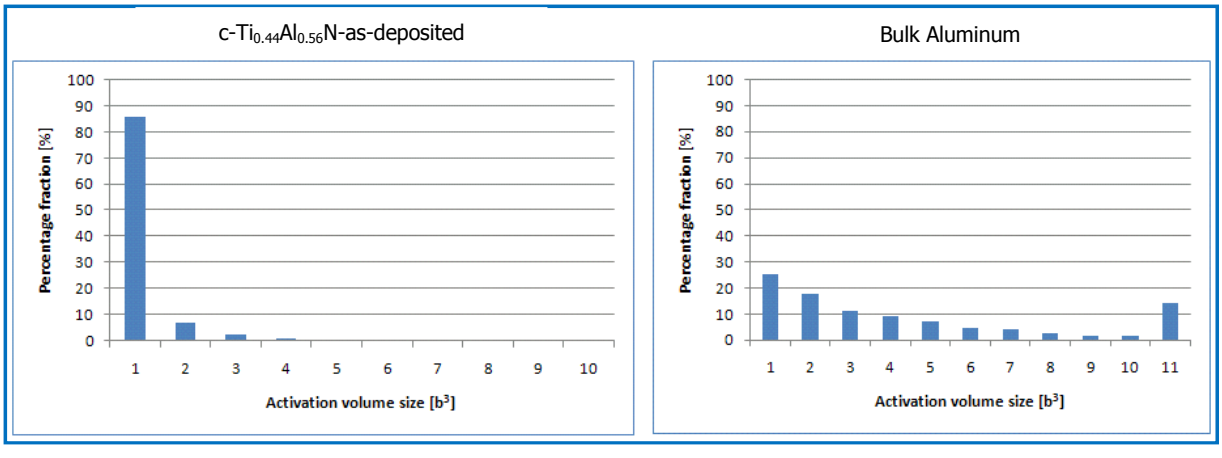

Figure 4-33: Population density function for the activation volumes of c-$Ti_{0.56}Al_{0.44}N$-as-deposited and bulk aluminum.

The first observation that can be made for the cubic-$Ti_{0.56}Al_{0.44}N$ sample is that over 85% of all the activation volume values are between 0-1 b^3. For bulk aluminum on

the other hand measured activation volumes are much higher and dispersed over a higher range, where 85% of the data lies between 0-10 b^3 for bulk aluminum. 95% of all the data for the cubic-$Ti_{0.56}Al_{0.44}N$ sample lay between 0-4 b^3 and between 0-25 b^3 for the aluminum sample.

The hereby determined activation volumes for bulk aluminum are 25 to 50 times higher than the activation volumes extracted for wurtzite and cubic TiAlN respectively. This is a positive finding, as it proves that the nanoindentation method is sensitive enough to pick up very subtle dislocation activity for hard ceramic coatings. When the last point of the load-displacement curve is used to measure the activation volume, the determined values lay much lower, between 1.5 and 5.5 b^3.

Figure 4-34 presents the activation volumes calculated using the last point of the load-displacement curve, illustrating the high activation volumes of aluminum compared to TiAlN films.

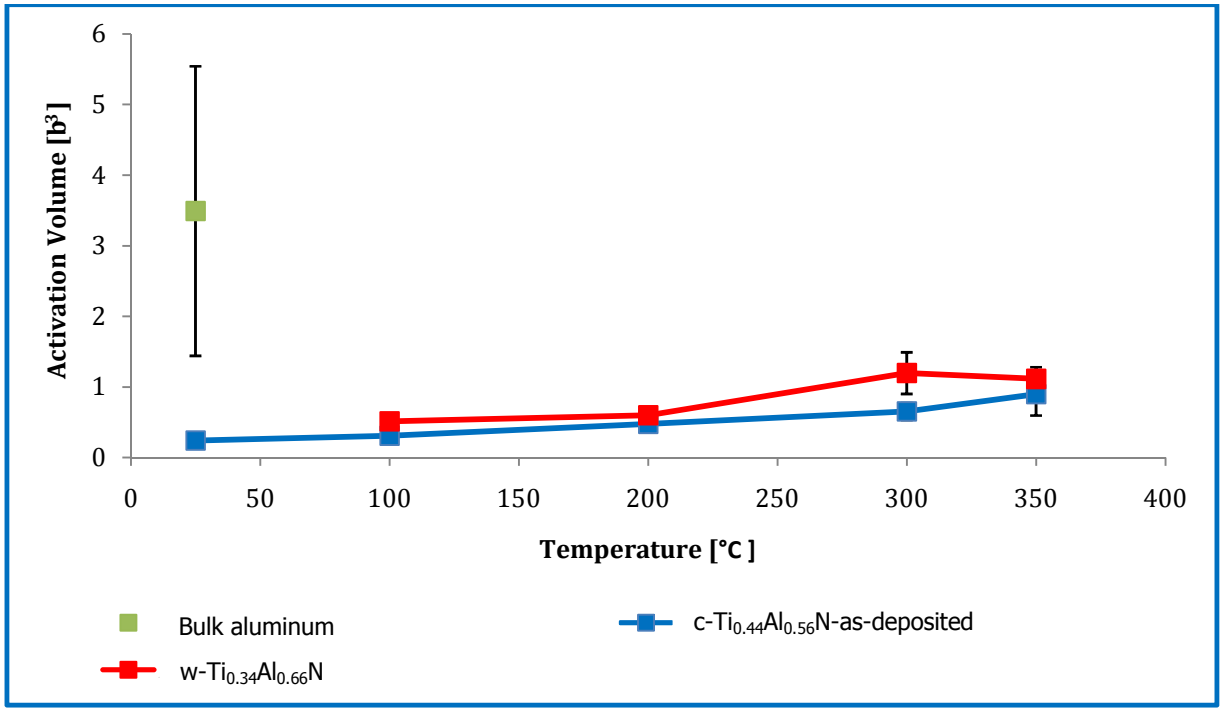

Figure 4-34 : Comparison of the activation volumes for c-$Ti_{0.44}Al_{0.56}N$-as-deposited, w-$Ti_{0.36}Al_{0.64}N$ and aluminum.

The next conclusion, which can be made, from this investigative method, as seen in Fig. 4-34, is that activation volumes determined by nanoindentation, using the last point of the load-displacement curve, tend to be relatively low, when compared with other investigative methods. An activation volume of 1.5-5.5 b^3 for aluminium is equivalent to an activation volume range of 0-25 b^3 determined using a PDF. Therefore the terminology apparent activation volume should be used, when the last point of the load displacement curve is used for calculation, as it would not make any physical sense, to ascertain, that an activation volume smaller than 1, is characteristic for dislocation-dislocation interaction.

Summing up, it can be said, that the cubic-TiAlN films, irrespective of their chemical composition, have very low apparent activation volumes in the range of 0.2 to 0.7b^3. The wurtzite films, on the other hand have an apparent activation volume, which are 2 to 3 times higher than that of the cubic-TiAlN films. Further on, the activation volumes show a trend of rising with rising temperature.

4.2.3.6 Ab-initio calculations of thermal expansion increase

The next graph in Fig. 4-35 represents the lattice parameter as a function of temperature, as calculated by means of Density Function Theory using the VASP package [34]. For each system, two curves corresponding to local density approximation (LDA, lower curve) and generalized gradient approximation (GGA, upper curve), which are known to underestimate and overestimate lattice parameters, respectively, were calculated. Therefore, the actual lattice parameter is expected to lye within the LDA and GGA boundaries. The effects of temperature are taken into account using the quasi-harmonic harmonic approximation [35].

For approximation of the lattice parameter of TiAlN coatings, the interpolation of the lattice parameters of TiN and AlN can be used and were herein calculated [36].

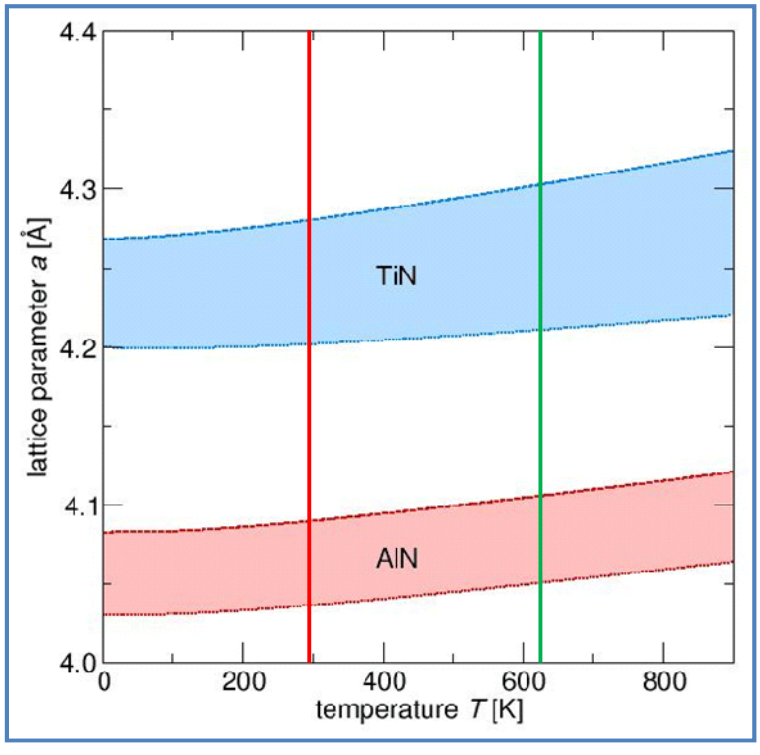

Figure 4-35: Lattice parameter calculation using VASP package, LDA and GGA curves.

Table 4-6 shows the calculation of lattice parameters for 25°C (red line) and 350°C (green line).

	Lattice parameter 25°C	**Lattice parameter 350°C**
TiN		
GGA-approximation	4.28	4.31
LDA-approximation	4.2	4.22
Average	4.24	4.265
AlN		
GGA-approximation	4.09	4.11
LDA-approximation	4.03	4.05
Average	4.06	4.08
TiAlN		
Average	4.15	4.1725
Volume-TiAlN: a^3	71.47	72.64%
Volume %-increase	--	**1.63%**

Table 4-6: Calculation of lattice parameter increase in the temperature range.

Table 4-6 shows that the activation volume increases by 1.63% due to the thermal expansion between 25° and 350°C.

The activation volumes of the samples increase by more than a 100% in the measured temperature range. Only an infinitesimal increase of the activation volume is due to thermal expansion.

4.2.4 Activation energies

All activation energies are calculated in eV for facilitating comparison with other studies. As presented in Chapter 2.7, the total activation energy ΔG_{tot} is dependant on two factors: an athermal component ΔW, which is related to the stress through indentation and a thermal component $\Delta G(\tau)$ [22]:

$$\Delta G_{tot} = \Delta G(\tau) + \Delta W \qquad (4\text{-}2)$$

4.2.4.1 Influence of thermal component $\Delta G(\tau)$:

Figure 4-36 illustrates the influence of temperature on the thermal component $\Delta G(\tau)$ of the total activation energy for all samples:

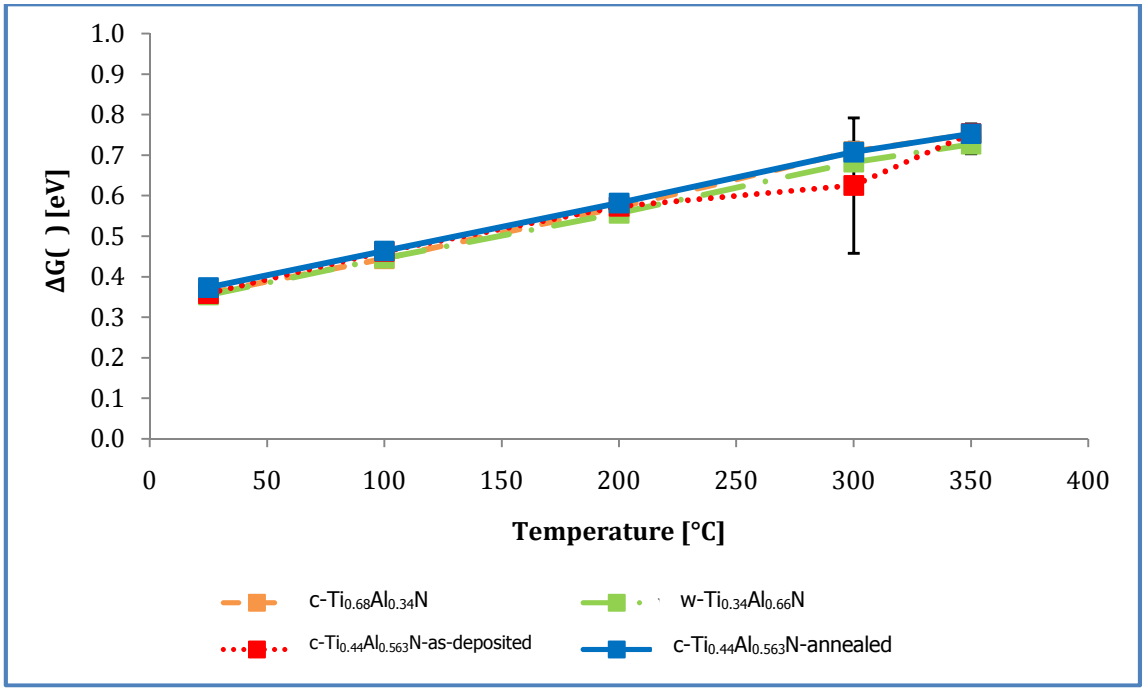

Figure 4-36: The thermal part of the activation energy, $\Delta G(\tau)$, in dependence of the temperature is plotted for all samples, at a loading rate of 0.5 mN/s.

Figure 4-36 shows that for all samples the thermal part of the energy $\Delta G(\tau)$ rises linearly with increasing temperature. In the case of the cubic and the wurtzite TiAlN samples, the total activation energy approximately doubles in the range of 25 to 350°C. While for hardness, Young's modulus and activation volume, different crystallographic structures presented a noticeable difference in the determined values, the thermal part of the activation energy is similar for the cubic and the wurtzite samples.

4.2.4.2 Influence of mechanical component ΔW :

Figure 4-37 shows the influence of the mechanical component ΔW of the total activation energy in the tested temperature range:

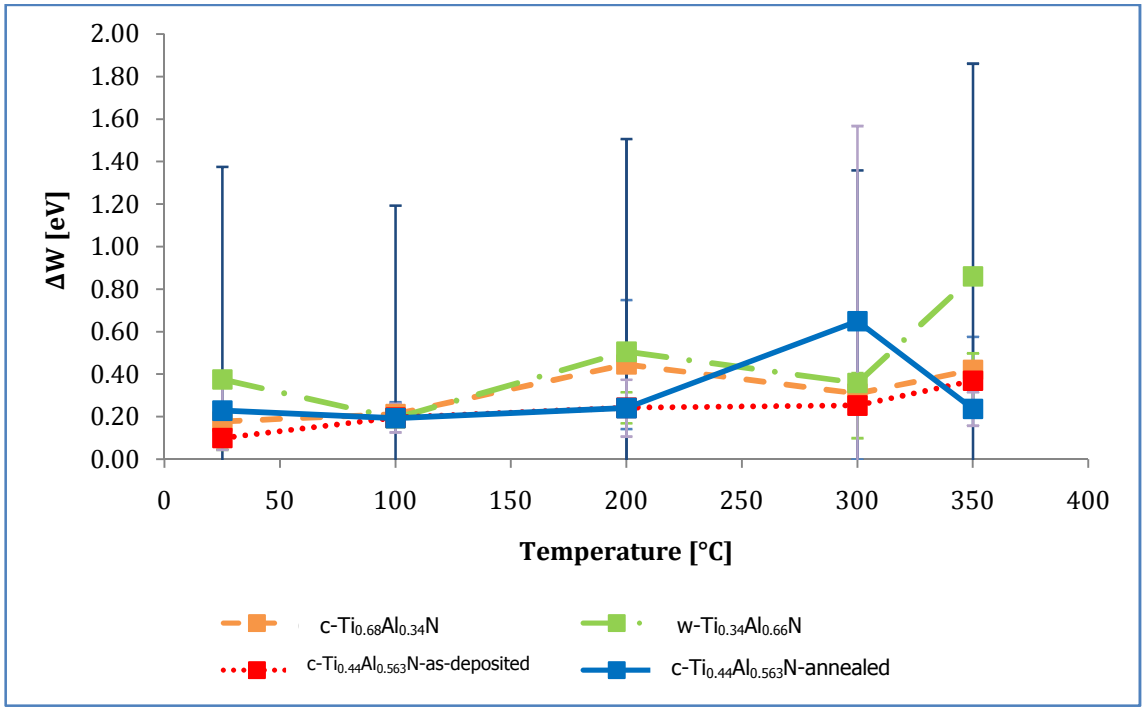

Figure 4-37: The mechanical part of the activation energy, ΔW, in dependence of the temperature, at a loading rate of 0.5 mN/s.

The mechanical part of the activation energy has slightly higher values for the wurtzite structure than the cubic structure. For both structures, ΔW, once again,

doubles in the tested temperature range. ΔW ranges between 0.19-0.65 eV for the cubic structures and between 0.19-0.86 eV for the wurtzite structure. The error bars for the measured values are very large. This results from the fact, that the measured values for τ have large fluctuations. Even though the mechanical part should be athermal, at higher temperatures, higher dislocation activities take place, as seen in chapter 4.2.1, where the activation volume doubles in the tested temperature range. Therefore, the mechanical part of the activation energy is also related to temperature and cannot be regarded as totally "athermal".

4.2.4.3 Influence of total activation energy $\Delta G_{(tot)}$:

The following Figure 4-38 presents a graph of the total activation energy ΔG_{tot} as a function of temperature:

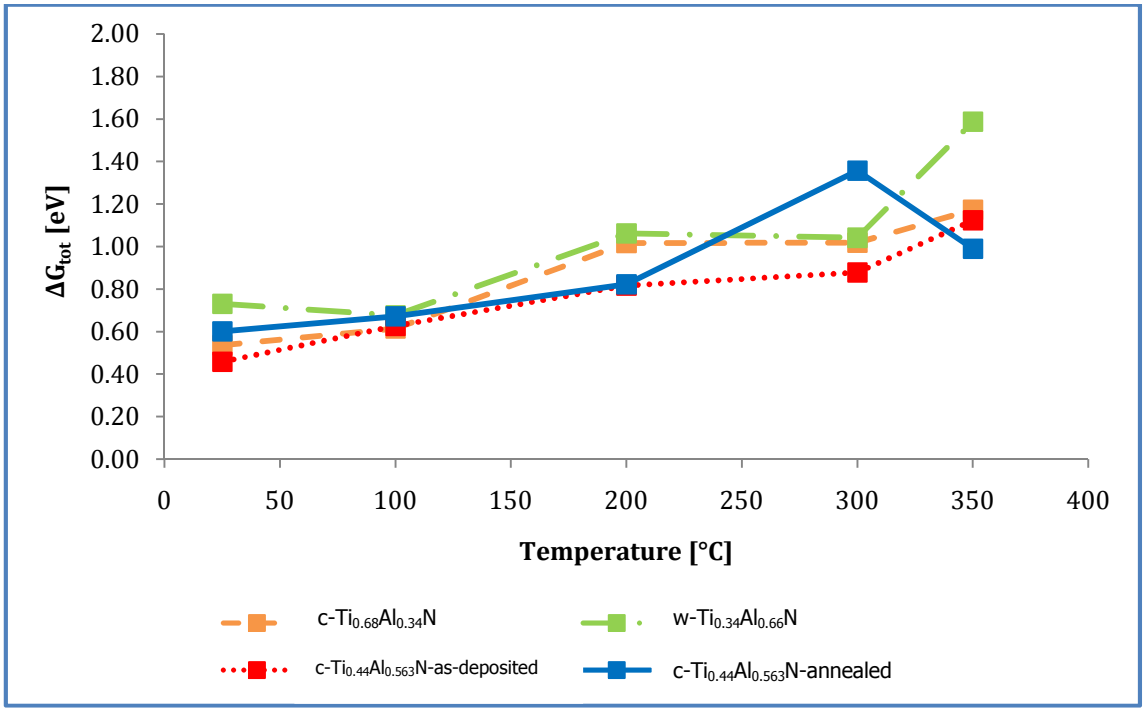

Figure 4-38: ΔG_{tot} in dependence of the temperature is for all samples, at a loading rate of 0.5 mN/s.

As an increase of the thermal and athermal part in the tested temperature range was observed, the addition of both term, will show the same trend. Further on, once again, all deposited samples, show comparable values of ΔG_{tot}. All values range between 0.45-1.65 eV. When the values of the activation energies for the samples are converted from eV units to μb^3, the total activation energy values are found to be in the range of $1.29.10^{-2} - 3.88.10^{-2}$ μb^3.

Activation energies are inherently linked to the rate-controlling mechanism. If a rate controlling mechanism changes, so will the measured activation energy range, this is illustrated in Table 4-7.

Obstacle	**ΔG_0 [μb^3]**	**ΔG_0 [eV]**	**Example**
Strong	2 μb^3	70 eV	Large or strong precipitates
Medium	0.2-1 μb^3	7-35 eV	Forest dislocations, small or weak precipitates
Weak	< 0.2 μb^3	< 7 eV	Lattice resistance, solution hardening

Table 4-7: Classification of obstacles according to their strength in terms of ΔG_{tot}[23].

Even though the activation energies double in the tested temperature range, they are nowhere near the value of 0.2, thus excluding dislocation-interactions as rate controlling mechanism in the investigated temperature range.

When compared to the values in the Table 4-7, the rate-controlling deformation mechanism for all measured TiAlN samples in the tested temperature range of 25-350°C, independently of crystallographic structure and chemical composition, can be chosen to be lattice resistance or movement of point defects. This is plausible, as TiAlN ceramic films are stiff in nature. It would be expected that dislocation activity is very limited at such low temperatures as the tested temperature range chosen for this investigation.

4.2.4.4 The loading rate dependence of ΔG_{tot}:

Figure 4-35 presents the influence of the loading rate on the calculated total activation energy values:

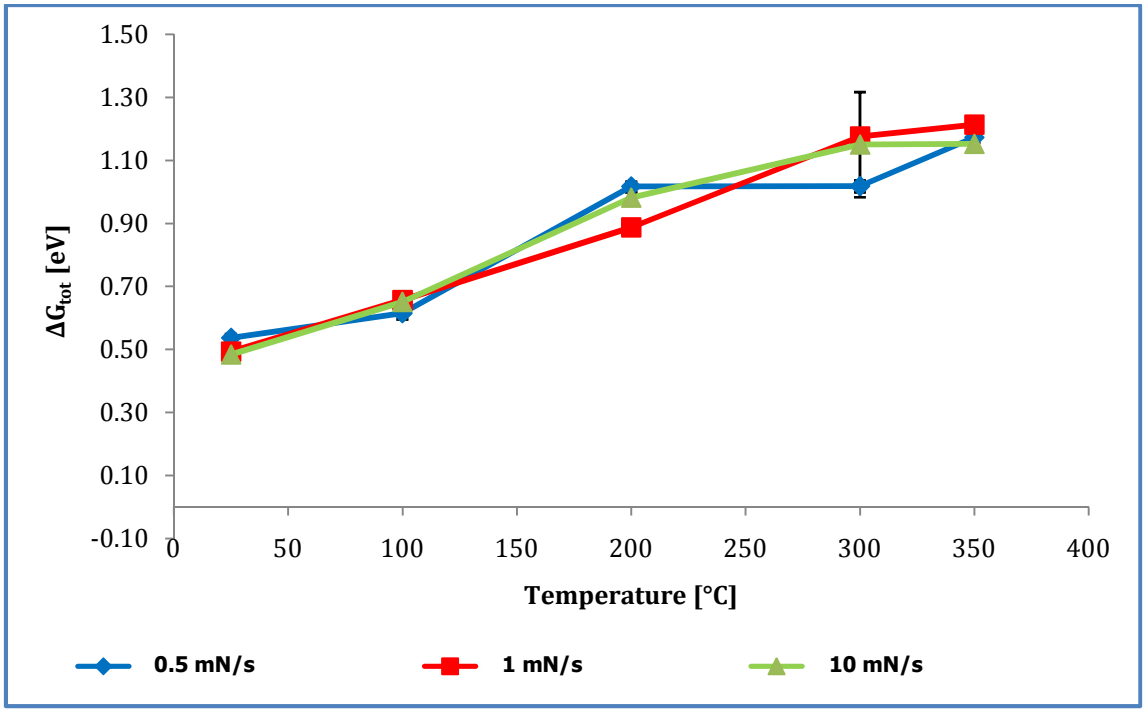

Figure 4-39: Loading rate dependence of ΔG_{tot} for c-$Ti_{0.68}Al_{0.32}N$ as a function of the temperature.

Figure 4-39 illustrates, that the activation energy is not loading rate dependant. As the hardness and the activation volumes were slightly loading rate dependant, we would expect the mechanical part of the activation energy to also present a slight loading-rate dependence. Yet, as the thermal part, which is responsible for about 50% of the energy, is not loading rate dependant, the total energy turns out not to be measurably loading-rate dependant.

Independently of the actual rate-controlling mechanism, the following can be said: The activation energy for the movement of a dislocation rises proportionally to the temperature. Meaning that the thermal component plays an important role in the rate-controlling mechanism. Our measurements have shown, that also the mechanical part of the activation energy majorly influences the rise in ΔG_{tot}.

5 Summary and conclusions

In this thesis, the mechanical properties and the fundamental deformation parameters of reactively magnetron sputtered TiAlN coatings have been investigated using high-temperature nanoindentation. The effects of the chemical composition, as well as of the structure were analysed.

Out of absence of adequate apparatus or out of convenience, the mechanical properties of hard ceramic coatings are determined from room temperature tests or after annealing. As TiAlN coatings are used primarily for high temperature applications, it is more sensible to determine the mechanical characteristics at higher temperatures. Nevertheless only few studies have investigated the behaviour of TiAlN at high temperatures. Detailed literature research showed that only the hot hardness of TiAlN was measured in previous investigations, but no detailed information has been reported on fundamental deformation parameters.

For this investigation near-to epitaxial TiAlN films were grown on MgO single crystals (100) using a reactive magnetron sputtering system. The chemical composition was varied by physically adding Ti pieces onto the $Ti_{0.5}Al_{0.5}$ target. A multitude of pre-deposition runs were necessary to deposit three single-phased films with the following chemical compositions: cubic-$Ti_{0.44}Al_{0.56}N$, cubic-$Ti_{0.68}Al_{0.32}N$ and wurtzite-$Ti_{0.36}Al_{0.64}N$. Additionally cubic-$Ti_{0.44}Al_{0.56}N$ was also annealed under an argon atmosphere at 600°C for 24 hours.

HT-nanoindentation experiments were carried out in a temperature range from 25 - 350°C at 3 different loading rates of 0.5, 1 and 10 mN/s using a Berkovich indenter. Even though the NanoTest platform can test up to 750°C, this temperature was not chosen, because diamond tips are known to readily oxidize at ~400°C.

First the hardness behaviour was investigated: A decrease of the hardness with rising temperature was observed for the single-phased wurtzite-$Ti_{0.36}Al_{0.64}N$ sample. The hardness fell by 14.5% from 20.0 to 17.1 GPa between 25 - 350°C. For the cubic

samples, the hardness remained relatively constant at around ~22 GPa only decreasing slightly to 19.9 GPa at around 350°C. The annealed cubic-$Ti_{0.44}Al_{0.56}N$ samples showed higher hardness values, than in the as-deposited state. XRD analysis on powder samples of cubic-$Ti_{0.44}Al_{0.56}N$ before and after annealing indicated an increase of the integral width from 0.55 to 0.59 suggesting ongoing spinodal decomposition to form Ti- and Al-rich cubic domains, when annealed at low temperatures of 600°C for 24 hours.

In the loading rate range of 0.5 to 10 mN/s the hardness of all TiAlN films was found to be loading-rate sensitive. The hardness of c-$Ti_{0.44}Al_{0.56}N$-annealed increased by 17.2% from 26.1 to 30.6 GPa, $Ti_{0.44}Al_{0.56}N$-as-deposited increased by 24.8% from 20.1 to 25.1 and $Ti_{0.68}Al_{0.32}N$ increased by 24.0% from 21.2 to 26.3 GPa. The loading-rate sensitivity of the wurtzite sample could not be measured because of the influence of substrate effects. Further on the $Ti_{0.44}Al_{0.56}N$-annealed sample presented lower V* values than the as-deposited state. The annealed sample only showed a 34% increase of activation volume at a loading rate of 0.5 mN/s compared to 236% for the as-deposited state.

Secondly the Young's modulus values were investigated. The Young's modulus values for all samples remained constant throughout the temperature range: 344 ± 34 GPa for c-$Ti_{0.68}Al_{0.32}N$, 336 ± 23 GPa for c-$Ti_{0.44}Al_{0.56}N$-as-deposited, 356 ± 21 GPa for c-$Ti_{0.44}Al_{0.56}N$-annealed and 219 ± 11 GPa for the wurtzite-$Ti_{0.36}Al_{0.64}N$.

Thirdly fundamental deformation parameters were calculated and extracted. Dislocation activation volume values in the range of 0.18 to 0.79 b^3 were calculated for the cubic samples. The activation volume values for the wurtzite sample ranged from 0.24 to 1.22 b^3. Ab-initio calculations using the VASP package showed that 1.63% rise of V^* in the tested temperature range is due to thermal expansion. For further comparison purposes, V^* values were determined for bulk-aluminum at room temperature using a population density function (PDF). V^* values ranged between

0-4 b^3 for the cubic films and 0-25 b^3 for bulk-aluminum, which is a clear indication for a different deformation mechanism than present in ceramic films.

The total activation energies for all samples independently of crystallographic orientation, or chemical compositions, were similar and ranged between 0.19-0.86 eV or in other units $1.29.10^{-2} – 3.88.10^{-2}$ μb^3. The total activation energies rose linearly with the temperate, whereby both the thermal and the mechanical work equally influenced the calculated values.

For a particular crystallographic structure, independently of the chemical composition, the calculated high temperature hardness, Young's moduli, activation volumes and energies were found to be very similar.

There are furthermore two main factors, which could account for the rise in activation volumes and fall of hardness in the tested temperature range:

- **The lattice resistance**: The lattice resistance could be falling with rising temperature, meaning that the material becomes weaker, which would allow for the accommodation of more dislocation movement. As the Young's modulus values remained constant in the tested temperature range, the lattice resistance should similarly stay constant.
- **The thermal activation energy**: Similarly to the apparent activation volume, the thermal activation energy $\Delta G(\tau)$, has been found to be rise linearly with the temperature.

Therefore the following conclusion will be drawn from this investigation:

The proposed deformation mechanism for the wurtzite and cubic samples is lattice resistance or particle-particle interactions.

For the cubic structure, lattice resistance can with good conscience be chosen as the rate-controlling mechanism, as the activation volumes, which are smaller than one for all temperatures and the low activation energy both agree with each other.

For the wurtzite structure, the combination of activation volumes and activation energies calculations is not conclusive. Looking at the low activation energies for the wurtzite sample, the rate controlling mechanism would have to also be lattice resistance. Clearly the activation volumes paint a different picture, where the values for higher temperatures are in the range of a volume of a burgers vector. A volume of a burgers vector in turn means that a dislocation would have to overcome an obstacle as big as a dislocation, speaking for a dislocation-dislocation interaction.

Even though the apparent activation volumes for the wurtzite structure, of 0.24, at room temperature, shift to higher values of 1.22 at 350°C, the apparent obstacles encountered by the dislocation are of a very small size, when compared to these encountered in a material, where dislocation-dislocation interaction is the primary deformation mechanism: bulk aluminium.

The lattice resistance is expected to be constant over the temperature range, as another inherent material property remains constant: the Young's Modulus.

This thesis proves that nanoindentation can be successfully used to extract fundamental deformation parameters. It is not only possible to extract and calculate the fundamental deformation parameters, such as activation energies and activation volumes, but also to use these findings to conclude which rate-controlling mechanism is taking place for a certain material, at a certain temperature.

6 Future scope

Temperature dependence of the shear modulus:

The temperature of the shear modulus was used for all the calculations (Chapter 4.2.3). After observing, that the Young's Modulus had not fallen with increasing temperature, in the tested range, the usage of the temperature dependence of the shear modulus has to be challenged. The shear modulus is inherently related to the Young's modulus. If no temperature dependence of the Young's modulus was observed, then none of the shear modulus should be expected. For this temperature range, the use of a constant temperature independent value for the shear modulus is therefore proposed for future calculations.

Characterization using TEM

The effectiveness of the combination of the nanoindentation and XRD analysis methods is limited, as both are indirect characterisation techniques. Therefore a TEM analysis of the microstructural evolution of the area under the indent would have to be performed, in order to empirically confirm the results by direct observation. Cross sections of the indents using a focused ion beam, could be imaged using a high resolution TEM. TEM observations would help prove the following points:

Rise in hardness with indentation dept: The rising hardness with increasing indentation depth was explained by the fact, that the films are probably denser at the substrate-film interface and more porous at the top (chapter 4.2.1). Film morphology characterisation, could easily be performed using TEM.

Delamination or cracks: The reason for the actual jumps in the load-displacement curves could also further be explained.

These TEM analyses would help validate the assumptions made in this thesis.

Influence of the diamond area function

Even though a lot of emphasis was put into measuring the diamond area function properly, some open issues still remain:
The hardness of the annealed $Ti_{0.44}Al_{0.56}N$ sample were higher than the as-deposited $Ti_{0.44}Al_{0.56}N$ sample. This was traced back to the influence of the same diamond area function, which was used for both samples. Using a single diamond area function for calculation of many samples, should be avoided, as the tip undergoes blunting in such a severe environment of high temperatures and loading rates. The diamond area function, should in future, be measured after each and every indentation cycle to minimise the influence of a faulty diamond area function on calculated results. Therefore a new test cycle of the annealed and as-deposited sample is recommended, with emphasis on the determination of the diamond area function after each indentation cycle. This new test cycle would prove if spinodal decomposition or the diamond area function is responsible for hardness increase after annealing at 600°C for 24 hours.

Calculation of activation volumes:

The calculation of the activation volumes was done, by choosing the last point on the load-displacement curve. The accuracy of the reliability of the data acquisition at the highest loading point must be questioned. Due to possible machine and electronic errors and fluctuations of mechanical or thermal nature, the activation volumes tend to have very large error bars. To reduce this error, the activation volume, should be calculated from a few points or even from an average of the last 20 points, for example. The usage of a population-density function, as shown in chapter 4.2.3, is a useful alternative for visualisation and calculation of the activation volumes.

Alternative method for determining the activation volumes

A research group around Prof. Luc Van Deperre is currently calculating the activation volumes in a slightly different way, than the one used in this thesis. By plotting the natural logarithm of loading rate versus the temperature, the slope of the curve is equal to kT/V*. The activation volume can therefore be calculated from the slope of the diagram. Isolated activation volume values were calculated with this method and seem to yield activation volumes in the same order of magnitude. A thorough study for the complete set of data would not only confirm the results but would yield more credibility to the investigation method used in this thesis.
Further on, Prof. Van Deperre's method allows for the calculation of another fundamental constant: the Peierls stress. This is done through extrapolation of activation volumes and stresses to zero Kelvin. The calculation of the Peierls stress, would allow for a deeper insight into the deformation characteristics of the investigated films and their temperature dependence.

Temperature testing range

The final point of the future scope is also the one with the most interesting potential. The tested temperature was limited by the fact that the diamond tip oxidizes at ~400°C. The NanoTest system has the capability of testing up to 750°C. By using a tip, which can withstand such high temperatures, such as Boron Nitride or Sapphire for example, a higher temperature testing range will be possible. This will also allow for the possibility for in-situ measurements of phenomena, which are important for TiAlN films, such as spinodal decomposition. Further on many factors increase with rising temperature: activity of dislocations, vacancies, movement of grain boundaries and creep. High temperature nanoindentation presents an unrivaled potential for in-situ investigation of these phenomena.

7 Appendix

Appendix 1: Deposition conditions for magnetron sputtering system.

Appendix 2: Diamond area functions.

Appendix 3: H, E, V* and ΔG_{tot} at a loading rate of 0.5 mN/s.

Appendix 4: H, E, V* and ΔG_{tot} at a loading rate of 1 mN/s.

Appendix 5: H, E, V* and ΔG_{tot} at a loading rate of 10 mN/s.

Appendix 6: XRD scan settings

Appendix 7: Burgers vector determination for fcc and hcp crystals.

7.1 Appendix 1: Deposition conditions for magnetron sputtering system

Sample Name	Sample Number	Structure	Um [V]	Im [A]	Pm [W]	Icoil [A]	T [°C]	Ar-flow [sccm]	N-flow [sccm]	Ptot [mbar]	Cleaning time [min]	T [°C]
c-Ti0.56Al0.44N-as-deposited	Run 28-3	cubic	345.6	1.49	518	-2	499	16	0	$4.8.10^{-3}$	5	500
c-Ti0.56Al0.44N-annealed	Run 28-3	cubic	345.6	1.49	518	-2	499	16	0	$4.8.10^{-3}$	5	500
c-Ti0.68Al0.32N	Run 34-011	wurtzite	340.6	1.49	510	-2	500	16	0	$5.0.10^{-3}$	5	500
c-Ti0.36Al0.64N	Run 37-012	cubic	335	1.49	530	-2	500	16	0	$4.99.10^{-3}$	5	500

Sample Name	Sample Number	Structure	Um [V]	Im [A]	Pm [W]	Icoil [A]	T [°C]	Ar-flow [sccm]	N-flow [sccm]	Ptot [mbar]	Deposition time [min]	Us [V]	Is [mA]
c-Ti0.56Al0.44N-as-deposited	Run 28-3	cubic	319	1.49	478	-2	500	13	1.6	$4.50.10^{-3}$	224	60	0.194
c-Ti0.56Al0.44N-annealed	Run 28-3	cubic	319	1.49	478	-2	500	13	1.6	$4.50.10^{-3}$	224	60	0.194
c-Ti0.68Al0.32N	Run 34-011	wurtzite	334.3	1.49	502	-2	500	7	10	$4.91.10^{-3}$	176	60	0.172
c-Ti0.36Al0.64N	Run 37-012	cubic	337	1.49	493	-2	500	13	1.6	$4.64.10^{-3}$	178	60	0.194

Table 7-1: Deposition conditions for analyzed samples using a reactive magnetron sputtering system

7.2 Appendix 2: Diamond area functions

This appendix lists the diamond area function that were determined during the course of the indentation of the samples used in this thesis.

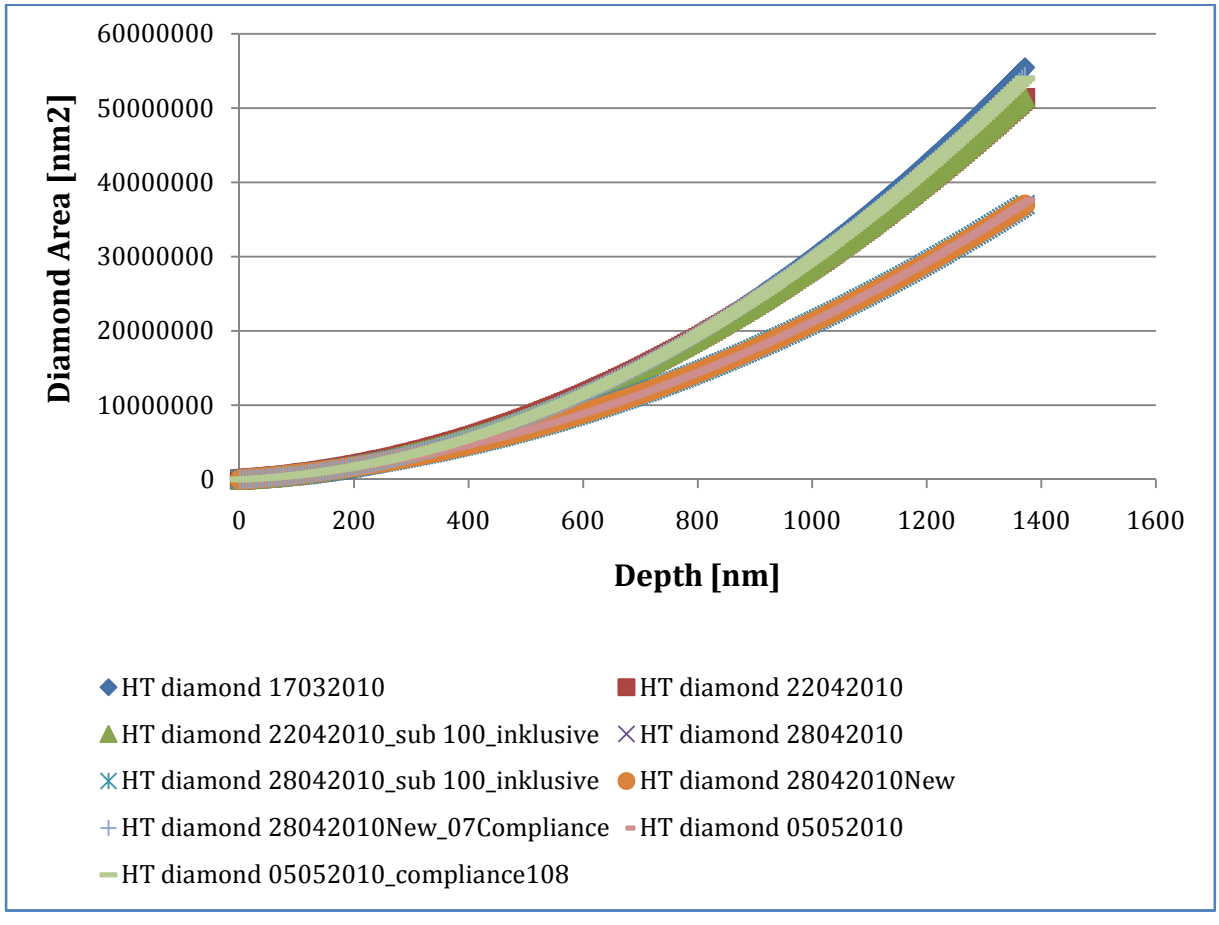

Figure 7-1: All the diamond area functions measured during sample testing.

Looking at Fig. 0-1, the first observation that can be made is that the following diamond area functions cannot be used to further calculations as they are "off":

- HT diamond 28.04.2010
- HT diamond 28.042010New
- HT diamond 28042010_sub100_inklusive
- HT diamond 05052010

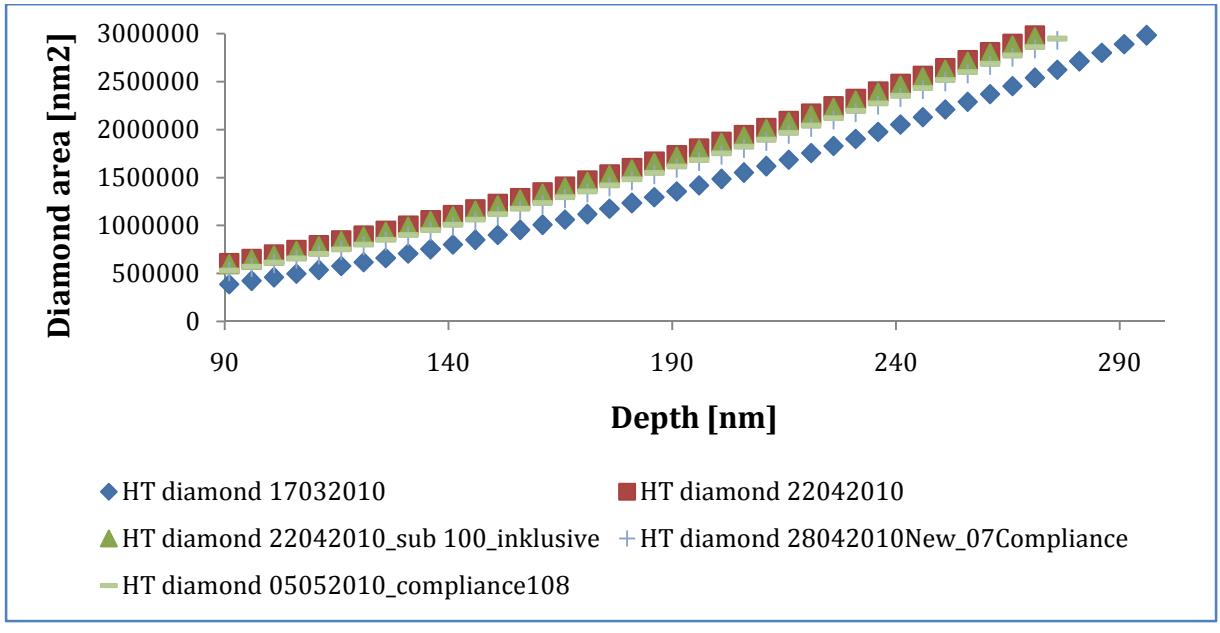

Figure 7-2: selected diamond area functions.

Looking at Fig. 0-2 the further observation that can be made, is that for the analysis depth used in this thesis ~100 nm - ~350 nm, all Diamond area functions can be used in chronological order apart from HT diamond 13032010. The diamond area functions used for the samples are presented in the following Table 0-1:

Sample	DAF NAME	DAF factor a	DAF factor b
c-$Ti_{0.44}Al_{0.56}N$	HT diamond 22042010_sub 100_inklusive	438,941,169	24,147,733
c-$Ti_{0.68}Al_{0.32}N$	HT diamond 22042010_sub 100_inklusive	438,941,169	24,147,733
c-$Ti_{0.44}Al_{0.56}N$-600C-24h	HT diamond 22042010_sub 100_inklusive	438,941,169	24,147,733
w-$Ti_{0.36}Al_{0.64}N$	HT diamond 28042010New_07_Compliance	331,414,397	26,435,754

Table 0-1: Diamond area function used to calculate the tips.

7.3 Appendix 3: H, E, V* and Δ G_{tot} at a loading rate of 0.5 mN/s.

Hardness values at a loading rate of 0.5 mN/s

	c-Ti0.68Al0.34N		w-Ti0.34Al0.66N		c-Ti0.44Al0.56N_as_dep.		c-Ti0.44Al0.56N_ann.	
	H [Gpa]	±	H [Gpa]	±	H [Gpa]	±	H [Gpa]	±
25 °C	21,2	1,9	19,8	0,9	20,1	2,3	26,1	1,9
100 °C	18,6	4	19,8	0,8	22,5	1,4	25,5	2,5
200 °C	19,8	1,3	18	1,2	20,1	1,6	22,6	1,3
300 °C	21,7	2,7	18,9	1,3	20,7	2,2	22,4	2,7
350 °C	18,4	1	16,9	1,4	19,9	1,5	19,9	2,8

Young's modulus values at a loading rate of 0.5 mN/s

	c-Ti0.68Al0.34N		w-Ti0.34Al0.66N		c-Ti0.44Al0.56N_as_dep.		c-Ti0.44Al0.56N_ann.	
	E [Gpa]	±	E [Gpa]	±	E [Gpa]	±	E [Gpa]	±
25 °C	345,3	19,6	211,8	10,5	329,2	25,7	369	18
100 °C	321	63,9	231	5,7	351	10,6	383,8	17,4
200 °C	357,1	20	225,6	10,6	332,7	34,5	344,4	29,5
300 °C	352,7	39,3	214,6	16,2	351	29,3	353,7	23,5
350 °C	344,5	27,3	213	14	320,6	19,9	329,2	18,5

Activation volume values at a loading rate of 0.5 mN/s

	c-Ti0.68Al0.34N		w-Ti0.34Al0.66N		c-Ti0.44Al0.56N_as_dep.		c-Ti0.44Al0.56N_ann.	
	V* [b^3]	±	V* [b^3]	±	V* [b^3]	±	V* [b^3]	±
25 °C	0,25	0,06	0,45	0,84	0,17	0,10	0,27	0,22
100 °C	0,27	0,12	0,28	0,07	0,23	0,09	0,25	0,14
200 °C	0,69	0,48	0,68	0,45	0,37	0,11	0,33	0,19
300 °C	0,43	0,19	0,49	0,09	0,38	0,24	0,83	1,16
350 °C	0,69	0,25	1,22	1,25	0,58	0,21	0,37	0,12

Total activation energy values at a loading rate of 0.5 mN/s

	c-Ti0.68Al0.34N		w-Ti0.34Al0.66N		c-Ti0.44Al0.56N_as_dep.		c-Ti0.44Al0.56N_ann.	
	Δ G_{tot} [eV]	±	Δ G_{tot} [eV]	±	Δ G_{tot} [eV]	±	Δ G_{tot} [eV]	±
25 °C	0,54	0,04	0,73	0,73	0,46	0,07	0,60	0,19
100 °C	0,62	0,08	0,68	0,12	0,63	0,04	0,67	0,08
200 °C	1,02	0,32	1,06	0,37	0,82	0,09	0,82	0,14
300 °C	1,02	0,33	1,04	0,09	0,88	0,32	1,36	0,94
350 °C	1,17	0,17	1,59	0,91	1,12	0,15	0,99	0,10

Table 7-2: calculated H, E, V* and Δ G_{tot} for 0.5mN/s.

7.4 Appendix 4: H, E, V* and Δ G_{tot} at a loading rate of 1 mN/S.

Hardness values at a loading rate of 1 mN/s

	c-Ti0.68Al0.34N		w-Ti0.34Al0.66N		c-Ti0.44Al0.56N_as_dep.		c-Ti0.44Al0.56N_ann.	
	H [Gpa]	±	H [Gpa]	±	H [Gpa]	±	H [Gpa]	±
25 °C	23,5	2,0	20,0	0,7	21,5	2,3	28,0	1,5
100 °C	22,2	2,0	19,7	0,1	21,8	2,4	26,9	1,5
200 °C	24,0	1,9	19,0	2,0	20,5	2,2	23,8	1,4
300 °C	21,9	1,9	18,2	1,0	21,7	4,3	23,5	1,1
350 °C	18,6	2,0	17,2	1,0	21,8	1,0	24,9	1,7

Young's modulus values at a loading rate of 1 mN/s

	c-Ti0.68Al0.34N		w-Ti0.34Al0.66N		c-Ti0.44Al0.56N_as_dep.		c-Ti0.44Al0.56N_ann.	
	E [Gpa]	±	E [Gpa]	±	E [Gpa]	±	E [Gpa]	±
25 °C	369,6	20,9	218,5	8,1	358,5	28,7	398,3	9,3
100 °C	363,5	17,1	225,2	7,0	359,5	28,2	381,2	9,4
200 °C	369,5	22,1	228,5	7,9	351,3	29,5	356,5	22,6
300 °C	365,2	22,4	228,3	8,3	359,3	24,3	369,8	18,8
350 °C	345,0	34,7	217,7	11,2	333,9	31,6	353,9	20,1

Activation volume values at a loading rate of 1 mN/s

	c-Ti0.68Al0.34N		w-Ti0.34Al0.66N		c-Ti0.44Al0.56N_as_dep.		c-Ti0.44Al0.56N_ann.	
	V* [b^3]	±	V* [b^3]	±	V* [b^3]	±	V* [b^3]	±
25 °C	0,17	0,06	0,24	0,11	0,22	0,04	0,18	0,03
100 °C	0,29	0,08	0,24	0,14	0,28	0,02	0,22	0,07
200 °C	0,40	0,06	0,52	0,16	0,32	0,11	0,32	0,10
300 °C	0,68	0,24	0,64	0,32	0,42	0,23	0,47	0,13
350 °C	0,79	0,37	0,67	0,19	0,53	0,17	0,43	0,15

Total activation energy values at a loading rate of 1 mN/s

	c-Ti0.68Al0.34N		w-Ti0.34Al0.66N		c-Ti0.44Al0.56N_as_dep.		c-Ti0.44Al0.56N_ann.	
	Δ G_{tot} [eV]	±	Δ G_{tot} [eV]	±	Δ G_{tot} [eV]	±	Δ G_{tot} [eV]	±
25 °C	0,49	0,06	0,55	0,10	0,50	0,04	0,53	0,04
100 °C	0,66	0,07	0,61	0,12	0,64	0,05	0,65	0,08
200 °C	0,89	0,07	0,95	0,10	0,77	0,10	0,82	0,10
300 °C	1,18	0,17	1,14	0,27	0,90	0,28	1,05	0,12
350 °C	1,21	0,26	1,19	0,15	1,02	0,35	1,11	0,15

Table 7-3: calculated H, E, V* and Δ G_{tot} for 1mN/s.

7.5 Appendix 5: H, E, V* and Δ G_{tot} at a loading rate of 10 mN/S.

Hardness values at a loading rate of 10 mN/s

	c-Ti0.68Al0.34N		w-Ti0.34Al0.66N		c-Ti0.44Al0.56N_as_dep.		c-Ti0.44Al0.56N_ann.	
	H [Gpa]	±	H [Gpa]	±	H [Gpa]	±	H [Gpa]	±
25 °C	26,3	0,8	19,6	1,9	25,2	2,5	30,6	1,1
100 °C	23,9	0,9	19,8	1,5	25,6	1,5	28,5	1,0
200 °C	25,3	0,6	17,0	2,0	24,0	1,2	27,0	0,3
300 °C	22,6	1,3	15,7	3,4	23,8	1,8	25,2	0,6
350 °C	19,8	1,6	14,1	3,1	23,6	1,0	24,2	0,5

Young's modulus values at a loading rate of 10 mN/s

	c-Ti0.68Al0.34N		w-Ti0.34Al0.66N		c-Ti0.44Al0.56N_as_dep.		c-Ti0.44Al0.56N_ann.	
	E [Gpa]	±	E [Gpa]	±	E [Gpa]	±	E [Gpa]	±
25 °C	408,7	19,5	211,2	15,3	396,3	27,8	29,4	1,1
100 °C	377,0	15,6	237,8	14,4	414,1	8,8	27,2	1,1
200 °C	389,4	13,8	233,6	16,6	395,6	15,9	25,7	0,5
300 °C	365,6	15,9	221,6	12,9	369,6	18,4	24,0	0,8
350 °C	342,2	14,5	217,7	10,3	369,7	18,6	23,1	0,6

Activation volume values at a loading rate of 10 mN/s

	c-Ti0.68Al0.34N		w-Ti0.34Al0.66N		c-Ti0.44Al0.56N_as_dep.		c-Ti0.44Al0.56N_ann.	
	V* [b^3]	±	V* [b^3]	±	V* [b^3]	±	V* [b^3]	±
25 °C	0,19	0,01	0,27	0,07	0,18	0,01	0,17	0,01
100 °C	0,31	0,04	0,32	0,09	0,32	0,03	0,22	0,03
200 °C	0,56	0,31	4,90	10,30	0,34	0,03	0,33	0,05
300 °C	0,73	0,28	3,18	4,60	0,49	0,08	0,51	0,06
350 °C	0,78	0,22	-	-	0,48	0,02	0,67	0,13

Total activation energy values at a loading rate of 10 mN/s

	c-Ti0.68Al0.34N		w-Ti0.34Al0.66N		c-Ti0.44Al0.56N_as_dep.		c-Ti0.44Al0.56N_ann.	
	Δ G_{tot} [eV]	±	Δ G_{tot} [eV]	±	Δ G_{tot} [eV]	±	Δ G_{tot} [eV]	±
25 °C	0,48	0,03	0,52	0,05	0,47	0,03	0,50	0,02
100 °C	0,65	0,05	0,64	0,07	0,70	0,02	0,61	0,05
200 °C	0,98	0,26	3,46	6,13	0,77	0,05	0,81	0,06
300 °C	1,15	0,20	2,33	2,38	0,94	0,25	1,05	0,05
350 °C	1,15	0,15	50,14	117,85	1,02	0,25	1,21	0,13

Table 7-4: calculated H, E, V* and Δ G_{tot} for 1 mN/s.

7.6 Appendix 6: XRD scan settings

The following scan settings were used on the XRD machine in London to measure the films:

Start angle : 30°
End angle : 120°
Time per step : 50 s
Step size: 0.0034°
Number of points : 2693

7.7 Appendix 7: Burgers vector determination for fcc and hcp crystals

Burgers vectors for face centered cubic crystals:

The burgers vector for face centered cubic crystals can be calculated as follows: the magnitude of the smallest possible burgers vector is in the close packed direction <110>. The vector length would be ½ <110>, as can be seen in the following Figure 0-3 and 0-4.

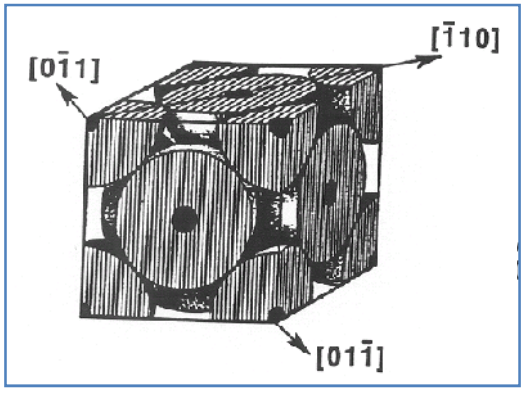

Figure 7-3: Slip systems in fcc crystals, with 3 close packed directions in each <-110> [37].

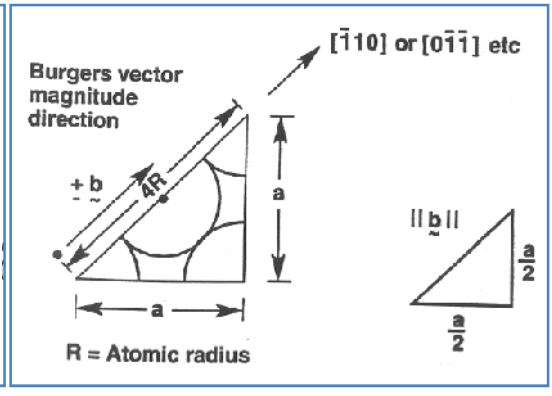

Figure 7-4: Calculation of b in fcc crystals in terms of lattice parameter a [37].

The burgers vector for the fcc systems therefore has a length of $b = \frac{a\cdot\sqrt{2}}{2}$.

As the burgers vector changes with the chemical composition, the following burgers vectors, calculated using Vegard's law and confirmed with ab-initio calculations were used for the analyzed samples:

Sample	burgers vector [m]
c- $Ti_{0.44}Al_{0.56}N$ -as-deposited	$2{,}96.10^{-10}$ [10, 38]
c-$Ti_{0.44}Al_{0.56}N$-annealed	$2{,}96.10^{-10}$ [10, 38]
c-$Ti_{0.68}Al_{0.32}N$	$2{,}98.10^{-10}$ [10, 38]

Table 7-5: Burgers vectors used for the cubic samples.

Burgers vectors for hexagonal close packed crystals:

A variety of slip systems have been observed for hexagonal close packed (hcp) crystals. Yet predominant slip directions are <11-20> and <0001>.

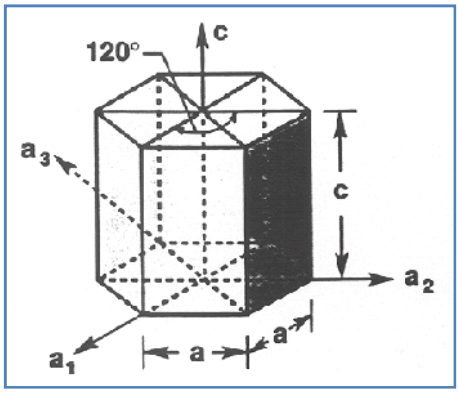

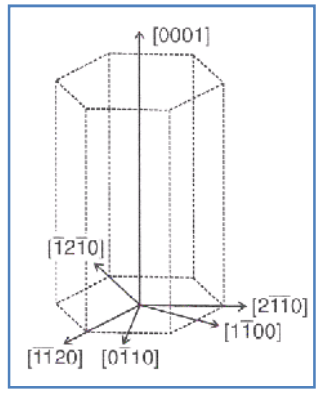

Figure 7-5: Slip systems in hcp. The 3 close packed directions are <11-20> [37].

Figure 7-6: Crystallographic directions in hcp system [39].

The predominant burgers vector direction for a vast number of hcp systems is <11-20>. The calculation of the burgers vector will therefore be $b = \frac{a.}{3} < 1120 >$, which itself is equal to a.

Sample	burgers vector [m]
w-$Ti_{0.36}Al_{0.64}N$	$3{,}22.10^{-10}$ [10, 38]

Table 7-6: Burgers vectors used for the wurtzite sample.

8 References

1. Jindal, P.C., et al., *Performance of PVD TiN, TiCN, and TiAlN coated cemented carbide tools in turning.* International Journal of Refractory Metals and Hard Materials, 1999. 17(1-3): p. 163-170.
2. Yamamoto, R., S. Murakami, and K. Maruyama, *High-temperature mechanical properties of hot-pressed TiN with fine grain size.* Journal of Materials Science, 1998. 33(8): p. 2047-2052.
3. PalDey, S. and S.C. Deevi, *Single layer and multilayer wear resistant coatings of (Ti,Al)N: a review.* Materials Science and Engineering A, 2003. 342(1-2): p. 58-79.
4. Brogren, M., et al., *Titanium-aluminum-nitride coatings for satellite temperature control.* Thin Solid Films, 2000. 370(1-2): p. 268-277.
5. Munz, W.D., *Titanium aluminum nitride films: A new alternative to TiN coatings.* Journal of Vacuum Science & Technology A: Vacuum, Surfaces, and Films 1986 4(6): p. 2717 - 2725
6. Kopacz, U. and H.A. Jehn, *Morphology and properties of sputtered TiN layers as a function of substrate temperature and sputtering pressure.* Thin Solid Films, 1985. 126(3-4): p. 265-273.
7. Knotek, O.M., W. D. Leyendecker, T. , *Industrial deposition of binary, ternary, and quaternary nitrides of titanium, zirconium, and aluminum* Journal of Vacuum Science & Technology A: Vacuum, Surfaces, and Films 1987 5(4): p. 2173 - 2179
8. Mitsuo, A., et al., *Improvement of high-temperature oxidation resistance of titanium nitride and titanium carbide films by aluminum ion implantation.* Surface and Coatings Technology, 1998. 103-104: p. 98-103.
9. König, W., R. Fritsch, and D. Kammermeier, *New Approaches to Characterizing the Performance of Coated Cutting Tools.* CIRP Annals - Manufacturing Technology, 1992. 41(1): p. 49-54.
10. Mayrhofer, P.H.H., Anders; Karlsson, Lennart; Sjölén, Jacob; , *Self-organized nanostructures in the Ti-Al-N system.* Applied Physics Letters, 2003. 83(10): p. 3.
11. Rachbauer, R., *Comparative microstructural investigations of Ti-Al-N thin films alloyed with Y or Nb*, in *department of physical metallurgy and materials testing*. 2008, Montanuniversität Leoben: Leoben. p. 85.
12. Callister, W.D., *Fundamentals of Materials Science and Engineering: An integrated approach*. 5th ed. Vol. 1. 2000: Wiley.
13. John B. Wachtman, W.R.C., M. John Matthewson, *Mechanical Properties of Ceramics*. 2nd ed. 2009: Wiley.
14. Durand, S., *Phase Transformation in Ti1-xAlxN coatings*, in *Division of Engineering Materials*. 2006, Lulea University of Technology: Lulea. p. 27.
15. Adibi, F.P., I.; Hultman, L.; Wahlstrom, U.; Shimizu, T.; McIntyre, D.; Greene, J. E.; Sundgren, J.-E., *Defect structure and phase transitions in epitaxial metastable cubic Ti0.5Al0.5N alloys grown on MgO(001) by ultra-high-vacuum magnetron sputter deposition.* Journal of Applied Physics 1991. 69(9): p. 6437 - 6450

16. Ohring, M., *Materials Science of Thin Films*. 2nd ed. 2001: Academic Press.
17. Wasa, K.K., Makoto; Adachi, Hideaki, *Thin Film Materials Technology - Sputtering of Compound Materials*. Vol. 1. 2004: William Andrew Publishing.
18. Sauveur, A., *Iron and steel magazine:*
a monthly publication devoted to the iron and steel industry, Volume 8, B.t. laboratories., Editor. 1904: Boston.
19. W.C. Oliver, G.M.P., *Measurement of hardness and elastic modulus by instrumented indentation: Advances in understanding and refinements to methodology.* Journal of Materials Research, 2004. 19(1): p. 3 - 20
20. *Nanoindenters from Micro Star Technologies*, R. 2.3, Editor. 2010, Micro Star Technologies.
21. Bhakhri, V., *A Study of the deformation kinetics of gold using high-temperature nanoindenation technique*, in *School of Graduate and Postdoctoral Studies*. 2009, The university of Western Ontario: London, Ontario.
22. Vineet Bhakhri, R.J.K., *High-temperature Deformation Kinetics of Gold at 473K to 773K.* Material Research Society Symposium, 2009. 1137.
23. H.J. Frost, M.F.A., *Deformation-Mechanism Maps for BCC metals and compound materials*. 1982: Pergamon Press Oxford.
24. Vandeperre, L.J. (2010) *The lattice resistance to dislocation flow*.
25. Willmann, H., et al., *Single-crystal growth of NaCl-structure Al-Cr-N thin films on MgO(0 0 1) by magnetron sputter epitaxy.* Scripta Materialia, 2007. 57(12): p. 1089-1092.
26. Losbichler, P. and C. Mitterer, *Non-reactively sputtered TiN and TiB2 films: influence of activation energy on film growth.* Surface and Coatings Technology, 1997. 97(1-3): p. 567-573.
27. Hultman, L., et al., *Transmission electron microscopy studies of microstructural evolution, defect structure, and phase transitions in polycrystalline and epitaxial Ti1-xAlxN and TiN films grown by reactive magnetron sputter deposition.* Thin Solid Films, 1991. 205(2): p. 153-164.
28. Chen, L., et al., *Compositional and structural evolution of sputtered Ti-Al-N.* Thin Solid Films, 2009. 517(24): p. 6635-6641.
29. Fox-Rabinovich, G.S., et al., *Effect of temperature of annealing below 900 °C on structure, properties and tool life of an AlTiN coating under various cutting conditions.* Surface and Coatings Technology, 2008. 202(13): p. 2985-2992.
30. J. M. Wheeler, R.A.O., T.W. Clyne, *High temperature controlled athmosphere nanoindentation*, in *MRS Fall 2008*. 2008: Boston.
31. Stone, D.S.J., Joseph E.; Puthoff, Jonathan; Elmustafa, Abdelmageed A., *Analysis of indentation creep.* Journal of materials research, 2010. 24(4): p. 611-621.
32. Wiedemann, R., H. Oettel, and M. Jerenz, *Structure of deposited and annealed TiB₂ layers.* Surface and Coatings Technology, 1997. 97(1-3): p. 313-321.
33. Mulford, R.A., *Analysis of strengthening mechanisms in alloys by means of thermal-activation theory.* Acta Metallurgica, 1979. 27(7): p. 1115-1124.
34. Kresse, G. and J. Hafner, *Ab initio molecular dynamics for liquid metals.* Physical Review B, 1993. 47(1): p. 558.

35. Grabowski B., H., T. & Neugebauer, *Ab initio study of the thermodynamic properties of nonmagnetic elementary fcc metals: Exchange-correlation-related error bars and chemical trends.* Physical Review B, 2007. 76.
36. Holec, D., *Private Communication.* 2010.
37. Zabaras, N., *Dislocations*, in *MAE 12*. 2001.
38. Mayrhofer, P.H.M., D.; Schneider, J. M., *Influence of the Al distribution on the structure, elastic properties, and phase stability of supersaturated Ti1-xAlxN.* Journal of Applied Physics, 2006. 100(9): p. 094906 - 094906-5
39. Holec, D., *Multi-scale modelling of III nitrides: from dislocations to the electronic structure*. 2008, Selwyn College: Cambridge.

9 List of figures

10 List of tables

11 List of symbols and abbreviations

Roman letters

A	Contact area between tip and sample [nm^2]
b	Burgers vector [nm]
c	cubic
E	Young's modulus [GPa]
E_{eff}	Effective elastic modulus [GPa]
E_i	Young's modulus of indenter [GPa]
ΔG_{tot}	Total activation energy [eV]
$\Delta G(\tau)$	Thermal activation energy [eV]
H	Hardness [GPa]
h_c	Plastic component of depth
h_{max}	Maximum depth in load-displacement curve [nm]
h_t	Total depth
P_{max}	Load at maximum depth in load-displacement curve [mN]
S	Elastic unloading stiffness [mN/nm]
σ_{ind}	Average indentation stress [MPa]
T_m	Melting Temperature [K]
V^*	Dislocation activation volume [b^3]
ΔW	Mechanical activation work

Greek letters

β	Factor, that accounts for deviation in stiffness [-]
ε	Strain [-]
$\dot{\varepsilon}$	Indentation strain rate [1/s]
$\dot{\gamma}_{ind}$	Indentation shear strain rate [s^{-1}]
τ_{ind}	Indentation shear stress [MPa]
μ	Elastic shear modulus at temperature T [GPa]
μ_0	Elastic shear modulus at 300K [GPa]
ν_i	Poisson ratio of indenter [-]

Abbreviations

Al	Aluminium
AlN	Aluminium nitride
EDX	Energy dispersive X-Ray analysis
GGA	Generalized gradient approximation
LDA	Local density approximation
MgO	Magnesium oxide
NaCl	Sodium chloride
PDF	Population density function
PVD	Physical vapour deposition
SEM	Scanning electron microscopy
TEM	Transmission electron microscopy
Ti	Titanium
TiN	Titanium nitride
TiAlN	Titanium aluminium nitride
VASP	Vienna Ab-initio Simulation Package
XRD	X-Ray diffraction